Let me fall out of the window with confetti in my hair
Deal out Jacks or better on a blanket by the stairs
I'll tell you all my secrets but I lie about my past
Send me off to bed forever more

-Tom Waits

Acknowledgements

I would like to express my appreciation to my supervisors, Prof. David G. Nicholson and Dr. Karina Mathisen, for giving me the opportunity to be part of this research group, and for all support and guidance the past two years. David; I don't think I'll ever forget this comment: "du er visst ikke noe hengehue...". I'll take that as a compliment. Special thanks to Karina whose door is always open. You have inspired me greatly through your dedication to science and your great sense of humor. I'm also really glad I wasn't the only B-person in the group.

Without funding from the Norwegian Research Council and NTNU I would never have experienced the excitement of doing research at the synchrotrons in Grenoble and Lund.

My gratitude also goes to Syverin Lierhagen for carrying out the ICP-MS analyses, and for holding "lectures" on the wonders of Excel. Julian Tolchard for help on SEM and XRD. Sema Akyalcin and Morten Bjørgen for letting me run the FTIR experiment and for giving me pointers on how to interpret the spectra.

A special thanks to Asmira, Beate, Katrine, Mari, Mari, and Tina with whom I've been studying and struggling; I wouldn't have survived here without you. Mari: our coffee breaks and "deep" conversations have so often made my day. Thanks to you I'll never forget what Knutson diffusion is. Bolle kaffi? Beate: I had a blast living in Australia (even though you know how I feel about Newcastle) and traveling around with you. Let me know if you ever need "engine". I'll find you an outlet.

To all the regulars at Mandagspilsen; I've greatly appreciated solving the World's problems and discussing the tilt angle of the floor at Naboen almost every Monday

for the past three years. Next time I'll bring a spirit level. I still mean I won that bet; the staue of Olav Trygvason IS taller than Eirik.

Mom, Dad, Ingrid, Tone and Besta: thanks for always being supportive and giving me a place to vent. Tante Tone: this one is for you. Miss you always.

Kasper, Håkon and Pia Elisabeth: auntie Anlaug will soon be home to teach you how to have fun. All you need is some iodine, ammonia and a coffee filter.

Henning, thank you for always being there for me no matter what and for acting as my personal IT consultant.

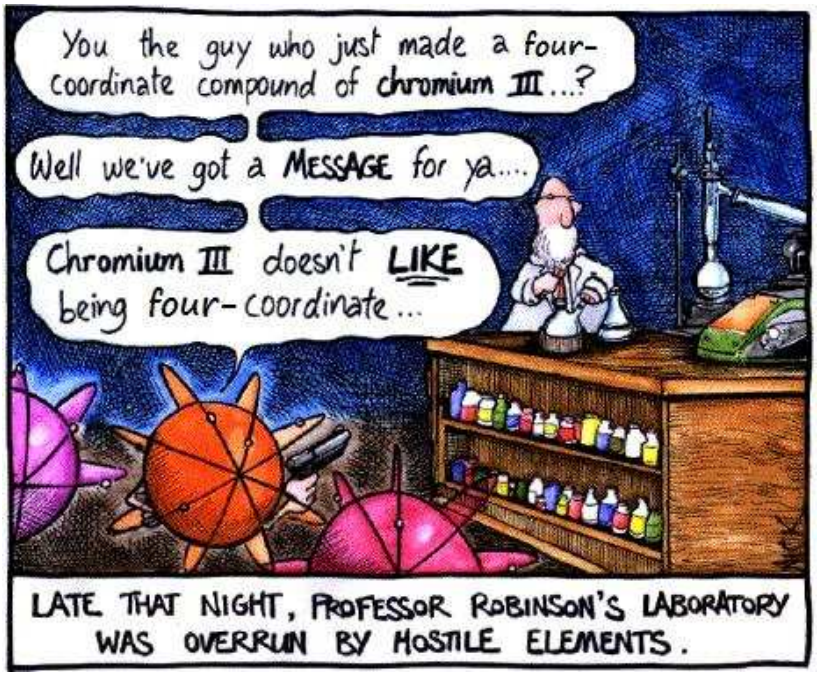

And last, to all the quadrupole transitions I've encountered; thanks for nothing.

May 15, 2009

Anlaug Haukvik Grave

Contents

List of Figures

List of Tables

Chapter 1

Introduction

Metal-substituted aluminophosphate molecular sieves (MeAPOs) has evoked high interest among researchers working in the area of molecular sieve science and shapeselective catalysis. Aluminophosphates have a crystalline three-dimensional network, in which aluminum and phosphorus tetrahedra are linked via oxygen atoms. The porous structure of molecular sieves, combined with their chemical composition, makes them uniquely suitable for use as catalysts or support materials. Isomorphous substitution of transition metal ions in inorganic solids is an important reaction which allows control over cation-exchange capacity and acidity of the molecular sieve materials. Substitution for Al^{3+} has been claimed for a variety of metals[4;5;6] such as Mn(II), Co(II), Fe(II), Mg(II), Zn(II) giving rise to the formation of bridged hydroxyl groups of different acidic strength.

Catalytic properties of chromium, especially in redox reactions, has evoked high interest in chromium containing molecular sieves over the past few years mainly because such materials were expected to reveal favorable catalytic properties due to creation of well-distributed and separated catalytic centers. Substitution of Cr^{3+} for Al^{3+} in AlPO-5s does not induce additional framework charge or ion-exchange ability as the parent framework is neutral. However, if the product exhibits a compositional heterogeneicy with evenly distributed chromium centers, it influences the sorption properties of the material in a similar way as charged centers in other metal substituted AlPO-5s. These sorption centers are able to interact with molecules adsorbed in the pores and act as a catalyst for reactions such as the oxidation of secondary alcohols and hydrocarbons in the liquid phase.[7;8]

One aspect that is generally overlooked in the rush to develop new catalytic system is the stability and heterogenicy of these materials under working conditions. Cr^{3+} in inorganic compounds exhibits a strong tendency to adapt octahedral coordination due to the stability of the trivalent ion and its $3d^3$ ground state which splits into three stabilizing and two destabilizing orbitals in an octahedral field. Substitution for Al^{3+} is consequently a difficult task as it requires tetrahedral coordination of chromium. Octahedrally coordinated chromium may still act as a catalyst, but in that case it would not be a heterogeneous but rather a homogeneous catalyst due to leaching of active chromium into the liquid phase. Homogeneous chromium catalysts are associated with problems due to the toxicity of chromium, and also difficulty in separation, recycling of catalyst after the reaction, etc. It is thus highly important to find a synthesis route in which chromium is incorporated in a stable manner. This is discussed more in detail in Chapter 2.

The issue on whether Cr^{3+} substitutes for Al^{3+} in the framework and to what extent was highly debated until a great discovery was made by Kornatowski et al.[9] revealing a new strategy for chromium substitution in AlPO-5s. By introducing a co-template into the reaction mixture the likelihood of incorporation was greatly increased. The work in this thesis is therefore concerned with the synthesis and characterization of CrAPO-5 with focus on the effect of the co-template.

The aim of this thesis was to investigate the coordination behavior and redox properties of chromium in microporous aluminophosphates of AFI type structure, and the effect of modifying the conventional synthesis method by adding a co-template. This includes syntheses of CrAPO-5 materials and characterization of these by X-ray absorption spectroscopy (XAS) and Raman spectroscopy, in addition to in-house techniques such as X-ray powder diffraction (XRPD) for phase determination, scanning electron microscopy (SEEM) for particle size and morphology, inductively coupled plasma mass spectrometry (ICP-MS) for elemental composition, thermo-gravimetric analysis (TGA), and Fourier transform infrared spectroscopy (FIR) for template investigations. Chapter 2 gives the theoretical aspects of all characterization methods.

The main focus with respect to characterization methods was on X-ray absorption spectroscopy using synchrotron radiation to study the local geometry and redox properties of chromium.

XAS is an element specific local probe, which allows targeted studies of the local

environment (including coordination, bond distances and valence state) of the metal of interest. The pre-edge region holds a great deal of information on the coordination and valence state of chromium. Most of this work has therefore been directed towards interpretation of the features appearing in these regions. In situ XAS studies where the temperature and gaseous environment of the material was altered to simulate real conditions of a working catalyst gave valuable information on what catalytical properties (if any) to expect from the material. Combined in situ XAS/Raman spectroscopy was employed to take advantage of the complementarities of the two techniques in investigating possible solid state transformations under non-ambient conditions and to give a broader view of the material. Monitoring the valence state and coordination of chromium during these different reaction stages provided a better understanding on the behavior of chromium in AlPO-5s.

In situ studies on CrAPO-5 revealed some quite interesting differences between CrAPO-5s with and without the presence of a co-template. Chromium in the material synthesized without a co-template showed a strong redox behavior dependent on the gaseous environment and temperature. The co-templated material also showed redox behavior, however, chromium was not fully oxidized to Cr^{6+}. Through mainly EXAFS and pre-edge peak analyzes, a pseudotetrahedral coordination for chromium in AlPO-5 molecular sieves was suggested for the material synthesized with a co-template. Further investigation as to why chromium behaves in such a manner in co-templated CrAPO-5s is presented in Chapter 4.

Chapter 2

Theory

2.1 Microporous materials[10;11;12;13]

2.1.1 Introduction

Molecular sieve materials are widely used in a large number of industrially important areas such as chemical separation, adsorption and heterogeneous catalysis. The use of heterogeneous catalysts represents a major technology for minimizing waste by simplifying recovery of catalyst and product isolation. Porous solid materials are classified as a function of pore diameter in the following way:

- Microporous materials (d < 20 Å)
- Mesoporous materials (20 < d < 500 Å)
- Macroporous materials (d > 500 Å).

Zeolites are classified as microporous materials due to having pore diameters between 2 and 20 Å. They occur naturally in large deposits and because of their numerous applications, they are also produced synthetically. Their high acidic strength combined with small pore-size distribution and high surface area, has made them valuable in shape-selective catalysis and separation technologies. In recent years there has been extensive research on their ability to act as heterogeneous catalysts for various reactions, and different types of zeolites are now used for industrial purposes.[14] Heterogeneous catalysis play an important role in the petrochemical industry as well as in the production of fine chemicals. Hydroprocessing catalysts

used in various refining processes are bifunctional, where hydrogenation reactions take place at the impregnated metal centers and hydrogenolysis reactions take place at the acid sites.[15] The acid function can be provided by zeolites with the proper geometry. Geometry combined with high surface area is the prerequisite for such an acidic catalyst to function with desired activity and selectivity.

There is several different ways of altering the properties of a zeolite. By changing the Si/Al ratio (e.g. by substituting some Al^{3+} with Si^{4+}), the concentration of cations will also change, and thus influence the hydrophobicity of the zeolite. The position of exchangeable cations are also of great importance. The location, charge or size of the cations can alter the cross section of the rings and channels in the zeolite. This action will have a great effect on the size of the molecules that can be adsorbed in the zeolite, and thus also have an impact on catalytic activity/selectivity. Other structures similar to zeolites containing atoms other than aluminum and silicon have also been synthesized. These are often referred to as *zeotypes*. They have structures similar to those of zeolites, but may contain other elements such as phosphorus.

2.1.2 Aluminophosphates

Microporous aluminophosphate molecular sieves have a crystalline three-dimensional network, in which aluminum and phosphorus tetrahedra are linked via oxygen atoms. Pure aluminum phosphates (AlPO-ns) belong to the family of zeotypes and can be formed by substituting silicon with phosphorus, where *n* refers to a particular geometry. Their general structure can be expressed as

$$[(AlO_2)_x(PO_2)_x]\cdot yH_2O \tag{2.1}$$

Hydrothermal synthesis of aluminophosphates in the presence of of various alkali inorganic cations or organic structure directing molecules (e.g. organic amines or quarternary ammonium salts) has lead to the discovery of a large number of framework structure types. The incorporation of phosphorus into a zeolite was reported in 1971 by Flanigen et al.[16] As opposed to zeolites, AlPOs have neutral frameworks and can thus not act as ion exchangers. They possess a regular pore system with diameters ranging from 3-14 Å, and they can act as sieves on a molecular level. On the basis of their pore diameters, AlPO-ns can be classified as small pore (< 4Å), medium pore (4-6 Å), large pore (6-8 Å) and extra-large pore (> 8Å).

Creating redox and Brønsted and Lewis acid catalytically active sites in AlPOs can be accomplished by replacing Al^{3+} with divalent metals, similar to the procedure of replacing Si^{4+} with Al^{3+} in zeolites. Metal ions can be introduced by impregnation, where a solution of metal salt and water is added to the parent material. This approach has, however, proven to be less useful for metal incorporation as the metal ions mainly seem to be attached to the surface of the framework rather than replacing atoms in the framework. Another more useful method is to introduce the metal salt into the reaction gel prior to hydrothermal crystallization. The metal ion is more likely to be incorporated into the framework via this synthesis route.

AlPOs have recently received a great deal of attention in the field of catalysis. By replacing some of the aluminum with metals like Li, Be, Mg, Mn, Fe or Zn, metal-aluminum phosphates (MeAlPOs) can be formed. Similarly, partially replacing aluminum or phosphorus with silicon in AlPOs or MeAlPOs yields SAPOs and MeSAPOs. However, these metal-substituted aluminum phosphates generally lack the stability of zeolites, and important applications have yet not been commercialized.[17]

The $AlPO_4$-5 was first synthesized in 1978[18], with AFI type structure (the International Zeolite Association [IZA] structure code) and hexagonal symmetry. AlPO-5s are composed of one-dimensional 12-membered-ring (MR) channels with a diameter of about 8 Å, which are surrounded by smaller one-dimensional 4- and 6-MR channels (see Figure 2.1 for illustration). They belong to the large-pore class with a pore diameter of 7.3Å. There is a strict alternation of $AlO_{4/2-}$ and $PO_{4/2+}$ tetrahedra in agreement with the Löwenstein rule which states that *whenever two tetrahedra are linked by one oxygen bridge, the center of only one of them can be occupied by aluminum*.[19] It is thus not possible to have two aluminum tetrahedra side-by-side (sharing the same oxygen) in the framework. This leads to the formation of an electro-neutral structure (see Figure 2.2).

Because they are neutral, it would be reasonable to assume that AlPO-5s would be hydrophobic. However, due to the alternating tetrahedra which create charge discontinuities, such materials reveal considerably hydrophilic properties. For this reason, AlPO-5s are good adsorbents for dipole molecules as for the electrically inert ones.

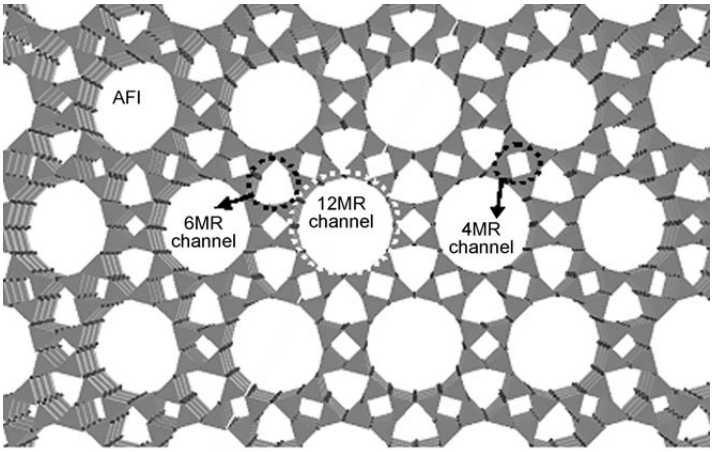

Figure 2.1: AFI structure, viewed perpendicularly to the channel direction, showing the different channels.[1]

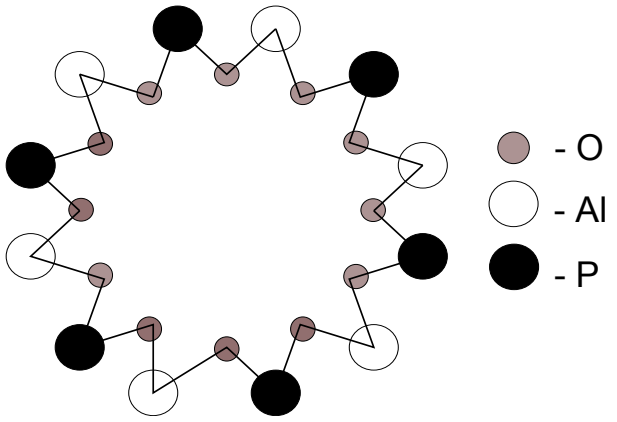

Figure 2.2: Aluminum and phosphorus tetrahedra linked together forming a 12MR channel.

The uses of aluminum phosphates extend from catalysis to possible applications in non-linear optics and nanochemistry. The $AlPO_4$-5 channels are accessible when samples are freshly calcined, and may function as a site-selective catalyst. Catalytic oxidation of hydrocarbons by AlPO-5- materials has been reported.[20;21;22;23]

The main object for studying AlPO-5s in this thesis is their role as catalysts. Due to the presence of many cavities, zeotypes have a very large internal surface suitable for molecule adsorption. They can accommodate many more molecules than an

equivalent amount of amorphous catalyst. In addition, the molecular sieve action makes the zeolite very selective, controlling which molecules to enter (or which molecules to exit) the active sites. This is commonly known as shape-selective catalysis, which is divided into three different groups:

- Reactant shape-selective catalysis
- Product shape-selective catalysis
- Transition-state shape-selective catalysis

Reactant selectivity ensures that only molecules smaller than a particular size can enter the pores and reach the active sites of the zeolite (illustrated in Figure 2.3a). After the catalytic reaction, only products with appropriate dimensions may leave the active sites and diffuse through the channels (see Figure 2.3b). In addition, some reactions are prevented from occurring because the intermediates take up more space than the pores are willing to provide (Figure 2.3c).

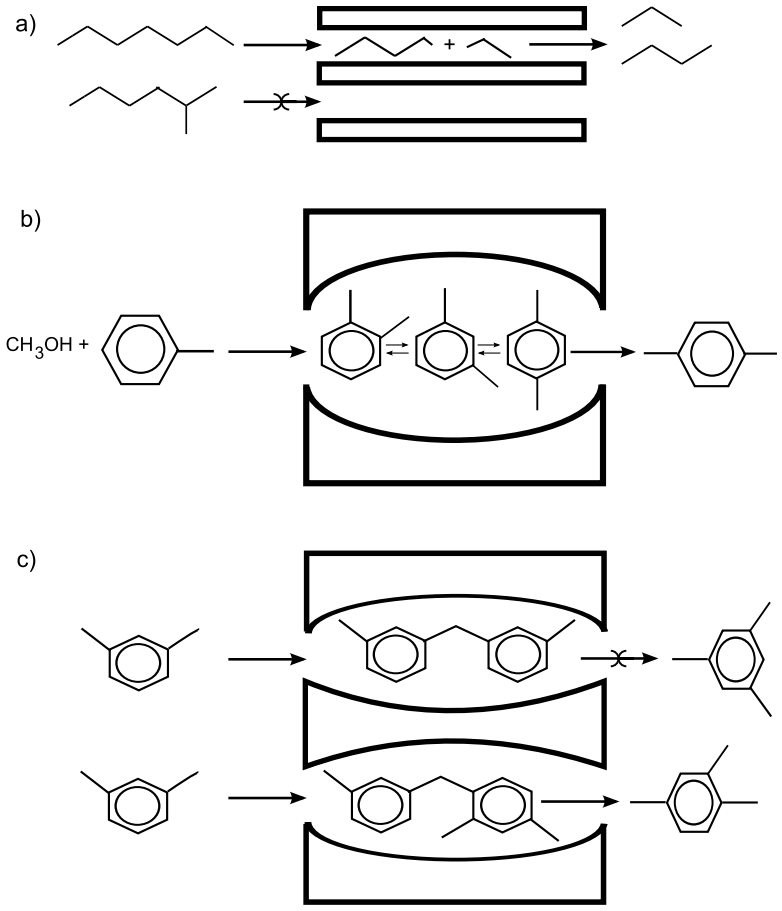

Figure 2.3: Schematic representation of a) reactant selectivity, b) product selectivity, and c) Transition-state selectivity.

2.1.3 The role of structure-directing agents[10;24;25]

The use of structure directing agents (SDA), or templates, is a crucial step in the synthesis of both zeolites and aluminophosphates. A template in this context is a bulky organic amine that fills in the void spaces of a microporous solid. They contribute to the formation of the AlPO-n lattice during crystallization. Templates can enhance stability with London dispersion- and electrostatic interactions, and/or by forming hydrogen bonds. The topology of the template can be faithfully duplicated in only one step. Thus, templates exert both an electronic and a steric influence. Templating gives highly ordered interconnected porous structures with good control over pore size. The way in which the template achieves the microporosity is still

unclear. It involves complex organic-inorganic interactions, but their actual role can vary from structure to structure, and it is therefore difficult to make general assumptions about the role of the template.

Molecular modelling calculations has highlighted the importance of the non-bonded energy between themplate and framework in the determination of the product formed. The non-bonded forces are dominated by van der Waals' interactions between the atoms in the framework and the template atoms. The better the geometric match (the template provides better filling of the void space), the greater the van der Waals' interactions. High void filling within the pore system maximizes the short-range interactions between the SDA and the framework, which leads to a stabilization of the product relative to the structure that would form in the absence of a template. This geometric relationship often extends to a strong match in symmetry between the template and the framework.

Davis and Lobo[26] has classified templates by assigning them three different roles:

- space filling
- structure directing
- "true" templating.

When many different organic molecules can be used to synthesize the same structures, they are considered to be '*space fillers*. Those that direct a specific structure to form are '*structure directing*, while *true templates* direct the framework to adopt the electronic and electronic configurations unique to the template itself. In many cases, by varying the synthesis conditions, the same organic molecule can be used to generate different products. Molecular flexibility is one factor which makes is possible for a template molecule to synthesize more than one product.

The SDA is normally added to the reaction mixture in at least stoichiometric quantities to ensure complete crystallization and maximize void-filling. In reactions where several product phases can crystallize, other effect may be observed with the addition of template in lower amounts. In some cases this can have a major influence on the product formed. Small amounts of a particular template can have a "structure blocking" effect, i.e. it will hinder the formation of certain products. The key factor in determining the product formed in such reactions is not so much the strong geometric match with the potential new product, but rather the mismatch with the default product.

New framework types may be synthesized using the same organic molecule by incorporating different atom types into the network. Substituting different atom types for Al or P (for $AlPO_4$) will alter the bond lengths and angles as well as the stabilities of the frameworks. For example, tetraethylammonium (TEAOH) will form a complex with aluminophosphate molecules that acts as a template for constructing an $AlPO_4$-5 lattice. When zinc is incorporated into some of the aluminophosphate molecules, TEAOH adopts a different conformation and yields a different intermediate complex that acts as a template for the formation of a different structure; ZnAPO-34. It is also important to be aware of that the template may form a complex with the metal and hinder the metal from being incorporated.

Since the $AlPO_4$ framework is neutral, only van der Waals interactions can occur between the guest species and the host framework. NMR has underlined the importance of weak, noncovalent intermolecular forces in precrystalline phases during molecular sieve formation, while Raman spectroscopy has suggested that encapsulation of the template in precrystalline (amorphous) solids occurs and undergoes protonation.

Newer research done by Luis Gómez-Hortigüela et al.[1] has brought new aspects into the light. They claim that the internal space of microporous framework during synthesis is not only occupied by the organic structure directing molecules, and that water can play a primary role in structure direction. The true structure directing species is thus not the organic SDA itself but an aggregate between SDA and water. This situation has been defined as *cooperative structure direction*; water is required to achieve the thermodynamically stable composition of the system.

The template is removed from the molecular sieves by calcination. Calcination in a process in which a substance is subjected to the action of heat, but without fusion, for the purpose of causing changes in physical or chemical composition. A schematic illustration of the templating process in Figure 2.4. The removal mechanism is a two-step process. At low temperature, the loosely bonded template molecules are removed from the near-surface region while at high temperature the template decomposes.

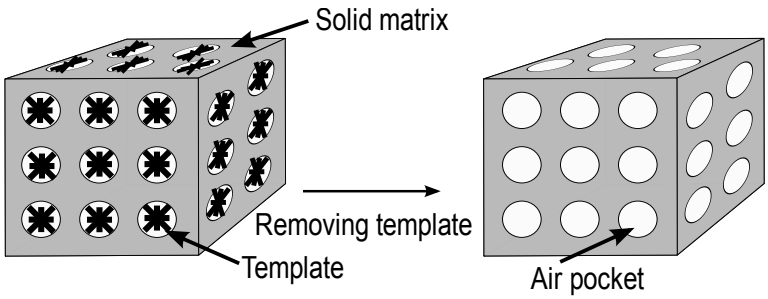

Figure 2.4: A structure with structure directing molecules filling the void spaces (left) and the resulting structure after the SDA has been removed.

The total reaction of the template decomposition is given here for triethylamine (TEA):

$$(C_2H_5)_3N \longrightarrow 3C_2H_4 + NH_3 \tag{2.2}$$

Karl-Heinz Schnabel et al.[27] has proposed a mechanism through which this reaction supposedly occurs:

$$\begin{array}{lcl} & [(C_2H_5)_3NH]^+OH^- & \\ 423K & \downarrow & \longrightarrow H_2O \\ & (C_2H_5)_3N & \\ 523K & \downarrow & \longrightarrow C_2H_4 \\ & (C_2H_5)_2NH & \\ 573K & \downarrow & \longrightarrow C_2H_4 \\ & (C_2H_5)NH_2 & \\ 623K & \downarrow & \longrightarrow C_2H_4 \\ & NH_3 & \end{array}$$

Selective removal of the template (e.g. calcination or dissolution) will give porous material with highly ordered architecture. In absence of structure-directing compounds, no crystalline porous aluminum phosphates will form.

2.1.4 Chromium-substituted aluminophosphates[28;29]

A useful way to alter the properties of aluminum phosphates is to incorporate transition metals into the framework sites of aluminum phosphate molecular sieves by isomorphous substitution for Al^{3+} or P^{5+}. Isomorphous substitution is defined as the replacement of an element with a similar cation radius and coordination requirements.[30] Some of the most important factors to consider for substitution are thus ionic charge, ionic radius, difference in acidic/basic properties in relation to the master framework atoms, and affinity to the formation of tetrahedral coordination with oxygen.[9] The parent frameworks are, however, quite flexible and incorporation of elements with M-O distances that are inconsistent with with the accepted concept for tetrahedral incorporation and cation sizes that differ from that of Al^{3+} has been reported.[30]

A number of divalent metal ions have been reported incorporated into aluminophosphate lattices, including Mn(II)[4], Co(II)[4], Fe(II)[4], Mg(II)[5], Zn(II)[6] giving rise to the formation of bridged hydroxyl groups (Brønsted sites) of different acidic strength. Simultaneously, Lewis sites of low as well as of high acidity are generated. Metal substituted aluminum phosphates are abbreviated MeAPOs.

Chromium compounds are very attractive due to their oxidation ability in many organic reactions. However, due to the toxic nature of chromium, their use in stoichiometric quantities or catalytic (homogeneous) amounts has lead to some serious problems associated with chromium containing effluents. Furthermore, use of homogeneous chromium catalysts also lead to other problems like difficulty in separation, recycling and recovery of the catalyst after reaction as well as deactivation complications, disposal of wastes, etc. A great deal of effort has therefore been put into developing greener processes such as heterogeneous catalysis. Several solid supports (i.e. alumina, silica, and microporous molecular sieves) containing active chromium species have been identified for this purpose.[31]

Substitution of Cr in AlPO-5s was claimed for the first time by Flanigen et. al.[32]. An illustration of the idea of isomorphous substiution of chromium for aluminum is given in Figure 2.5.

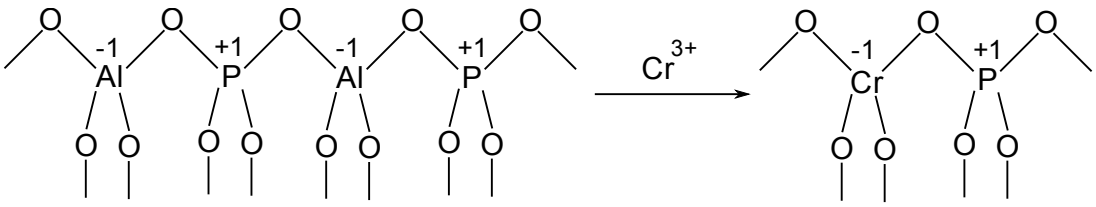

Figure 2.5: Isomorphous substitution of chromium(III) for aluminum(III) leaving a neutral framework.

Weckhuysen and Schoonheydt[28;33] concluded that Cr^{3+} cannot occupy framework positions mainly because of a strong preference for octahedral coordination. This claim is supported by litterature involving stabilization energies which is further discussed below.

Chromium belongs to Group 6 in the periodic table and is is a member of the transition elements. A transition element is defined as an element that has an incomplete d subshell in either the neutral atom or its ions. Chromium may exist in various oxidation states varying from -2 to +6 with +3 being the most stable. This can be explained in terms of electronic configuration and crystal field stabilization energies (CFSE). The electronic configuration of the neutral atom is [Ar]$3d^5 4s^1$. Removing three electrons gives [Ar]$3d^3$. In an octrahedral crystal field, the five d subshells are split into two sets of orbitals; three degenerate lower energy t_{2g} orbitals, and two degenerate higher energy e_g orbitals separated by the ligand-field splitting parameter, Δ_O. The three 3d electrons will accommodate the t_{2g} orbitals which is stabilized by $-2/5\Delta_O$ relative to the energy of the d orbitals in the free atom (see Figure 2.1.4).

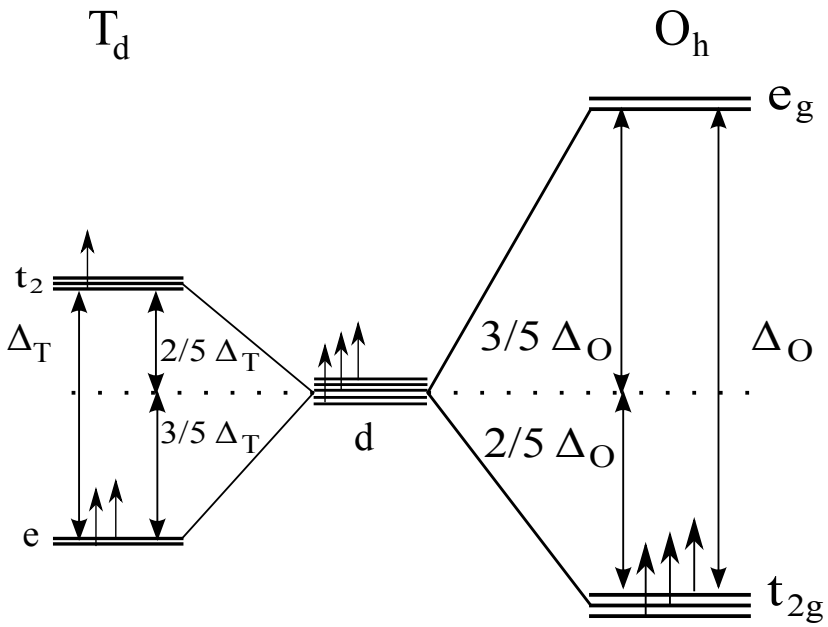

Figure 2.6: The energies of the d orbitals in a tetrahedral (left) and octahedral (right) crystal field.

Electrons in the e_g orbitals would contribute to a destabilization of $+3/5\Delta_O$. In a tetrahedral crystal field, the d orbitals are split in such a way that gives two lower energy e orbitals (stabilization of $-3/5\Delta_T$) and three higher energy (destabilized by +2/5 Δ_T) t_2 orbitals. The splitting parameter for a tetrahedral field is about $4/9\Delta_O$. The CFSE for octahedral coordination of Cr^{3+} is 224.5 kJ/mol and 66.9 kJ/mol[30] for tetrahedral coordination. The most stable coordination for Cr^{3+} is therefore octahedral. The CFSE varies with the number of electrons in the d orbitals and can easily be calculated if the electron configuration is known. Approximate octahedral and tetrahedral CFSEs for various electron configurations are given in Figure 2.8.

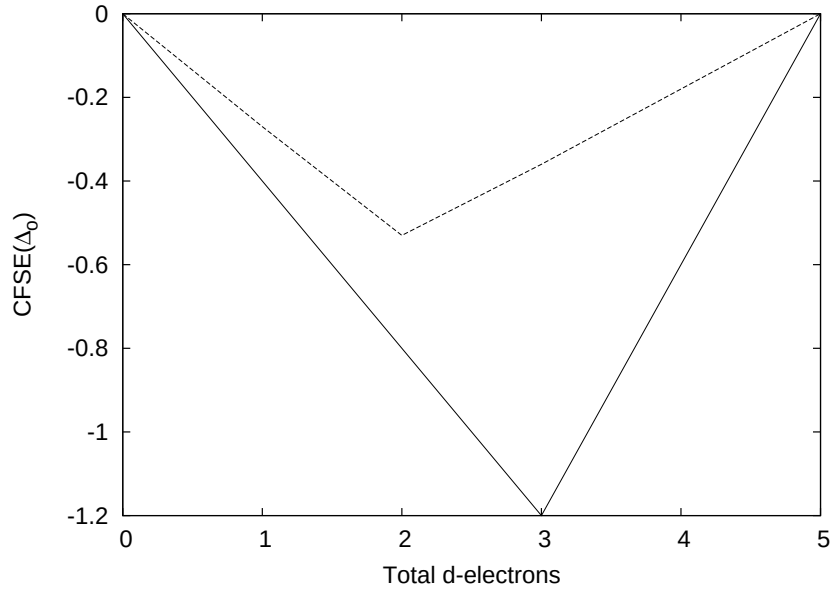

Figure 2.7: Approximate CFSEs for octahedral (solid) and tetrahedral (dashed) crystal fields with varying electron configuration.

One of the criteria for incorporating chromium into the aluminophosphate framework is tetrahedral coordination.[9] The question has been, and still is to some extent, whether Cr^{3+} can be incorporated into the framework because of the large CFSE of octahedral Cr^{3+} complexes. Cr^{6+} on the other hand, may adapt both tetrahedral and octahedral coordination because of its [Ar]$3d^0$ configuration (see Figure 2.8). Another problem arises, however, when Cr^{6+} is tetrahedrally coordinated. The ionic radius decreases to about 0.26 Å which makes it less suitable for substitution with the considerably larger Al^{3+} ion.[34] This decreases the likelihood of Cr^{6+} incorporation drastically. Substitution for P^{5+} is possible, however, it is much more likely that Cr^{6+} will be present as extra framework species, anchored to the surface. An overview of the ionic radii in question is given in Table 2.1.

Coordination	4 (Å)	6 (Å)
Al^{3+}	0.39	0.536
Cr^{3+}	-	0.615
Cr^{6+}	0.26	0.44
P^{5+}	0.17	0.38

Table 2.1: Ionic radii

Synthesis of CrAPO-5[9]

The motivation for incorporating chromium into aluminophosphates materials is mainly due to their catalytic properties. However, as mentioned in the above section, this has proven to be a very difficult task. Many unsuccessful attempts[28;33;35] has been made to incorporate chromium in a stable manner. Newer research has, however, revealed a new strategy for incorporating of chromium into AlPO-5 molecular sieves. Kornatowski et al.[9] suggested a new procedure based on the co-tempating effect. They conclude that chromium substituted AlPO-5s can be synthesized under the following conditions:

- a pseudoboehmite Al compound and
- use of a co-template, e.g. acetate ions or other aliphatic acids

Without an appropriate aluminum source, crystals of low sorption capacities are formed, with extra-framework Cr species clogging the pores. Without the co-template, lower amounts of chromium are incorporated. The Cr^{3+} ions are substituted into the framework mainly in the form of $CrO_{4/2}$ units complemented with two ligands located in the pores to form a distorted octahedral (tetragonal) coordination. These ligands are probably co-template molecules in the as-synthesized samples, while in the form of H_2O in calcined samples. There are several possible co-template options, however, organic acids of chain lengths C_2-C_4 have proven to incorporate the largest amounts of chromium.[36]

Effect of co-template[37;9]

Introducing a co-template into the synthesis gel has been suggested to create a more ideal internal structure and sorption properties than MeAlPOs prepared by

conventional methods. The amount and distribution of substituted metals are also affected. Organic acids as co-template have received a great deal of attention the past few years. The presence of multiple bonds and/or the length of the hydrocarbon chain (C_n), the number and distribution of functional groups and the amount of acid added to the reaction gel are all important parameter that significantly influence the morphology and properties of the crystals. The combined use of co-templates and metals makes it possible to grow crystals with an aspect ratio (i.e. the length of the crystal divided by the diameter, *l:d*) down to approximately 0.05.

The co-templates allow the incorporation of the highest amount of chromium, which, curiously, is not necessarily accompanied by further shifted aspect ratios or perfect morphology of the crystals.

The most regular and flat crystal morphology is observed for the C_1 to C_4 acids. Pentanoic acid causes small, and hexanoic acids causes large, decrease in the crystal morphology and shape, despite their good sorption properties and crystallinity. The favorable tendency to make the length of the crystal shorter is hindered by the affinity to formation of convex external hexagonal walls that look like aggregates. Only the smallest crystals seem to form hexagonal walls.

Kornatowski and Zadrozna[38] has investigated various acids, but the number of experiments and the number of acids have not been satisfactory large with respect to conclude defined tendencies or dependencies between the structure of the co-template molecules and their effect on morphology. They have, however, established that there is a type of mutual interaction between the template and co-templates, and also a synergetic effect of heteroatoms and co-template molecules. The latter (together with the increased amount of incorporated chromium) suggests that the co-templates form complex species with chromium that are more favorable for the framework incorporation than simple hydrated ions. The full role of the co-template is however, yet to be fully understood.

Properties of CrAPO-5[39]

Catalytic properties of chromium, especially in redox reactions, has lead to a high interest in chromium containing molecular sieves. Such materials were expected to reveal favorable catalytic properties due to creation of well separated and well-distributed catalytic centers. Trivalent chromium is an exceptional substituent as

substitution of Cr^{3+} for Al^{3+}in AlPO-5 results in a material with a heterogeneity of composition and no framework charge.

The heterogeneity affects sorption properties in a similar way as charged centers in other metal substituted AlPO-5s. The influence of the neutral centers may be weaker than that of the charged ones, however, the main factors controlling sorption processes are the metal content (i.e. the number of heterocenters), and their distribution inside the AlPO-5). The latter is of greater importance for sorption of nonpolar sorbates. Adsorption potential of low substituted AlPO-5 are lower than that of the parent material, but as the general trend is that when the amount of incorporated metal increases, so does the adsorption potential. This is only true, however, up to a certain limit. Experiments have shown that the highest amount of incorporated chromium does not necessarily mean better sorption properties. In fact, CrAPO-5 with ca. 0.07 mmol/g stably incorporated chromium shows significantly better sorption properties than a CrAPO-5 with 0.32 mmol/g incorporated metal.[9] This may suggest that materials with higher chromium content in fact has some extra framework chromium clogging the pores and thus decreasing the sorption properties.

Chromium substituted aluminophosphates has been reported as active and very selective heterogeneous catalysts for the oxidation of secondary alcohols and hydrocarbons in the liquid phase.[7;8] The incorporated chromium heteroatoms create sorption centers able to interact with molecules adsorbed in the pores. These sorption centers are the active sites in CrAPO-5 materials which slow the diffusion of reactants into the channels. The conversion is therefore somewhat lower than for an AlPO-5. However, the AlPO-5s loose their activity very quickly as a result of coking. The activity of the chromium centers is more stable and maintained for a longer period of time compared with pure AlPO-5 sorption centers.

Stably incorporated Cr^{3+} cannot undergo redox reactions, which is not favorable for redox reactions. The Cr(III) ions do, however, in spite of the lack of additional framework charge, show increased acidity compared with AlPO-5s. This effect can be assigned to the two additional water ligands at Cr, which are located in the pores and complement the coordination of chromium to the favored (pseudo)octahedral coordination.

The conversion of isopropanol is a process for which CrAPO-5 is a very selective catalyst. This particular conversion is possible over acidic cites of any strength and results in a dehydration to propylene. Apart from the main product, small amounts

of diisopropylether (DIPE) can be formed via intermolecular dehydration of isopropanol. Dehydrogenation of isopropanol to acetone may occur over basic centers, however, basicity of the catalyst requires a small amount of a redox component. With no such redox properties, formation of acetone may only occur at temperatures over 573 K.

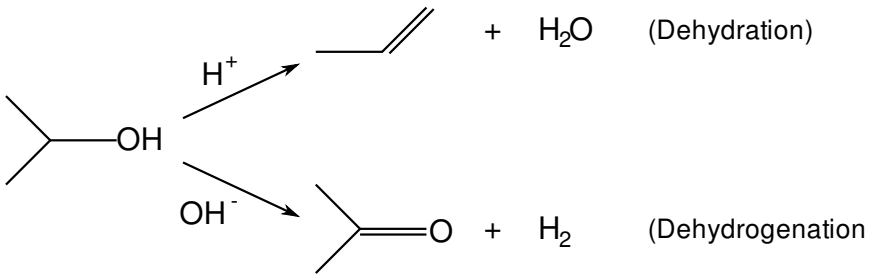

Figure 2.8: Reaction of isopropanol over acidic (top) and basic (bottom) catalytic centers.

Essentially all of the propylene produced for chemical purposes is consumed as a chemical intermediate in other chemical manufacturing processes. It is amongst other things used in the production of synthetic rubber, and as a propellant or component in aerosols.

Another interesting area where CrAPO-5 may possibly be used is in optical applications such as optical amplifiers, phosphors, laser, filters, or optical memories. Some of these applications require, however, large and perfect crystals of the host material. It is therefore important to try and tailor the synthesis of CrAPO-5 to yield products which meet these requirements.[40]

Toxicology[41;31]

The health and environmental effects of chromium depends on which chromium compounds one is exposed to. Chromium in its trivalent form is a necessary trace element of the human body and originates from the diet, drinking water and air. Chromium in its hexavalent form, however, is highly toxic and may cause severe damage to human and animal life. The time weighted average (TWA - an average value of exposure over the course of an 8-hour work shift) concentration for Cr(VI) is 0.05 mg/m^3.[42] Exposure to chromium(VI) above this limit is a serious human

health risk. Significant acute exposure of the skin may cause ulcerations, dermatitis, allergic skin reactions, burns, alterations of genetic materials, cancer, kidney damage or failure, and liver damage or failure. Long-term inhalation can cause lung cancer, and also result in general damage of the respiratory system. If inhaled through the mouth, it can result in serious gum diseases. The primary exposure routes are inhalation of fumes or mist and dermal contact with chromium(VI) used by workers in industrial operations.

Sources of chromium compounds in water, soil, and air can occur be both naturally occurring or anthropogenic. Chromium in air exists as droplets or particles and may be transported by wind and/or deposited onto water or soil. The behavior of chromium in water and soil is quite complex, and there are several factors that determine whether chromium is in its hexavalent or trivalent form, including oxygen levels, pH, temperature, and the presence of organic matter and other chemicals. Hexavalent chromium may leach out of soil into groundwater and migrate over time. Chromium compounds are slowly degradable and can bioaccumulate in organisms.

The toxicity of hexavalent chromium to aquatic organisms varies a great deal, depending on the chemical characteristics and the species of the water. Rainbow trout, lake trout and algae are examples of species that are relatively sensitive to Cr(VI). Cr(VI) is also very toxic to mammals and ingestion can be lethal or result in severe development effects. It is therefore highly important not only to consider worker exposure, but also exposure to animal and plant cultures.

2.2 X-ray Diffraction

X-rays are electromagnetic radiation with wavelengths ranging from about 0.02Åto 100Å. These wavelengths are similar to the size of atoms, and for this reason they are useful to explore the atomic structure in crystals. X-ray diffraction (XRD) is perhaps the most widely used technique for characterizing solid material. It is a chemical analysis method for determination of inorganic structures. The wavelengths of X-rays are comparable to the distances between planes of atoms in a crystal (about 1 Å). Hence, X-rays are diffracted by crystal lattices resulting in a diffraction pattern from which one can identify the crystalline phases present in the material as well as structural properties (grain size, strain state, epitaxy, phase composition, preferred orientation and defect structure). XRD is ideal for in situ studies as it is a

nondestructive technique. Materials of any element may be investigated using XRD, but XRD is more sensitive to high-Z elements since the diffraction intensities from these are much higher than those of low-Z elements. The sensitivity of XRD depends thus on the material in question.[43]

2.2.1 Generation of X-rays[44]

X-ray emission spectra characteristic of the elements in a specimen may be excited by a variety of accelerated particles or incident photons. The most frequently used type of excitation is by photons from X-ray tubes (see Figure 2.2.1).

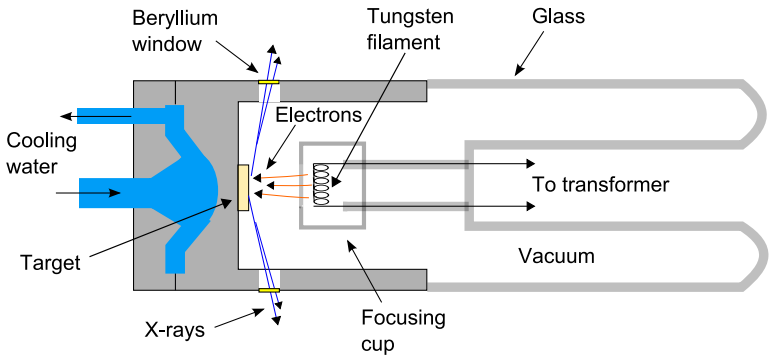

Figure 2.9: Schematic representation of an X-ray tube.

An X-ray tube is an evacuated electron chamber that produces X-rays by accelerating electrons to high velocities by applying a high-voltage field and causing them to collide with a metal target. The tube contains a source of electrons (the cathode) which is usually a tungsten filament, and a thermally rugged anode (metal target) enclosed in an evacuated glass chamber. Electrons are emitted due to current flowing through the tungsten filament causing it to glow. The voltage applied between the cathode and the anode (30 to 100 keV) causes the electrons to move at high velocity from the filament to the metal target. Electrons that are decelerated after colliding with the target emit what is called brehmsstrahlung, while the electrons that have sufficient energy to knock an electron out from the inner shells of the metal target produces characteristic X-rays at discrete energies. Only about 1 percent of the energy produced by the electrons is converted to X-rays.

The X-rays then travel through a beryllium window which acts as a barrier between the vacuum environment inside the tube and the atmospheric conditions on the outside, while at the same time allows X-rays to pass through so that they can be collected and used for different purposes.

Two types of X-ray spectra are produced by bombardment of the metal target of the X-ray tube. The first type is called the *continuous spectra* which consists of a range of wavelengths of X-rays. Minimum wavelength and intensity depend on the voltage across the X-ray tube and the target material. As the voltage increases, the wavelength decreases while the intensity increases (see Figure 2.10).

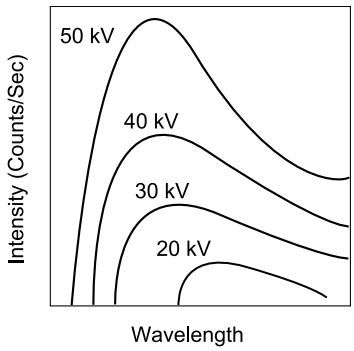

Figure 2.10: Intensity versus wavelength for various voltages.

The other type of spectra, namely the characteristic spectra, is produced at high voltage as a result of the specific electronic transitions that occur within the individual atoms of the target. If the energy of the accelerated electrons have sufficient energy to knock out K-shell electrons (the innermost electrons), electrons from the L- and M-shells relax to fill the place of the dislodged electrons. These electronic transitions produce X-rays characteristic for the atom considered. A transition from the L-shell to the K-shell produces K_α X-rays, while a transition from the M-shell to the K-shell produces K_β X-rays. The intensity of these X-rays are much higher than those produced by the continuous spectra. The K_α rays can be filtered out to obstain higher intensity X-rays.[44]

Wavelengths of the X-rays produced by some common metal targets are given in table 2.2.

Table 2.2: Experimentally determined wavelengths for X-rays produced by commonly used target materials

Element	K_α Wavelength (λ)
Mo	0.7107
Cu	1.5418
Co	1.7902
Fe	1.9373
Cr	2.2909

2.2.2 X-ray diffraction and Bragg's Law

A beam of X-rays consists of several separate waves which can interact with one another. Waves can interfere either constructively (waves are in phase) or destructively (waves are out of phase). If waves interfere constructively, their amplitudes will add together to produce a wave of higher amplitude. Destructive interference will reduce the amplitude or, in extreme cases, even destroy the resultant wave. Atoms in a crystal interact with X-rays in a similar way to produce interferences. The waves are reflected by planes of atoms i.e. crystal lattice planes. If the incident X-rays have the same starting point, their relative phases depend on the path lengths. As can be seen from Figure 2.11, the path-length difference between rays 1 and 2 is BC + CD. Both the X-rays reflects off of the lattice planes at an angle θ, equal to the angle of incidence. Thus, including the distance, d, between planes, the path-length difference can be expressed as $2d\sin\theta$. If this distance is not an integral number of wavelengths, destructive interference will occur. Thus, the following must be true in order for constructive interference to occur:

$$2d\sin\theta = n\lambda \tag{2.3}$$

Equation 2.3 is known as Bragg's Law for X-ray diffraction.

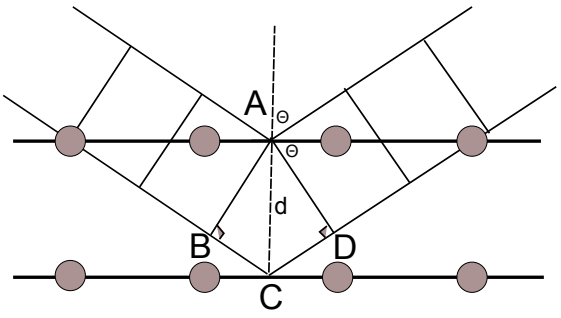

Figure 2.11: Visualization of the derivation of Bragg's law.

2.2.3 X-ray powder diffraction

In powder X-ray diffraction (XRPD), the sample is in a fine powdery form, consisting of grains of single crystallites randomly oriented throughout the sample. By scanning through at incident angles from 0 to 90°, angles where diffraction has occurred will be recorded and associated with different atomic spacings. An X-ray powder diffractometer is used to record these data. The powder is packed in a sample holder and placed on a sample stage so that it can be irradiated. An electronic detector detects the rate of the diffracted X-rays (counts/second) and delivers this information to a computer. A goniometer is used to rotate the sample and to maintain the angle. See Figure 2.12 for a simplified setup.

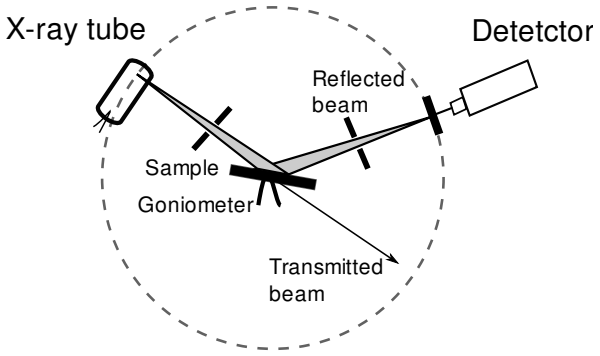

Figure 2.12: The basic components of a XRPD experiment.

When a scan is completed, the X-ray intensity can be plotted as a function of 2θ to produce an XRD pattern.

From the angle 2θ for each peak in the diffraction pattern, the d-spacing may be

calculated using the Bragg equation (equation 2.3). The specimen in the sample may be identified by running the results through the powder diffraction files (PDF) database, a data collection of thousands of crystalline substances. XRD patterns may be used as "fingerprints" for determining samples of unknown composition.[43]

The advantages of XRPD are:

- sample preparation is easy
- not very time consuming
- can analyze mixed phases

Although one can resolve structural structures from PXRD data alone, the single crystal technique is far more accurate.

2.3 X-ray absorption spectroscopy[45;46;47]

2.3.1 Introduction

X-ray absorption spectroscopy (XAS) has for some years now been applied to various scientific and technological systems in diverse fields such as inorganic chemistry, catalysis, biochemistry, etc. It has proven to be very useful for systems where single-crystal techniques fail to provide accurate structural information (e.g. liquids, gases, amorphous and polycrystalline solids, etc.). An XAS spectrum is obtained by plotting the absorption of X-rays, normally expressed by the absorption coefficient μ, as a function of the photon energy. The resulting XAS spectrum can, by convenience, be divided into three regions; the pre-edge region, X-ray Absorption Near Edge Spectroscopy (XANES) and Extended X-ray Absorption Fine Structure (EXAFS). The edge is the reference point at which a core electron is ejected from its core level. The pre-edge region is found near or below the edge, the XANES region extends from a few eV below to approximately 40 eV above the edge, while the EXAFS region generally refers to the energy interval 40-1000 eV above the the absorption edge in the XAS spectrum of the central atom (Figure 2.13). The XANES region contains information about the coordination and valence state, while interatomic distances and coordination numbers may be extracted from the EXAFS. Pre-edge regions generally contain absorption peaks due to excitation of core electrons to some bound states.

Valuable bonding information such as electronic configuration, site symmetry and energetics of virtual orbitals can be extracted from these peaks.

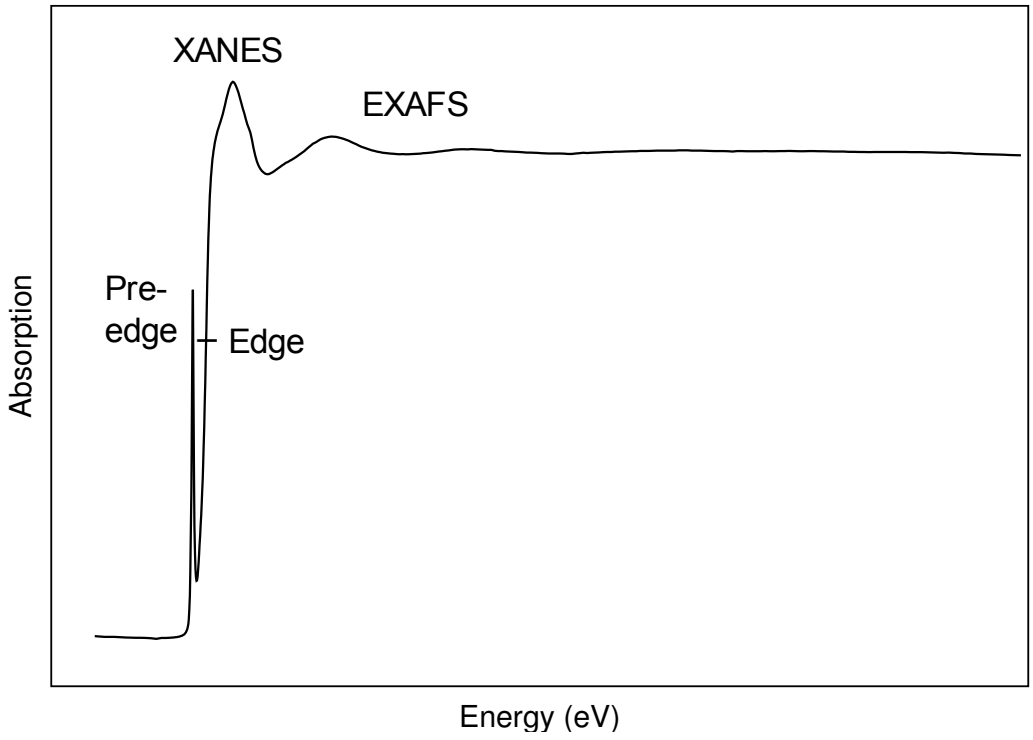

Figure 2.13: X-ray absorption spectrum labeled with the different regions

When a monochromatic beam travels through matter, it looses intensity due to interactions with the material. The loss in intensity is proportional to the initial intensity of the beam and the sample thickness x:

$$dI = -\mu I dx \tag{2.4}$$

The absorption coefficient can be calculated using Eq. 2.5 which is obtained by integrating Eq. 2.4.

$$\mu x = \ln I_0/I \tag{2.5}$$

where x is the thickness of the absorbing material, and I_0 and I are the intensities of the incident and transmitted beams, respectively (See Figure 2.14).

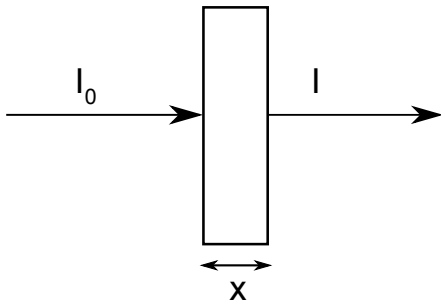

Figure 2.14: An X-ray of intensity I_0 travels through a material of thickness x and looses intensity.

The absorption coefficient is the sum of two components which reflect two different modes of interaction between X-rays and the matter it travels through; the true absorption coefficient τ and the scattering coefficient σ:

$$\mu = \tau + \sigma \tag{2.6}$$

The true absorption coefficient relates to the photoelectric effect where the excess energy from the incoming photoelectron is carried away by the ejected electron as kinetic energy. The scattering coefficient σ relates to the fact that the X-ray photons may experience a change in direction. This change in direction may or may not be accompanied by energy loss of the X-ray photons.

Sometimes it can be convenient to record XAS data in fluorescent mode, especially when working with dilute materials from which signals may be weak. For very dilute materials, problems occur when the small edge of interest is located on a high background absorption. In fluorescence mode the background absorption is removed, hence improving the sensitivity. The fluorescent radiation is measured at right angle to the incident beam. For a fluorescence experiment, the absorption coefficient is defined by:

$$\mu_f x = I_f / I_0 \tag{2.7}$$

where I_f is the intensity of the fluorescent beam.

When the X-ray energy reaches the value of the binding energy of some core electron of an atom in a sample, the electron will be ejected from an inner shell to the

continuum and a sudden increase in the absorption coefficient occurs. This abrupt increase defines the K absorption edge, which represents the amount of energy needed to eject a K-shell (1s) electron. Depending on the X-ray energy, electrons from the 2s, $2p_{3/2}$ and $2p_{1/2}$ orbitals (L-shell) may also be ejected and give rise to L_I, L_{II} and L_{III} absorption edges respectively. The edge position (given in eV) is element specific and represents how strongly the electrons are bound to the core of the atom. Hence, the position of the edge is also dependent on the valence state of the central atom. The edge is shifted (normally of the order of some eV) to higher energies with increasing valence state and is thus related to higher electron binding energies. For chemically similar compounds, the edge positions may be compared to indicate different oxidation states of the central atoms. By comparing the edge energies with that of a reference material in a similar chemical environment, the valence states of these atoms may be determined.

In order to excite an atom, it must absorb a photon. In X-ray *photoionization*, a photoelectron is ejected from a core level after absorbing a photon. The excited atom is the allowed to relax through a number of mechanisms, e.g. the *Auger* process or the *fluorescent* process (see Figure 2.15). The probability for Auger transitions to occur is relatively high, especially for light elements and/or at low energies. When a core electron is removed, the electrons in the higher shells will rearrange. The core level vacancy is filled, and the excess energy is released by ejecting another electron from the same higher shell. The fluorescent process is somewhat similar, only that the excess energy is released by emitting fluorescent photons.

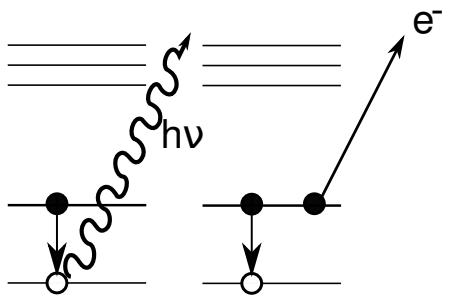

Figure 2.15: Fluorescence (left) and Auger (right)

2.3.2 The Pre-edge region[29;48]

Near the edge region, the photon energy is too low to excite core electrons. However, transitions of core electrons to empty bound states may occur and can be observed as peaks just below the edge. These pre-edge peaks are caused by a so-called dipole-forbidden 1s→3d transition and are sensitive to the electronic configuration and the symmetry around the central atom. In order to understand why these transitions still can occur, it is necessary to investigate the spectroscopic selection rules and which factors that may contribute to the relaxation of these rules.

A spectroscopic selection rule states which transitions that are allowed and which that are forbidden. An allowed transition has a nonzero transition dipole moment (the electric dipole moment associated with transitions between initial and final states), and hence nonzero intensity. For a forbidden transition the calculated transition dipole moment is zero. The *Laporte selection rule* is of great importance in the transitions occurring in the pre-edge area. It states that in a centrosymmetric molecule or ion, the only allowed transitions are those accompanied by a change in parity. This rule requires a little bit of knowledge about the symmetry of the orbitals of the central atom. The symmetry classes of the s, p, and d orbitals of a molecule of T_d and O_h (tetrahedral and octahedral symmetry respectively) point groups are given in Table 2.3. Transitions between g and u terms are allowed, while a transition from a g term to another g term is forbidden (the same is valid for u to u transitions).

The Laporte selection rule may be relaxed in two ways. A transition that is formally dipole forbidden can gain intensity through either a quadrupole transition mechanism or through metal $4p$ mixing with $3d$ orbitals giving the transition an electric dipole allowed character. A quadrupole transition can occur when the energy levels of a nucleus with spin quantum number I>1/2 split as a result of interaction between the Electron Field Gradient (EFG) at the nucleus and the electric quadrupole moment of the nucleus itself.[49] Such transitions are about 2 orders of magnitude weaker than dipole transitions and contributes thus only a little to intensity of the pre-edge feature even though $g \leftrightarrow g$ transitions are quadrupole allowed. For these reasons, it is therefore incorrect to describe pre-edge peaks in terms of 1s→3d transitions as such dipole transitions never occur even if the central atom has tetrahedral symmetry.

	T_d	O_h
s	A_1	A_{1g}
p_x	T_2	T_{1u}
p_y	T_2	T_{1u}
p_z	T_2	T_{1u}
d_{z^2}	E	E_g
$_{x^2-y^2}$	E	E_g
d_{xy}	T_2	T_{2g}
d_{yz}	T_2	T_{2g}
s_{zx}	T_2	T_{2g}

Table 2.3: Symmetry species of orbitals on the central atom.

Take Cr(VI) as an example. In octahedral symmetry, the final states (empty d orbitals) are T_{2g} and E_g, hence the transitions are:

$A_{1g} \rightarrow T_2g$

$A_{1g} \rightarrow E_g$,

which are Laporte forbidden. This results in a very weak (quadrupole allowed) transition with a corresponding small intensity of the pre-edge peak. In tetrahedral symmetry (where no inversion symmetry is present) the final states are T_2 and E which gives the expected transitions

$A_1 \rightarrow T_2$

$A_1 \rightarrow E$.

As can be seen in Table 2.3 the d and p orbitals have same symmetry, so the metal $3d$ and $4p$ orbitals may mix and hence allow direct dipole transitions into the $4p$ character of the $3d$ band. The $A_1 \rightarrow T_2$ therefore becomes particularly strong. This transition will also overwhelm the much weaker $A_1 \rightarrow E$ transition.

Pre-edge features are for these reasons strong in intensity for tetrahedral coordination, whereas extremely weak or zero for regular octahedral coordination. For central atoms with the same

The number of d-electrons also affect the intensity of the peaks. For a given element, the pre-edge peak intensity increases with increasing oxidation number. The general

trend, regardless of the type of element, is that the intensity will increase with decreasing number of d-electrons. Thus, the pre-edges of Fe^{6+} and Cr^{4+} (both with d^2 configuration) will have similar intensities. The reason for this effect is that when the number of d-electrons decreases, the empty p component in p-d hybridized orbitals will increase, which in turn results in a higher pre-edge peak. The d^0 elements give the highest peak, and the intensity decreases monotonically with the number of d electrons and reaches zero for d^{10}.

2.3.3 Basic EXAFS theory

The probability that an X-ray photon will be absorbed by a core electron depends on the initial and final states of the electron. The initial state is the core level corresponding to the absorption edge. The final state can be thought of as an outgoing spherical wave starting from the absorbing atom. For isolated atoms (e.g. monoatomic gases such as Krypton), the photoelectron may travel freely as a spherical wave. As a result, the absorption coefficient will decrease monotonically as a function of energy beyond the absorption edge. Atoms in molecules, however, behave differently due to the presence of neighboring atoms. The outgoing photoelectron can be backscattered from the neighboring atoms, thus producing a wave traveling in the opposite direction interfering either constructively or destructively with the outgoing wave (Figure 2.16). The interference between the outgoing and incoming waves gives rise to the sinusoidal variation of μ as a function of E known as EXAFS.

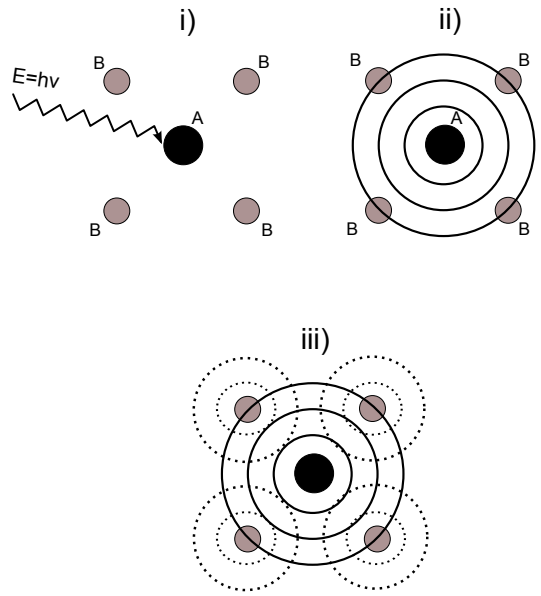

Figure 2.16: i) Incoming photon interferes with the central atom A, ii) producing outgoing waves from A. iii) The outgoing waves are backscattered from neighboring atoms B.

A number of individual waves are produced due to differences in types of neighbors and/or bond lengths. The sum of these waves can give information about atoms in the local three-dimensional environment surrounding a central atom. Constructive interference between the outgoing and backscattered waves will increase the absorption coefficient while a destructive interference will decrease the absorption coefficient, creating crests and troughs in the spectrum.

The theoretical description of EXAFS considers only the oscillations in the absorption spectrum produced by the backscattering process. This oscillatory fraction of the spectrum, χ(E), is defined by:

$$\chi(E) = [\mu(E) - \mu_0(E)]/\mu_0(E) \tag{2.8}$$

where μ(E) is the absorption measured at a given X-ray wavelength and μ_0(E) is the

background absorption, i.e. a "smooth" absorption that would occur for an isolated atom. In order to understand the appearance of the fine structure oscillations it is necessary to have a look at the wave properties of the photoelectron and thus introduce the photo electron wave vector k:

$$k = \sqrt{\frac{2m}{\hbar^2}(E - E_0)} \tag{2.9}$$

where m is the rest mass of the electron, $\hbar$ is the reduced Planck's constant and $(E-E_0$ is equal to the kinetic energy of the ejected electron. Equation 2.9 provides a way of converting χ(E) from the energy scale (eV) to the photoelectron wave vector or k scale (Å^{-1}) given that the value of E_0 is known. χ(k) is the sum of all sine waves with different frequencies as a result of backscattering from all coordination shells and can be described in terms of structural parameters by the EXAFS equation:

$$k^n\chi(k) = k^{n-1}\sum_j \frac{N_j}{r_j^2} \times S_i(k) \times F_j(k) \times e^{-2\sigma_j^2 k^2} \times e^{-2r_j/\lambda_j(k)} \times sin[2kr_j + \phi_{ij}(k)] \tag{2.10}$$

where F_j is the backscattering amplitude from each of the neighboring atoms (N_j) of the jth type with a Debye-Waller factor of σ_j (which accounts for static disorder and thermal vibration). $\phi_{ij}(k)$ is the phase shift that occurs due to the potentials of the central atoms i and the backscattering atoms j. The inelastic losses in the scattering process is accounted for by the term e^{-2r_j/λ_j}, where λ is the electron mean free path and r_j is the distance from the absorber to the the atoms in the jth coordination shell. $S_j(k)$ is the amplitude reduction factor due to many body effects at the central atom i.

Each EXAFS wave is determined by the backscattering amplitude ($N_jF_j(k)$), modified by $S_j(k)$, $e^{-2\sigma_j^2k^2}$, and $e^{-2r_j/\lambda_j(k)}$, and the distance dependence ($1/kr_j^2$), and the sinusoidal oscillation which is a function of $2kr_j$ and $\phi_{ij}(k)$. In order to determine N and σ, $F(k)$ must be known reasonably well, and, in order to determine r, the phase ($\phi(k)$) must be known accurately. These functions can either be determined empirically from model compounds or calculated theoretically.

Equation 2.10 can be reduced to a more general form by combining the numerous terms:

$$k^n = k^{n-1} \sum_j A_j(k) \times sin[\Psi_{ij}(k)] \tag{2.11}$$

where $A_j(k)$ represents the total backscattering amplitude of the jth coordination shell and $\Psi_{ij}(k)$ is the corresponding total phase.

The full EXAFS equation given in Eq. 2.10 is based on a *plane wave single scattering approximation* developed in the 1970s by Sayers, Stern, and Lytle.[50] The plane wave theory or the *small atom approximation* assumes that the atomic radii are much smaller than the interatomic distances, meaning that the backscattered incoming spherical waves can be approximated through the plane wave approach. When ignoring the curvature of the electron wave, the EXAFS expression is largely simplified.

Phase

The sine function in Eq. 2.10 and 2.11 accounts for the oscillations seen in the EXAFS. The argument inside the function, Ψ_{ij}, is the total phase of the backscattered photoelectron wave at the central atom consisting of two parts. The first part is related to the time it takes for the electron to travel from the absorbing atom to the backscatterer and return. This time would be represented by $2kr_j$ if the kinetic energy of the electron was constant across the entire r-range. However, the velocity of the electron will increase as it approaches an atom because the potential that the electron experiences decreases to more negative values as the electron is attracted more by the nucleus (see Figure 2.17). This effect is accounted for in the phase shift function which is defined as:

$$\phi_{ij} = 2\phi_i + \phi_j \tag{2.12}$$

where $2\phi_i$ and ϕ_j are the phase shifts for the absorber and the scatterer respectively. The phase shift by the absorber is accounted for twice because the photoelectron wave phase is shifted once going out and once coming back.

This part only accounts for 10% of the total phase, but it is still important to determine ϕ_{ij} before the nearest neighbor distance can be calculated with an accuracy better than $\pm$0.1 Å. If the phase shift is ignored, the radii (or bond lengths) will appear shorter than they really are. The value of ϕ_{ij} varies systematically with increasing atomic

number (Z), and can be determined experimentally, from standard compounds with absorber/scattering pairs similar to the material in question, or theoretically calculated. This value is then subtracted from the total phase of the unknown material to obtain accurate neighbor distances.[51]

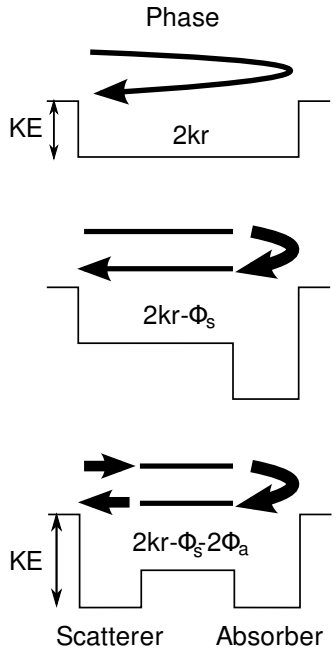

Figure 2.17: Graphic representation of the phase shift.

Amplitude

The total amplitude ($A_j(k)$) is a function of the backscattering amplitude from all neighbors in the jth shell ($N_j F_j(k)$), reduced by the Debye-Waller factor, inelastic losses in the scattering process, and the the amplitude reduction factor. The EXAFS amplitude is also dampened by the factor $1/r^2$, which reflects the decrease in photoelectron amplitude per unit area as one moves further away from the absorbing atom. This means that the EXAFS signals are significantly reduced the longer the photoelectron travels. EXAFS oscillations are typically only observed within approximately 5Åfrom the absorber.

The backscattering amplitude function ($F_j(k)$) is a function of the backscatterer type, not the absorber type. The photoelectron coming from the absorber is scattered by core electrons in neighboring atoms and the binding energies of these core levels affect

the intensity of the backscattering. This intensity is enhanced at those photoelectron energy values equal to the orbital energies of the respective atoms. The core level energies can be converted into k-space according to Eq. 2.9, thus the k-dependence of $F_j(k)$. For hydrogen, this means that only one maximum is observed in the backscattering amplitude (due to the presence of only 1s orbital) at low k, after which the scattering decays quickly. Two peaks can be seen for oxygen; one due to scattering off the 2p orbitals, and the second off the 2s orbitals.[52]

The remaining terms in $A_j(k)$ account for the physical effects that reduces the backscattering amplitude. Two of these factors are related to inelastic scattering processes which the photoelectron experiences as it travels back and forth between the absorber and the scatterer. The reduction factor, $S_j(k)$, depends only on the absorber and accounts for inelastic losses caused by multiple excitations from processes such as shake-up (excitation to higher bound orbitals) and shake-off (excitation to continuum). Thus, not all of the X-ray photon energy is transferred to the propagating photoelectrons, resulting in a kinetic energy lower than $(E - E_0)$ in Eq. 2.9. The second inelastic scattering effect, due to excitation of the neighboring environment, is approximated by $e^{2r_j/\lambda_j(k)}$, where $\lambda_j(k)$ is the mean free path of the photoelectron. The mean free path will increase with increasing k, which means that the significance of this effect will be greater at low k. Inelastic scattering processes are dominated by loosely bound electrons which are sensitive to the chemical environment.

The vibrational motion and static disorder of the backscattering atoms, represented by $e^{-2\sigma_j^2 k^2}$, also contributes to the damping of the EXAFS amplitude, especially at high k. System temperature also plays an important role here. At high temperatures the vibrational motion of the atoms increases, and thus reducing the amplitude. By studying the temperature dependence of the EXAFS amplitude, the Debye-Waller factor (σ_j^2) can be separated into two components:

$$\sigma^2 = \sigma_{vib}^2 + \sigma_{stat}^2 \tag{2.13}$$

where σ_{vib}^2 and σ_{stat}^2 represents the thermal (vibrational) and static disorder respectively. This approximation assumes harmonic vibration and Gaussian static disorder and is only applicable to systems of low disorder.

2.3.4 Experimental set-up[45;46;53;54;55]

The X-ray source used for EXAFS measurements is synchrotron radiation. This type of radiation occurs when charged particles (e.g. electrons or positrons) move in a curved path or orbit in a magnetic field at velocities close to that of light where relativistic effects dominate. Such radiation is very intense, and sharply collimated toward the tangential direction of the circle, highly polarized in the plane of the circular motion, and with a broad spectral range from far infrared down to hard x-rays. The flux (number of photons emitted per second with a unit energy range) of synchrotron radiation exceeds that of conventional X-ray sources by 3 to 6 orders of magnitude.[56] The high flux greatly improves the signal-to-noise-ratio significantly, thereby reducing the acquisition time from several days (for conventional sources) to 30 minutes. This is especially important for systems with low concentrations of the target elements.

The spectral distribution varies with the running conditions and size of the synchrotron and the types of magnets used (bending magnets, undulators or wigglers). Bending magnets are generally used for XAS experiments as they give a high and uniform flux of photons over a wide energy range (which is extremely important for XAS measurements as a typical spectrum extends over 1000 eV). Wigglers provide higher intensity X-rays, however the energy range is much more narrow.

The electrons in a synchrotron radiation facility is produced and accelerated by electric fields in a pre-injector before entering a synchrotron booster where the energy of the electrons is increased. When the electrons enter the storage ring they are forced to move along a circular path by bending magnets. This causes the electrons to emit synchrotron radiation. After the beam is generated it passes through some slits and enters a monohcromator. The monochromator, usually consisting of a silicon single crystal, can filter out a single desired wavelength of radiation with a narrow bandwidth according to Bragg's Law (Eq. 2.3). Mirrors help to focus the monochromatic beam and rejects higher harmonics. The monochromatic X-rays are then sent to the experimental hutch and used in transmission and fluorescence experiments. See Figure 2.18 for a simplified XAS experiment set-up.

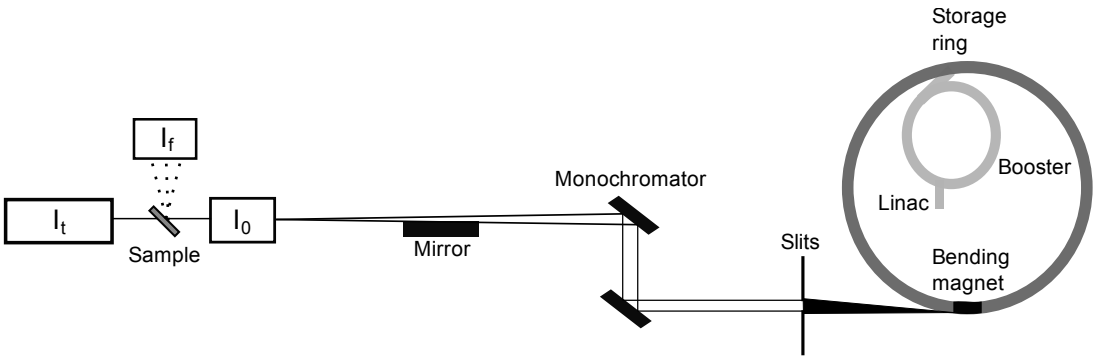

Figure 2.18: Simplified experimental setup for an XAS experiment.

Regardless of detection scheme (transmission or fluorescence), the incident intensity must be measured in order to remove the effect of a varying source intensity. This must be done so that only a small fraction of the incident intensity is depleted. Ion chambers have been most widely used in the X-ray regime. They are filled with a gas or a mixture of gases contained by two thin windows and work on the principle of measuring photoion current. Ion chambers are also used as detectors for transmitted beams. A major advantage of ion chambers is that the gas mixture can be adjusted to fit various experiments. Generally, for fluorescence experiments, a scintillation detector, a nondispersive solid-state detector, or a combination of a curved crystal analyzer and a scintillation detector is used.

2.3.5 In-situ measurements

Catalytical systems often include a carrier system (e.g. zeotypic material or dense materials like alumina) and an active metal finely distributed throughout the system. A great challenge lies in determine the roles of the carrier system and the active metal in catalysis.

In situ XAS studies can enhance the understanding of such systems given that the metal in question is suited for such investigations. The temperature and gaseous environment of the material can be altered to simulate real conditions of a working catalyst using an in situ cell (further described in Section 4.8). Useful information such as metal redox properties and exhaust gas composition can be extracted from an XAS in situ experiment by performing scans at various temperatures and gas mixtures.

Such studies on CrAPO-5 give clear information on whether Cr is incorporated into the AlPO-5 framework as chromium should reveal no redox properties under any conditions if stably incorporated.

2.3.6 Data reduction[46;2]

Before any structural parameters can be determined, the EXAFS oscillations need to be extracted from the measured absorption spectrum. There are several utilities for processing EXAFS data available[57]; the ones chosen for this study are ATHENA[58;2], which is a part of the XAS analysis software package IFEFFIT, fityk (a peak fit software), and EXCURV98[59] developed by the Daresbury laboratory. Athena was used for data normalization and background substraction, and although ATHENA has a peak-fitting function, fityk was used as it is designed for this purpose. EXCURV98 was used to extract information from EXAFS.

There are several processing steps that needs to be gone through before the data can be reduced to $\chi(k)$. The procedure can be divided roughly into three parts:

- Importing raw data and converting it to $\mu(E)$
- Normalizing the data so that the measurements are independent of sample variations or detector setup
- Determining the background function and subtract it from the data to convert it to $\chi(k)$

Normalizing and background subtraction

ATHENA uses the AUTOBK algorithm to normalize and determine the background of $\mu(E)$ data. A detailed description of this algorithm is described by M. Newville et. al.[60].

Once the data is imported and converted, the process of normalizing the scans can begin. This is an important part of the data processing as it allows direct comparison between scans regardless of sample and detector setup variations. It also affects the presicion of the absolute value of the EXAFS amplitude and hence the coordination number. Multiple scans of the same material (recorded under same conditions) should first be merged to increase the signal-to noise-ratio. Also, monochromator

glitches can (and should) be removed to ease the background subtraction process. Truncating data may be useful if data becomes noisy after a particular energy or if the data range exceeds a second absorption edge. This option allows one to remove all data points after a chosen energy.

The normalization is controlled by the threshold energy (E_0), ”pre-edge range“, and ”normalization range“ parameters. The value of E_0 is chosen from a metal foil scan of the metal of interest. There is no recipe for how to identify E_0 as there is no obvious feature in the edge region that can be assigned to E_0. The threshold energy value will, however, be refined later in the EXAFS analysis, so the position of E_0 in Athena can be chosen somewhat arbitrarily as long as the positioning is consistent throughout all the scans. The ”pre-edge range“ and ”normalization range“ parameters define regions before and after the edge respectively. The data in the pre-edge region is fitted by a linear function while the data in the normalization range is fitted with a polynomial. The normalization constant, $\mu_0(E_0)$, is evaluated by extrapolating the pre- and post-edge lines to E_0 and subtracting the value of where the pre-edge line crosses E_0 from the value from where the post-edge line crosses it. This gives the value of the ”edge-step“ parameter (see Figure 2.19. The pre-edge line is extrapolated to all energies in the data range and subtracted from $\mu(E)$. This operation puts the pre-edge region of the data on the y=0 axis.

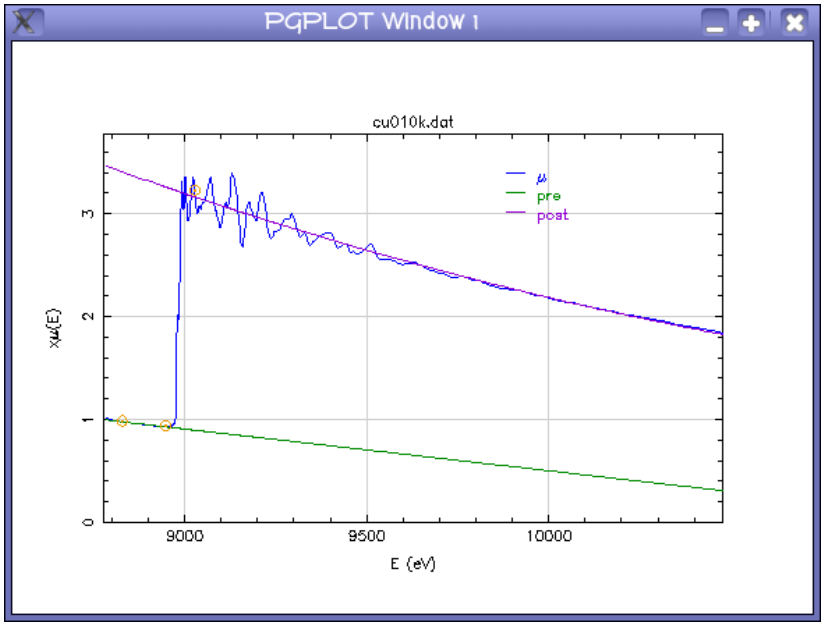

Figure 2.19: EXAFS scan with pre- and post-edge line used for normalizing data. Adapted from the Athena user's guide.[2]

The background absorption (the smooth absorption function that would appear if no neighboring atoms were present) is the part of the absorption spectrum which does not contain any structural information. It is derived by means of a polynomial or spline fit. Roughly speaking, the background is determined by optimizing the components of low frequency of the Fourier transform of the data. The cutoff frequency below which the optimization happens is determined by the parameter "Rbkg". The spline is varied so that the transform spectrum between 0 and Rbkg is optimized. This mean that a part of the spectrum is minimized. Background removal is a crucial part of the data reduction as it can lead to unsuccessful EXAFS refinements if not properly removed.

After normalization and proper background removal, the experimental absorption data ($\mu(E)$) in energy space is converted to $\chi(k)$ in k-space by Eq. 2.8.

2.3.7 Peak fitting

Modelling of the peak areas was performed using the peak fitting software *fityk 0.8.6*.[61] The XANES are fitted with an Arctan (step-like) function and one or two

Gaussian functions for the peaks in the data. fityk uses a Levenberg-Marquart nonlinear least-squares minimization algorithm to optimize the parameters. An illustration of the peak-fit procedure can be seen in Figure 2.20.

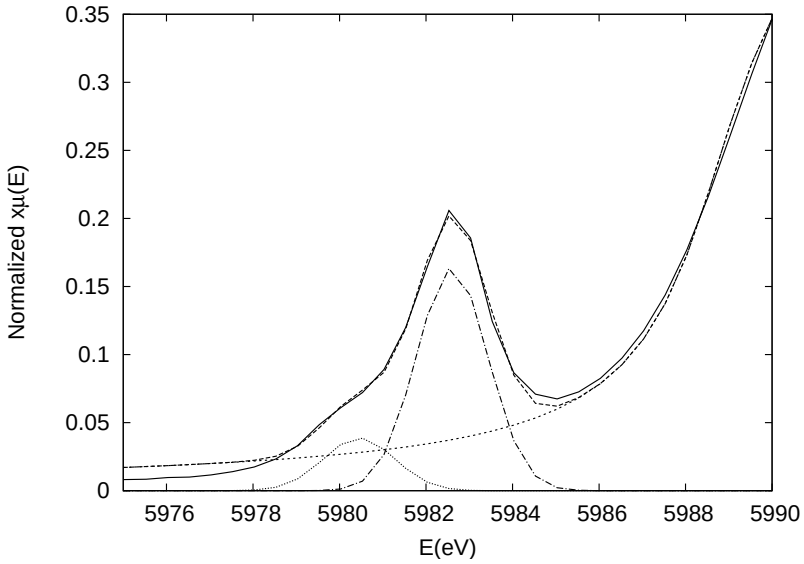

Figure 2.20: Illustration of the pre-edge peak fitting procedure.

The Arctan and Gaussian functions are given in Eq. 2.14 and 2.15 respectively.

$$f(x) = A \times \frac{\arctan\left(\frac{x-B}{C}\right)}{\pi + 0.5} \tag{2.14}$$

$$f(x) = A \times \exp\left[-ln(2) \times \left(\frac{x-B}{C}\right)^2\right] \tag{2.15}$$

where A is the height, B is the centeroid, and C is the half maximum full width (HMFW).

The best fit was found by noting the R^2 factor, which is defined by:

$$R^2 = 1 - \frac{\sum(data - fit)^2}{\sum data^2} \tag{2.16}$$

where the sums are over the data points in the fitting region. R^2 ranges from 0-1, 1 being the best fit.

2.3.8 Data analysis[59]

The goal for the analysis of EXAFS is to extract structural information (interatomic distances, multiplicity, and Debye-Waller factors) for the coordination shells of interest. Structural information via EXAFS depends on the viability of resolving the data into individual waves, each corresponding to the different types of neighbors of the central atom. This can be accomplished by two different techniques; *curve-fitting* or *Fourier-transform techniques*. Curve-fitting involves finding the best fit of the data with a sum of individual waves modeled by empirical equations derived from Eq. 2.9. Each wave contains structural parameters for each neighbor. When performing a Fourier transform, the $k^n\chi(k)$ is transformed from k space to r space. Each peak in the Fourier transform represents a coordination shell. To perform these analyzes, the EXAFS refining software EXCURV98[59] was used.

EXCURV98 employs a least squares fitting routine, by which a theoretical model ($\chi_{th}(k)$) can be can be fitted to the experimental spectrum ($\chi_{exp}(k)$). Calculations are performed using the small atom theory, described by the EXAFS equation (2.10). Before structural information can be extracted, the other parameters in the EXAFS model must be known. The backscattering amplitude (F) and the phase shift (ϕ) are derived from *ab initio* calculations using the Hedin-Lundquist formalism. This also accounts for the losses due to inelastic scattering ($e^{\frac{-2r_j}{\lambda_j(k)}}$). The amplitude reduction factor $S_i(k)$ (named $AFAC$ in EXCURV98) is only approximated by the Hedin-Lundquist potential. Only two parameters can be refined at the same time, and because the total amplitude consists of three correlated functions (N_j, σ^2 and $AFAC$), the AFAC must be determined using a model compound with known structure. The value of $AFAC$ may then be transferred to the unknown samples (with a structure similar to the model) so that the other parameters may be refined.

The dampening of the EXAFS amplitude at high k can be compensated for by weighting $\chi(k)$ by a power of k; $k^n\chi(k)$, where $n = 1, 2,$ or 3. This gives the high k region exponentially higher weights. Weighting spectra prevents the larger amplitude oscillations from dominating smaller ones when determining interatomic distances which depend on the frequency of the EXAFS, not the amplitude. The recommended weighting schemes with respect to the backscatterer are: $n = 1, 2,$ and 3 for Z > 57, 26 < Z < 57, and Z < 26 respectively.[46]

Fourier transformation of the EXAFS separates the contributions of individual coor-

dinations shells visually. It provides a simple physical picture of the local geometry around the absorbing atom. The position of the peaks in the FT spectra indicate the gives a representation of the interatomic distances, and the magnitude of the peaks are related to the coordination number. It must be kept in mind that EXCURV98 does not fit the FT spectrum, only $\chi(k)$. The individual waves can be separated further by Fourier filtering. A single peak in the FT spectrum may be filtered out and backtransformed into k space. Fourier filtering removes high frequency noise and residual background and provides equally-spaced data points in k space. Such spectra are useful when trying to identify the type of backscatter, however, they should not be refined as the filter is only applied to the experimental EXAFS and not the calculated EXAFS. This makes comparisons between the experimental and calculated EXAFS incorrect, since the filter may distort the EXAFS contribution of one or more scatterers.[62]

The quality of the fit is indicated by the R-factor defined in Eq. 2.17.

$$R_{exafs} = \sum_{i}^{N} \frac{1}{\sigma_i} (\mid \chi_i^{exp}(k) - \chi_i^{th}(k) \mid) \times 100\% \tag{2.17}$$

An R-factor of around 20% would indicate a reasonably well fitted $\chi(k)$.

The quality of the fit can be improved by increasing the number of refined parameters, however, it is important to keep in mind that the best fit is not necessarily chemically valid even though it is it mathematically satisfying. The number of refined parameter must therefore be less than the number of independent parameters:

$$N_{ind.par.} = \frac{2\Delta r \Delta k}{\pi} + 2 \tag{2.18}$$

where Δr is the distance over which data are refined, and Δk is the k-range.

Several factors affect the accuracy of the structural parameters obtained from EXAFS analysis. Among these are complexity and disorder of the system, quality of data, choise of model compound, data range etc.. The analysis of the CrAPO-5 materials in this work is somewhat complicated as chromium exists in mixed environments. Care need therefore be taken when analyzing these materials.

2.3.9 Limitations of XAS[55]

XAS is very sensitive to short range (r = 1-5Å) information but unlike PXRD it does not provide information on long range order in crystalline solids. As EXAFS data often need to be processed over a wide k-range (in order to detect as much structural information as possible) problems may arise at large values of k where the signal can be very noisy as a result of a dampening of the amplitudes of the EXAFS sine waves. As a result of this the R-factor (which represents the quality of the fit) will increase and the structural parameters obstained will be less trustworthy. Standard deviation for bond lengths are ± 0.01Åfor small values of r.

Due to its limited resolution, it is also difficult to separate bonds with similar lengths. Different coordination shells may appear as a single peak in the Fourier transform if their bond lengths are similar; it is thus important to try and determine by other means than from the FT whether the results from an EXAFS analysis makes chemical sense or not.

Elements with similar atomic mass numbers (Z) are hard to separate, and it is virtually impossible to make a distinction between to elements that are neighbors in the periodic table. Unless a considerable amount of information is already known about the system, it is not easy to differentiate between a reduction in coordination and an increase in disorder, particularly disorder that cannot be described by an effective Debye-Waller factor.

All elements can in principle be characterized by this technique, but elements with K- and L- edges below 2500 eV are hard to analyze. Soft X-rays ($\leq$2500 eV) are absorbed by air and will thus give inaccurate values for the absorption of the material. Elements for which this limitation applies include aluminum, phosphorus, oxygen, nitrogen and carbon. The flux distribution of the synchrotron source and type of monochromator are factors that can cause problems in the working energy ranges. XAS is also very sensitive to system disorder.

2.4 Raman Spectroscopy[10;63]

Raman Spectroscopy is based on the Raman effect and is used to study vibrational, rotational and other low-frequency modes in a system. The Raman effect arises when

a photon incident on a molecule interacts with the electric dipole of the molecule. The electric field may induce an electric dipole in the molecule of interest. For a transition to be Raman active, the polarizability of the molecule must change. Raman scattering can be decribed as an excitation to a virtual state lower in energy than the real electronic transition. Almost coincident with the excitation relaxation occurs accompanied by a change in vibrational energy. The process of exciting crystal and molecular vibrations is called Stokes scattering and the process that annihilates existing vibrations is called anti-Stokes scattering. An energy diagram illustrating this is given in Figure 2.21.

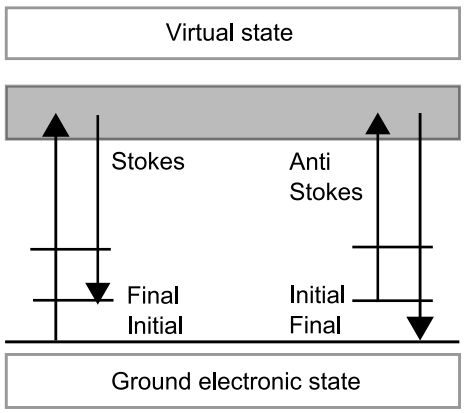

Figure 2.21: Raman scattering: Stokes (left) anti stokes (right).

Crystals and atoms can be pictured as balls (atoms) connected into larger systems by springs (chemical bonds). These systems may start vibrating with frequencies determined by the mass of the balls (atomic weight) and by spring constant, i.e. the stiffness of the spring, which is equivalent to the bond force constant. Diatomic molecules such as HCl, O_2 and CO, have only one fundamental vibrational frequency. The same holds for diatomic crystals, which contain repeating units of diatomic molecules. The number of vibrational modes for crystals, linear and non-linear molecules is given in Table 2.4

where n is the number of atoms in the molecule or within the primitive unit cell of the crystal.

The mechanical crystal and molecular vibrations are placed in the infrared (IR) region of the electromagnetic spectrum, in the frequency range of 10^12-10^14 Hz (3-300 μm wavelength). Coupling between the electronic structure of the chemical

Table 2.4: Number of vibrational modes based on geometry

Geometry	No. of vibrational modes
Crystal	$3n$-3
Linear	$3n$-5
Non-linear	$3n$-6

bond and incident IR radiation produces an IR absorption spectrum. The Raman spectrum arises as a consequence of indirect coupling of high-frequency radiation (visible light, ultraviolet and infrared) with the electron clouds making the chemical bonds. The physical processes and the selection rules of IR absorption and Raman are different although both techniques measure the vibrational spectra of materials. However, both give information about the details of chemical bonding and atomic arrangements. The Raman spectrum is sensitive to bond lengths, strength (e.g. double vs. triple bond), and arrangement of bonds in a material, but not so much to chemical composition.

A simplified setup of the Raman scattering experiment is shown in Figure 2.22

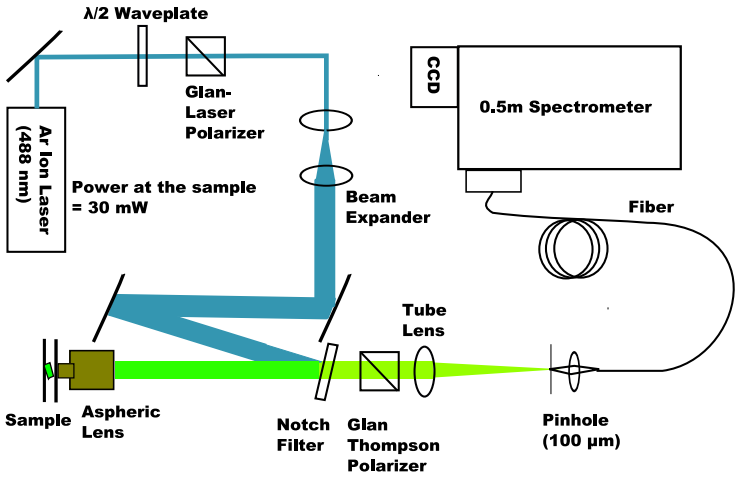

Figure 2.22: Simplified setup of an Raman scattering experiment.

The radiation source is most commonly a continuous gas laser (e.g. argon, krypton and He-Ne lasers). The output from the laser is polarized. A polarization rotator

controls the polarization orientation with respect to the sample. After the beam hits the sample, the output data are recorded and may be further analyzed. Various substances may be analyzed using Raman technology, be it in the form of a powder, liquid, solution or solid.

When the monochromatic beam hits the sample, the electron clouds that make up the chemical bonds in the sample are distorted due to the electric field of the incident radiation. When the wave passes the electric field is reversed, causing the distorted electron clouds to relax and release the stored energy. Most of the stored energy is emitted at a frequency equal to that of the incident beam. This component gives a strong line centered in the middle of the Raman spectrum (see Figure 2.23. Such scattering is known as Rayleigh scattering. A small portion of the stored energy is transferred to the sample, exciting the vibrational modes. These energies are subtracted from the energy of the incident beam. Weak side bands known as Raman lines appear in the spectrum at frequencies less than that of the incident beam. By measuring the separation between the Raman lines and the Rayleigh line, the vibrational frequencies of the sample is obtained. Vibrations that have been thermally excited can be annihilated by coupling with the incident beam. These vibrations appear as side bands at higher wavenumbers.

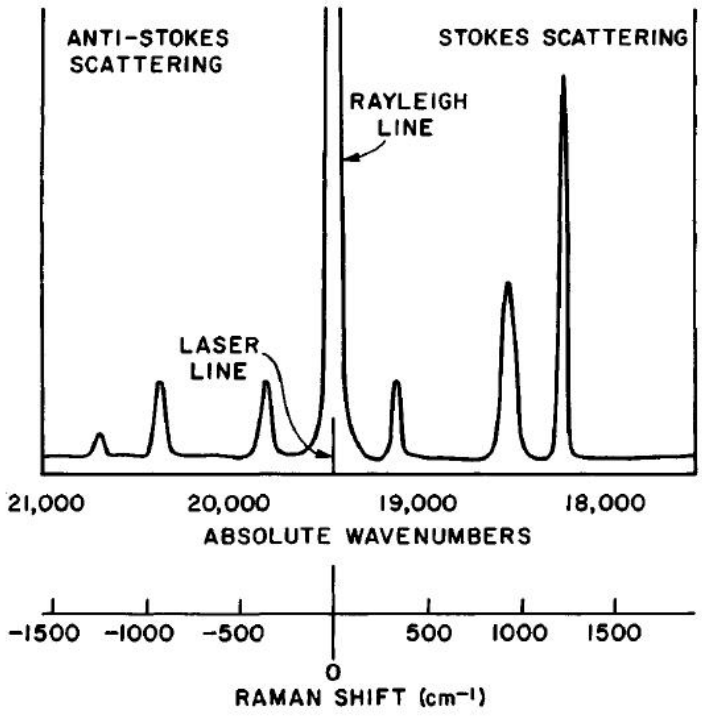

Figure 2.23: Raman spectrum showing Stokes and anti-Stokes scattering in addition to the Rayleigh line.

Raman spectroscopy has limited inorganic information and is typically not quantitative. Fluorescence radiation, which is much more intense than the Raman signal, can limit the usefulness of Raman.

Under ambient conditions, good quality data can be obtained from zeotypes down to 100 cm^1 by using longer exposing times to "burn out" interfering background luminescence. Thermal treatments of such materials increase the luminescence due to a possible increase of hydroxyl defects.[64]

2.5 Infrared Spectroscopy[65]

Infrared spectroscopy is a very versatile experimental technique. It is relatively easy to obtain spectra for samples in various phases (i.e. gases, liquids, and solids). Traditionally, since the 1940s, dispersive instruments has been used to obtain infrared spectra. In present time, however, Fourier-transform infrared (FTIR) spectrometers

are predominantly used. FTIR spectroscopy is based on the idea of interference of radiation between two beams creating an interferogram. The interferogram is a signal produced as a function of the change of the pathlength between the two beams. The distance and frequency are interconvertible by Fourier-transformation. The basic components of an FTIR spectrometer are shown in Figure 2.24. Radiation from the source is passed through an interferometer to the sample before reaching a detector. In the amplifier, the high-frequency contributions are eliminated by a filter. The data are then converted to digital form by an analog-to-digital converter and sent to a computer for Fourier-transformation.

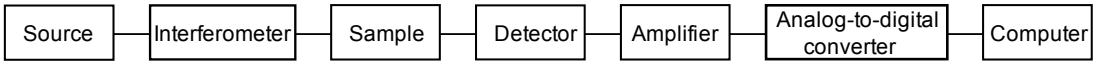

Figure 2.24: Basic components of an FTIR spectrometer.

The interferometer (Michelson interferometer) consists of two plane mirrors; one is fixed and the other can move in a direction perpendicular to the plane (see Figure 2.25). The beamsplitter, which is a semi-reflecting film, bisects the plane of the two mirrors. When a collimated beam of monochromatic radiation passes through an ideal beamsplitter, 50% of the incident beam will be reflected to one of the mirrors while the remaining 50% will be transmitted to the other mirror. The two beams are reflected off of these mirrors, returning to the beamsplitter where they recombine and interfere. Fifty percent of the beam reflected from the fixed mirror is reflected back to the source while 50% is transmitted through the beamsplitter. The beam leaving the interferometer at 90°to the input beam is called the transmitted beam and it is this beam that is detected in FTIR spectrometry. The moving mirror gives an optical path difference between the two arms of the interferometer. The two beams will interfere destructively in the case of transmitted beam and constructively in the case of the reflected beam for path differences of $(n + 1/2)\lambda$ producing an interference pattern.

To obtain an FTIR spectrum one must produce an interferogram without a sample in the beam and transforming the interferograms into spectra of the source with and without sample absorptions. The ratio between these two corresponds to a double-beam dispersive spectrum.

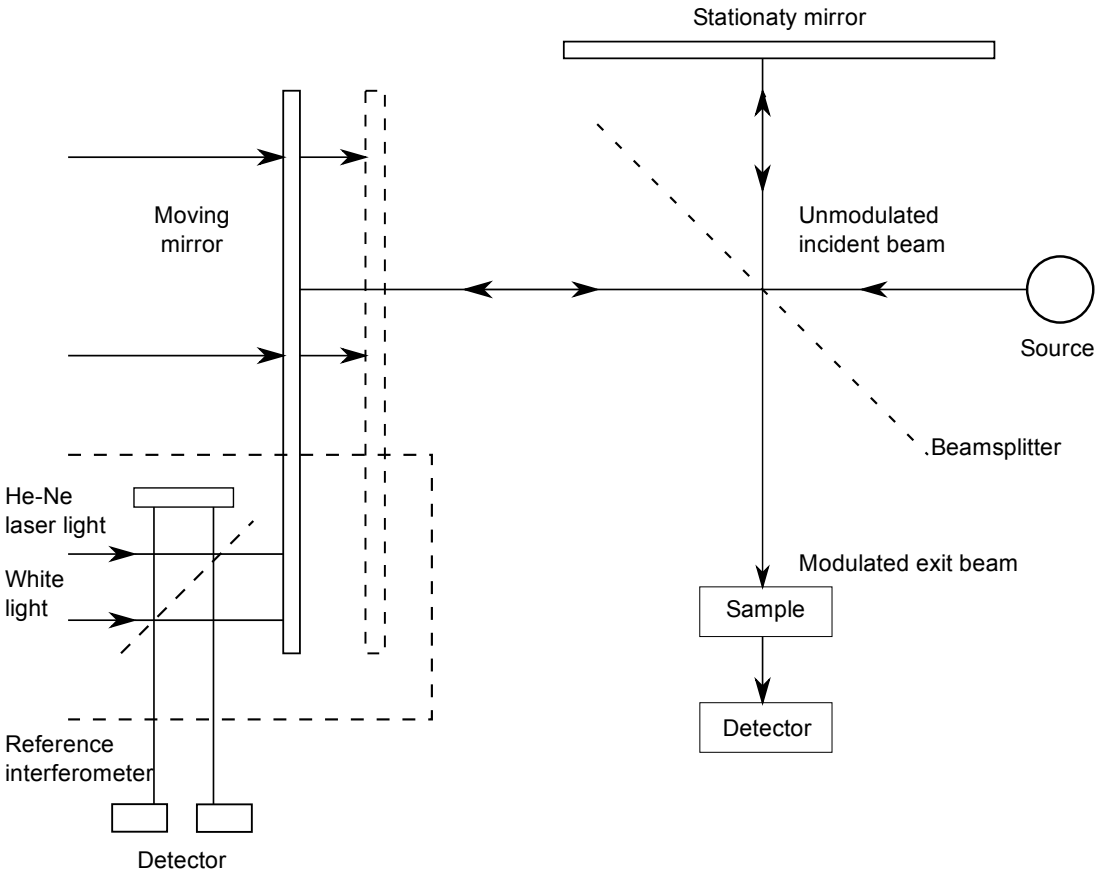

Figure 2.25: Schematic of an Michelson interferometer.

FTIR have several advantages to consider. First of all, all of the spectral elements are measured simultaneously which means that a spectrum is obtained very quickly. This in turn leads to a better signal to noise ratio in the same time compared with an older dispersive instrument. It is possible to collect many spectra and add them together to increase the signal to noise ratio. Spectral subtraction can be performed easily, e.g. remove the spectra of a solvent to obtain that of the solute.

Some disadvantages also have to be kept in mind. The FTIR instrument measure interferograms, not spectra. A Fourier-transform has to be performed to obtain a spectrum and the way the interferogram is transformed may affect the results. If noise occurs in one part of the radiation from the infrared source, it will spread throughout the spectrum. This limitation does, however, not apply in mid-infrared systems.

2.6 Thermogravimetric analysis[66]

Thermogravimetric analysis (TGA) is a technique which measures the amount and rate of change in the weight of a material as a function of temperature or time in a controlled atmosphere. Measurements are used primarily to determine the composition of materials and to predict their thermal stability. This technique can characterize materials that exhibit weight loss or gain due to decomposition, oxidation, or dehydration. The apparatus is called a *thermobalance* (or a thermogravimetric analyzer) which has four major parts (see Figure 2.26):

- the electrobalance and its controller
- the furnace and temperature sensors
- the programmer or computer
- the recorder, plotter or data acquisition device.

The sample is loaded in a small pan and is placed in an electrically heated oven with a thermocouple to measure the temperature. The atmosphere may be purged with an inert gas to prevent undesired reactions. A computer is used to control the instrument and to record data.

In addition to weight changes, some instrument also record the heat flow into the sample pan compared to that of the reference pan. This is referred to as *differential scanning calorimetry* (DSC), which measures the temperature and heat flows associated with transitions in materials as a function of time and temperature. DSC data provide information about chemical and physical changes that involve exothermic and endothermic processes. The instrument may also be coupled with a mass spectrometer in order to quantitatively measure material decomposition products.

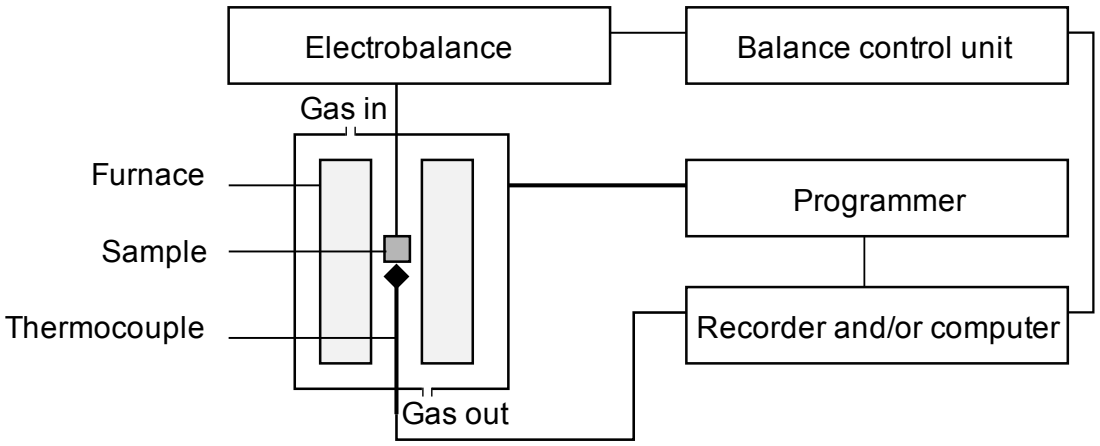

Figure 2.26: The basic parts of a thermogravimetric analyzer.

2.7 Inductively coupled plasma mass spectroscopy[67;68;69]

Inductively coupled plasma mass spectroscopy (ICP-MS) was introduced in the 1970s and is today a widely used technique for determining elements using mass spectrometry from ions generated by an inductively coupled plasma. It is a so-called "wet" sampling method because the samples must be digested prior to analysis in order to dissolve the element(s) of interest.

Samples are continuously introduced into the plasma via a *nebulizer* which converts the liquid into a fine spray of droplets called an *aerosol*. The argon plasma is then used to generate ions (usually as singly charged positive ions) that are introduced to a mass analyzer. These ions are then separated and collected according to their mass-to-charge ratios (m/z) to produce a mass spectrum. The atoms of an unknown sample can then be identified and quantified. A block diagram of an ICP-MS system is given in Figure 2.27.

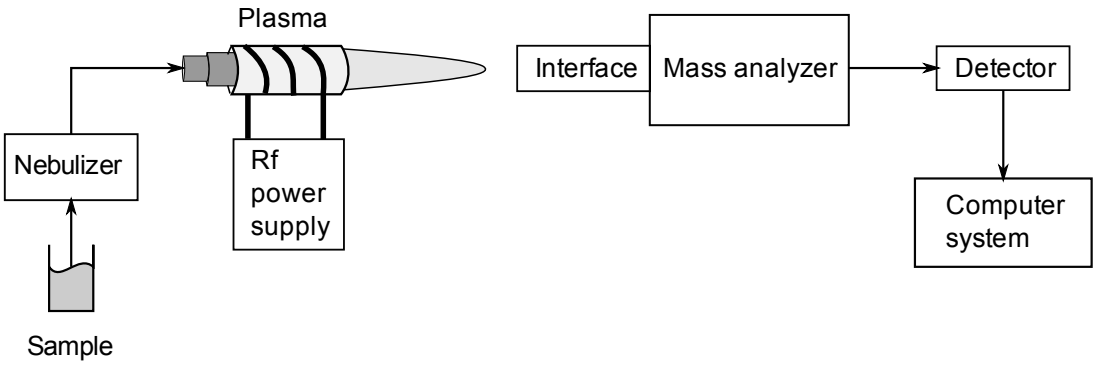

Figure 2.27: Block diagram of an ICP mass spectrometer system.

The resolution (R) of a mass analyzer is:

$$R = \frac{m}{\Delta m} \tag{2.19}$$

where m is the nominal mass and Δm is the mass difference that can be just resolved. A resolution of 100 means that unit mass (1 AMU) can be distinguished at a nominal mass of 100. A High Resolution ICP-MS can run at low, medium or high resolution (resolution of 300, 4,000 and 10,000 respectively). High mass resolution allows interference free measurements. The detection limit for chromium is less than 1 ppt when using hot plasma, and less than 100ppq when using cold plasma.

2.8 Scanning electron microscopy[70]

The scanning electron microscope (SEM) images sample surfaces by scanning it with an electron beam. The resulting signals (secondary electrons) from the sample contain information such as sample topography, morphology and composition. Non-conductive samples can be sputter-coated to increase the number of secondary electrons emitted from the sample. It is now possible to achieve a resolution of 0.5 nm using a High Resolution SEM, which is close to that of transmission electron microscopes.

The sample is investigated by a beam of electrons that are scanned repeatedly across the surface dwelling at some points for a period of time. Radiation from the sample is detected, amplified and used to modulate the brightness of a second beam of

electrons. The second beam is then synchronized with with the first one and used to excite an image on a cathode ray tube display (CRT). That image may then be photographed. SEMs provide three dimensional images because it records (in its normal mode) not the electrons passing through, but the secondary electrons that that are released when the incident beam hits the sample. Backscattered electrons, which can escape from much deeper regions of the sample, may also be detected together with secondary electrons. As the backscattered electrons are produced in a much greater region than secondary electrons, the resolution of backscattered electron images will be considerably lower than that of secondary electron images. The main components and the mode of operation of a simple SEM is shown in Figure 2.28.

The electron beam is produced by an electron gun (most commonly tungsten thermionic types) that provides a small electron beam with a large stable current. This beam is focused by electromagnetic lenses (condenser lens and objective lens) and the apertures to a tiny sharp spot. Smaller beam diameter gives better resolution, but also lower signal-to-noise-ratio. The scan coils are responsible for moving the electron beam back and forth over the sample (referred to as raster) and is synchronized with the CRT via the scan generator.

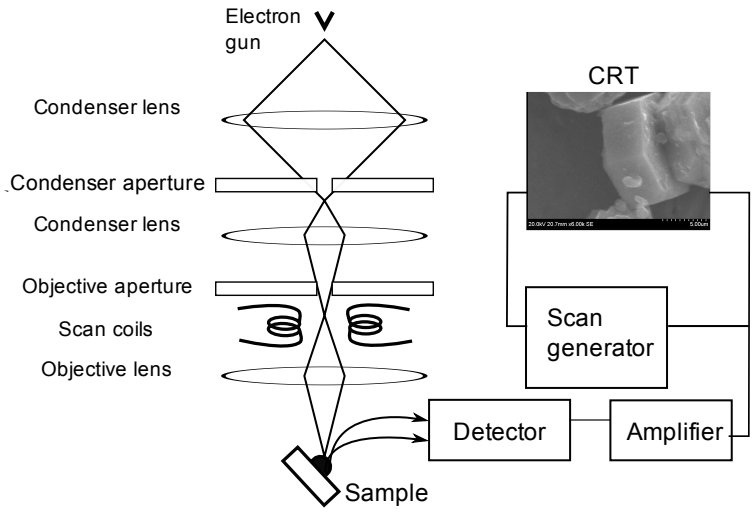

Figure 2.28: Schematic diagram showing the main components and the mode of operation of a simple SEM

Chapter 3

Experimental

3.1 General procedure for the synthesis of CrAPO-5

Three general procedures were used for the syntheses of CrAPO-5. The focus in the two first methods was to vary the chromium source (and the amount of chromium added) to see if that had any impact on the structure. A different template and a different mixing order was used in method 2. The third method differs significantly from the others because of the use of an additional template. All methods are described below. From this point on, samples synthesized using method 1, 2 and 3 will be denoted CrAPO-5/1, CrAPO-5/2, and CrAPO-5/3 respectively.

3.1.1 Method 1; CrAPO-5/1

A diluted acid solution was made by mixing orthophosphoric acid (H_3PO_4, 85 wt%, 10.85 g, Sasol North America Inc.) with deionized water (H_2O, 18.50 g) with stirring for 50 minutes before the chromium source, a metal salt was added with further stirring for for 6 hours. Three different sources of chromium(III) were used; chromium(III)acetate ($Cr(CH_3COOH)_3$, Riedel-de Haën AG), chromium(III)chloride ($CrCl_3$, Riedel-de Haën AG), and chromium(III)nitrate ($Cr(NO_3)_3$, The British Drug Houses Ltd.). The amount of chromium added was also varied, as can be seen in Table 3.1.

The reaction gels turned black upon addition of $CrAc_3$ and $Cr(NO_3)_3$, while addition of $CrCl_3$ resulted in a bright green color. The pH of the reaction mixtures at this point

was between 0 and 1. Pseudoboehmite (Al_2O_3, Capital B Alumina, 99%, 7.50 g, Sasol North America Inc.) was slowly added to the reaction mixture with vigorous stirring. Triethylamine ($N(CH_2CH_3)_3$, 12.20 g, Sigma-Aldrich Chemie) was added last, and the mixture was stirred for 24 hours. The compositions of the gel mixtures are given in Table 3.2.

The resulting gel was placed in an autoclave and heated to 190°C for 20 hours. Last, the product was filtered, washed with deionized water and dried at 100°C. Half the amount of powder obtained was calcined at 550 °C for 999 minutes (ramp rate: 1°C/min).

Table 3.1: Varying parameters in synthesis method 1

Experiment no.	Chromium source	Amount added (g)	Color of mixture	pH
1	$CrAc_3$	1.47	Black	0
2	$CrCl_3$	1.51	Bright green	0.5
3	$Cr(NO_3)_3$	1.50	Black	0.5
4	$Cr(NO_3)_3$	3.00	Black	1
5	$Cr(NO_3)_3$	0.75	Black	0.5

Table 3.2: The uniform gel composition ratios

Experiment no.	The uniform gel composition ratio Cr_2O_3:Al_2O_3:P_2O_5:TEA:H_2O
1	0.06 : 1.5 : 1 : 2.5 : 25.9
2	0.07 : 1.5 : 1 : 2.5 : 25.9
3	0.03 : 1.5 : 1 : 2.5 : 25.9
4	0.08 : 1.5 : 1 : 2.5 : 25.9
5	0.02 : 1.5 : 1 : 2.5 : 25.9

3.1.2 Method 2; CrAPO-5/2

A solution was formed by dissolving orthophosphoric (5.85 g) acid in water (13.50 g) with stirring for 20 min. Pseudoboehmite (2.50 g) was then added to the resultant mixture with vigorous stirring (magnetic stirring plus hand swirl at the beginning,

followed by magetic stirring). The mixture was stirred for 2 hours. A solution of chromium(III)nitrate in water (7.80 g) was then added to the pseudoboehmite gel with stirring for 70 hours. Tripropylamine ($N(CH_2CH_2CH_3)_3$, 3.60 g, Sigma-Aldrich Chemie) was then added and the mixture was further stirred for 14 hours. The autoclave and drying procedure was the same as in Method 1 (3.1.1).

3.1.3 Method 3; CrAPO-5/3[36]

Pseudoboehmite (4.96 g) was suspended in deionized water (15.0 g), under constantly stirring. Orthophosphoric acid (11.53 g) was diluted with deionized water (15.0 g) and slowly added to the mixture. After stirring for 1 hour, a solution of chromium(III)nitrate (1.20 g) and water (15.0 g). Last, triethylamine (5.59 g) and acetic acid (CH_3COOH, 0.91 g, SUPPLIER) were added to the mixture and the stirring continued for two more hours. The molar composition of the gel was $0.03Cr_2O_3$:0.97:Al_2O_3:1.0P_2O_5:1.5TEA:50H_2O:0.3:AA.

The reacion gel was placed into an autoclave and heated to 190°C for 24 hours. The product was then filtered, washed with deionized water, and dried in air at 80°C. Half the amount of powder was calcined using same procedure as in section 3.1.1.

An alternative drying method was to dry the product at room temperature in air with a squirt of ethanol. These samples are given the name CrAPO-5/3b.

3.2 X-ray diffraction

The CrAPO-5/1 samples were identified by XRD on a Siemens D5005 X-ray powder diffractometer operating at 50 keV and 40 mA with constant slit opening. The diffractometer uses a Cu-tube as the X-ray source with Cu K_α radiation. XRD patterns were collected in the 2θ range of 5 to 45°, with a step size of 0.03°.

As prepared and calcined samples were ground to fine powder form with a mortar and pestle and mounted in sample holders. The crystal structures were identified by comparing the diffraction patterns with patterns in the powder diffraction file database supplied by International Centre for Diffraction Data (ICDD).

3.3 SEM

Scanning electron microscopy was used to investigate the CrAPO-5 crystals with respec to particle sizes, shapes etc.

A tiny amount of powder was dispersed onto a brass stub (sample holder) with a drop of ethanol and set to dry. As soon as all the methanol had evaporated, the samples were coated with a thin layer of carbon in a carbon coater (Agar Turbo Carbon Coater) in order to make them electrically conductive. They were then observed with a scanning electron microscope (a JSM-840 A, JEOL Ltd.) which has a magnification range of 10-300.000X and a resolution of 4 nm for secondary electrons and 10 nm for backscattering secondary elelectrons. The working acceleraltion voltage was between 20-25 kV.

3.4 ICP-MS

Solid samples for total elemental analysis are digested using using an acid/microwave procedure in order to dissolve the samples. A procedure involving solving the sample in hydrofluoric acid and nitric acid was tried, however, the procedure will not be described here as it lead to a false elemental composition using ICP-MS. Both the chromium and aluminum content were much lower than expected. This is most likely due to precipitation of chromium(III)fluoride and aluminum(III)fluoride which the ICP-MS cannot detect. Digestion in agua regia, which is a mixture of hydrochloric and nitric acid (HCl/HNO_3), was much more suitable for the CrAPO-5 compounds and will thus be described more in detail.

As contamination can play a significant role in sensitive ICP-MS experiments, all sample containers were washed thoroughly with MQ-water. After washing, the Teflon sample containers (PTFE vessels, 18 ml) were loaded with an appropriate amount of material (10-20 mg).

Concentrated HNO_3 (Supra pure, 40%, 0.7 $\pm$0.05 g) and HCl (1.65 $\pm$0.1 g) was added to the Teflon vessels and placed in a sample rack. After this pre-treatment, the mixtures were loaded into the microwave (UltraClave, Milestone) and heated under pressure in order to get complete digestion of the samples.

The sample mixtures were heated at a heating rate of approximately 7°C per minute

from room temperature to to 250°C and kept at 250°C for 40 minutes. The mixtures were cooled to 60°C (cooling rate was approximately 3.5°C per minute). The temperature profile is shown in Figure 3.1.

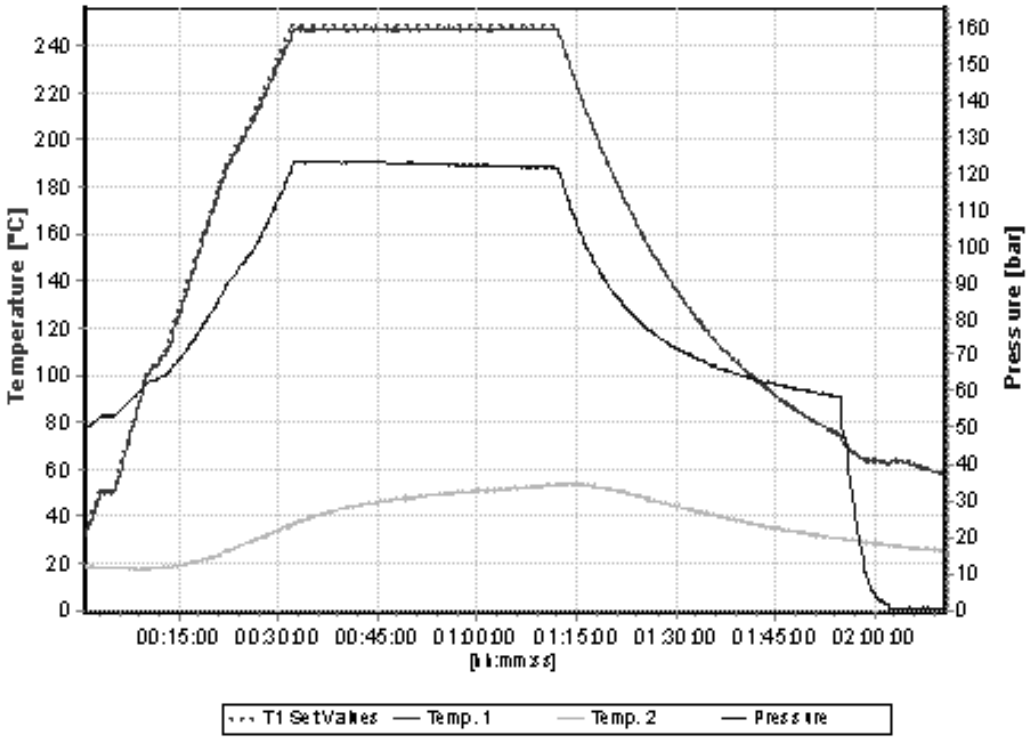

Figure 3.1: Temperature profile

The digested samples were then diluted to a final volume of 220 $\pm$0.5 ml/g, and placed in sample tubes for ICP-MS analysis.

The digested and diluted samples were analyzed with the ELEMENT2 High Resolution ICP-MS as described in Section 2.7. The ELEMENT2 is a high performance, double focusing magnetic sector field ICP-MS. It has a sensitivity greater than 1×10^9 counts per second (cps) per ppm In, and has a great detection power (less than 1 ppq for non-interfered nuclides). The analysis was run at low resolution.

3.5 TGA

Thermogravimetric analyses were performed on CrAPO-5/1, CrAPO-5/3, and CrAPO-5/3b to monitor the mass loss upon heating. The TGA analysis were carried out using a Perkin-Elmer Thermogravimetric Analyzer (TGA7). A Jupiter STA 449C was connected to a QMS 403V Aëolos Mass Spectrometer from Netsch to monitor the mass loss.

The CrAPO-5 sample (approximately 25 mg) was loaded in an Al_2O_3 pan. Temperature-programmed experiments were carried out at a heating rate of 2 K/min from room temperature to 550 K and kept at 550 K for 12 hours.

3.6 FTIR

FTIR spectra were obtained during the calcination processof CrAPO-5/3 in air in order to detect any possible acid sites and to monitor the template desorption from the cavities of the material.

The powder was pressed into a pellet using a manual sample press (manufactured by Graseby Specac Limited) and placed in a sample holder/cell. The spectra were recorded by a VERTEX 80 FTIR specrometer using OPUS 6.0 software. All spectra were run at 4000 cm^{-1} to 400 cm^{-1} (mid-infrared region) with 4 cm^{-1} resolution. The spectrometer aperture was set to 8 mm. The spectra were derived from 64 co-added scans at approximately 3 seconds per scan.

A background spectrum was recorded prior to the sample spectra in order to eliminate peaks that would "contaminate" the spectra. After that the sample was placed inside the IR spectrometer and scanned. Fourier transform calculations were then performed by a computer and the background spectrum was subtracted, leaving corrected spectra of the sample.

3.7 Raman

Raman spectra were recorded while running in situ XANES on CrAPO-5/1. The sample preparation procedure is described in Section 4.8.

The employed instrument was a dispersive spectrophotometer Renishaw RA100, with a 532 nm Ar-ion laser and a 1800 lines per millimeter grating. A standard Raman RP20V was connected to the instrument by optical fibers. The focusing of the laser on the sample was obtained using the camera on the Raman probe head.

The aquisition time was 140 seconds per scan, and the spectra were recorded over a range of 100-3700 cm^{-1}. The Raman data sets at room temperature were averaged by summing similar single scans to improve the signal-to-noise ratio. A background baseline correction of the spectra as well as identification of the peak positions were carrtied out using Renishaw software WiRE 2.0.

3.8 X-ray absorption spectroscopy

3.8.1 Experimental setup

The XAS data presented in this thesis were collected at the European Synchrotron Facility (ESRF) at the Swiss-Norwegian Beamplines (SNBL) and at MAX-lab, the Swedish National Electron Accelerator Laboratory for Synchrotron Radiation Research, Nuclear Physics and Accelerator Physics, at Lund University in Sweden.

X-ray absorption data for CrAPO-5 were collected in the transmission mode at the SNBL. Data were collected at the chromium K-edge at a 13 element Ge multi channel detector. The beamline (BM01b) uses a Si(111) crystal monochromator. No mirrors were used for the chromium experiments. The first ionization chamber detector (I_1, 17 cm) was filled with 20% N_2 and 80% He, and the second (It, 31 cm) with 90% He and 10% Ar. The electron beam energy was 6 GeV with a maximum current of 200 mA. EXAFS spectra were recorded with 5 eV steps below the absorption edge, 0.5 eV steps in the edge region, and steps equivalent to 0.05$Å^{-1}$ increments above the edge. Region borders were 5900, 5975, and 6020 eV. Multiple XAS scans were collected and summed.

XANES was measured with 5 eV steps below the edge, 0.25 eV in the edge region and, and steps equivalent to an increase of 0.1 eV above the edge (region borders were same as above). All XANES spectra were calibrated against chromium foil (5989 eV).

At MAX-lab, data were collected in fluorescent mode at the Material Science Beamline

I811 constructed at the MAX-II storage ring. I811 uses a double-crystal monochromator (manufactured by ACCEL) consisting of a pair of silicon single crystals (Si(111)/Si(311)) covering the energy range 2.3-20 keV. The MAXII storage ring operates at an energy of 1.5 GeV, with a maximum stored current of 280 mA. The fluorescence yield was collected using an ion-chamber detector (Lytle-detector).

The samples (typically 100-120 mg) were loaded in aluminum sample holders to a thickness of approximately 1 mm sealed with Kapton tape windows.

XANES and EXAFS spectra were recorded in separate runs.

3.8.2 In-situ measurements

A small portion of the sample (approximately 120 mg) was weighed out and placed between some quartz wool and two graphite/mica windows in an in-situ cell (see Figure 3.2 for illustration).

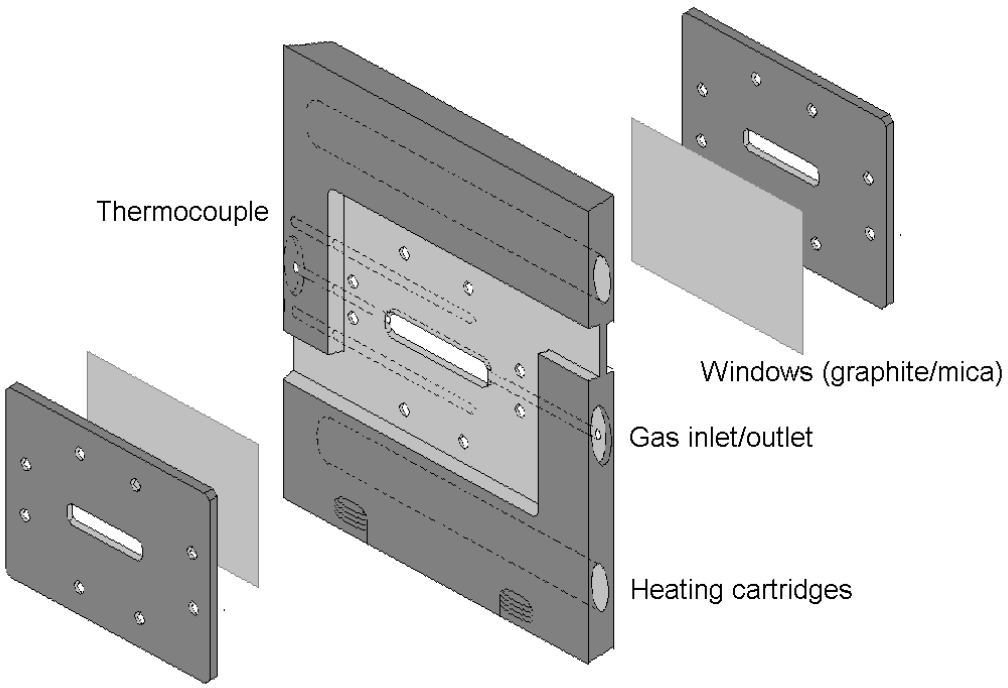

Figure 3.2: In situ cell for XAS/Raman experiments. (Illustration by Karina Mathisen).

Reaction gases flow through the sample via the gas inlet/outlet. Flow rates were controlled via flow meters. The sample was heated via a thermocouple by manually controlling the voltage. A simplified experimental set-up is given in Figure 3.3.

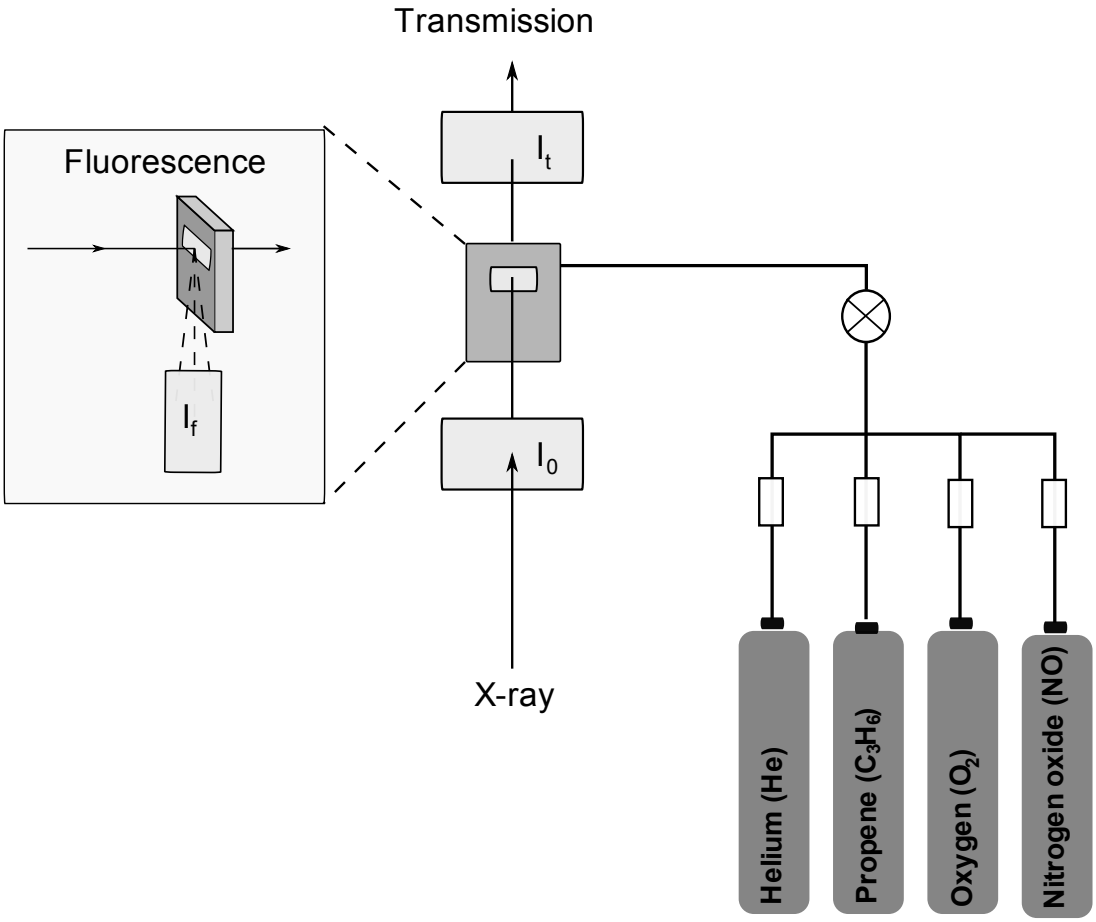

Figure 3.3: Experimental set-up for in situ experiments.

EXAFS scans were first collected at room temperature in air before the sample was heated to 150°C in He (15 ml/min) to remove water. Beamdump (loss of X-rays) occured when heating the sample between 50 and 119°C. No scans were therefore collected in that temperature range. XANES scans were then collected during heating and cooling of the sample in 43.6% propene in O_2 and 59.9% NO/O_2 respectively. The in-situ temperature range was aproximately 150-350°C for heating in propene/O_2 and 320-100°C for cooling in NO/O_2.

The in-situ experiments were collected in transmission and fluorescence mode at

SNBL and MAX-lab respectively.

Chapter 4

Results and discussion

4.1 Synthesis of CrAPO-5

One of the parameters varied in the synthesis of CrAPO-5 was the chromium source. Three different metal sources were used; chromium(III)chloride, chromium(III)acetate, and chromium(III)nitrate. The color of the as-synthesized samples were all pale green, typical for Cr^{3+} compounds. Different shades/intensities of color is observed due to varying chromium content. Upon calcination the color changes to yellow, characteristic for compounds with chromium in higher oxidation states, e.g. Cr^{6+} with traces of Cr^{5+}. The Cr^{6+} formed during calcination is most likely attached to the surface of the AlPO-5 as a chromate species with two extra oxygen ions.[9]

When using a co-template (CrAPO-5/3) the yellow color of the calcined sample is less intense and more greenish-yellow than actual yellow. The material also retains its color (green for as-prepared and greenish-yellow for calcined sample) better than those prepared by conventional methods when washed. It is thus more probable that larger quantities of chromium is incorporated into the framework and is resisting oxidation in these samples relative to the other samples.

The amount of chromium salt added to the reaction mixture seems to have little effect on the final product. The waste water that remained after washing the samples with higher chromium content had significantly greener color than that of the samples where less chromium salt was used. This indicates that there is an upper limit for how much chromium that can be incorporated into (or be bonded to) the framework.

The CrAPO-5/3 material dried at room temperature (CrAPO-5/3b) rather than at 80°C looked quite different from the other materials when calcined. Instead of turning yellow, it obtained a greenish-gray color. Green color indicates, as already mentioned, that chromium exists mainly in the trivalent form. It is not clear, however, if the temperature at which the material was dried had anything to do with chromium resiting oxidation, but this may suggest that removal of water at elevated temperatures prior to calcination affects the stability of chromium(III) in the molecular sieves.

The colors prior to and after calcination and effect of washing is summarized for all samples in Table 4.1.

Table 4.1: The uniform gel composition ratios

Sample	Color		Effect of washing	Drying temp.
	As-prepared	Calcined at 550°C		(°C)
CrAPO-5/1	Pale green	Intense yellow	Noticable color loss	100
CrAPO-5/2	Pale green	Intense yellow	Noticable color loss	100
CrAPO-5/3	Green	Pale yellow	Little color loss	80
CrAPO-5/1	Green	Grayish green	No noticable color loss	Room temp.

4.2 X-ray diffraction

Powder X-ray diffraction was performed on all synthesized materials (as-synthesized and calcined), mainly to identify their structures and hence possibly rule out some materials from further investigation (i.e. materials with diffracograms that do not confirm AFI structure).

The X-ray diffractograms of calcined CrAPO-5/1 synthesized using $Cr(NO_3)_3$, $Cr(Ac)_3$, and $CrCl_3$ are shown in Figure 4.1 a), b) and c) respectively, which all verify the AFI structure. Varying the source of chromium does not seem to have any major effects on the structure of the CrAPO-5, except for a slight increase of the relative intensity of the first peak when $Cr(NO_3)_3$ was used. The patterns illustrate a rather high crystallinity of the samples. There are no extra peaks related to chromium oxides, confirming the purity of the products. Furthermore, the XRD patterns of as-prepared

and calcined samples did not differ significantly from each other, indicating a stability of the products up to 550 °C.

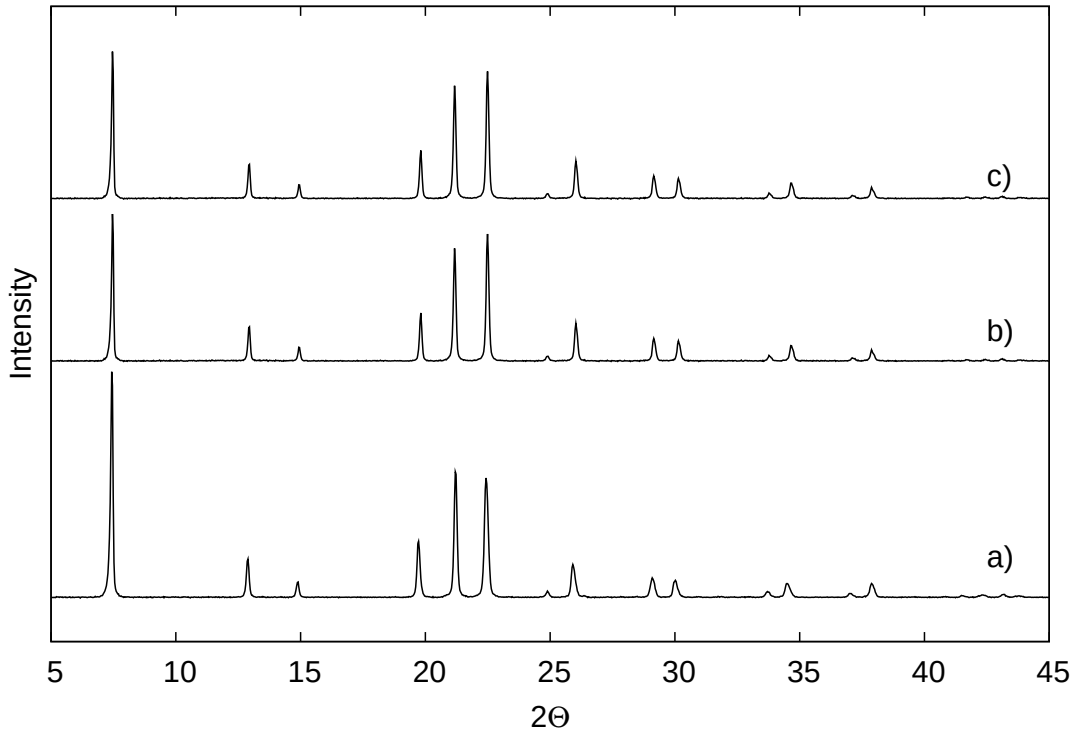

Figure 4.1: Normalized diffractograms of CrAPO-5 prepared using various sourced of Chromium; $Cr(Ac)_3$ a) as-prepared and b) calcined, c) $CrCl_3$ c) calcined, and $Cr(NO_3)_3$ d) calcined.

Diffractograms of calcined CrAPO-5/3 and CrAPO-5/2 are shown in Figure 4.2 a) and b) respectively. The CrAPO-5/2 was synthesized using TEA as template. Also for these samples the AFI structure is verified, and both are thermally stable up to 550°C. The slight difference in the order of mixing does not seem to have any noticable effect on the crystallinity of the material.

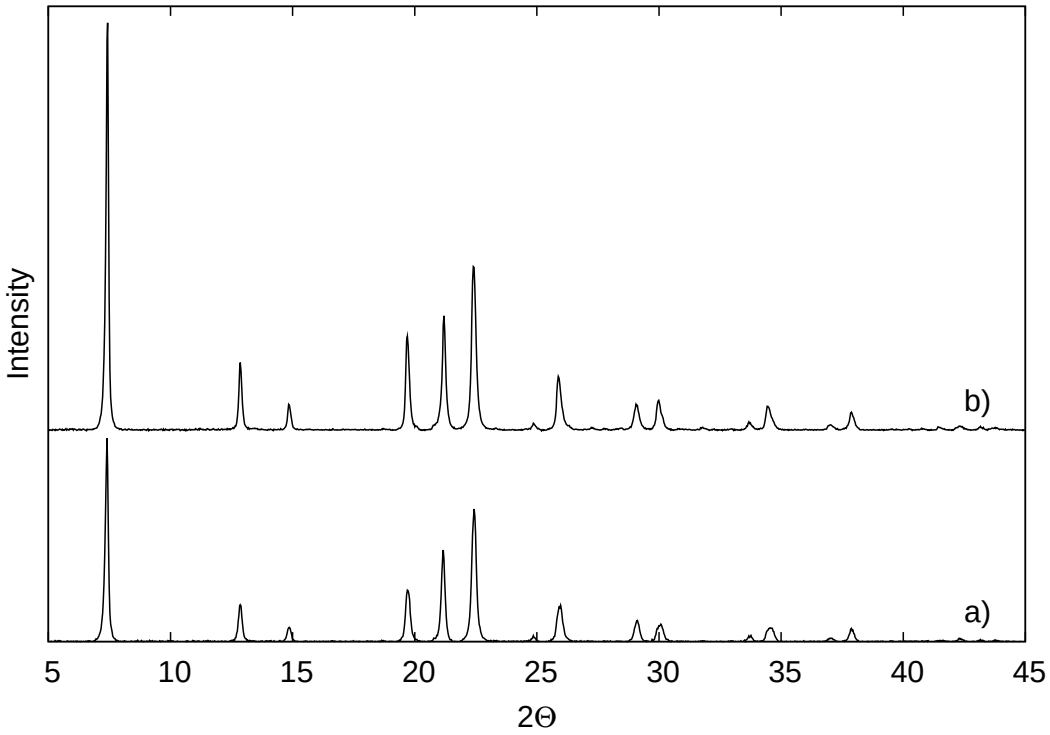

Figure 4.2: Normalized diffractograms of CrAPO-5/2 (a) and CrAPO-5/3 (b).

When using TEAOH as template, significantly lower crystallinity was obtained for the as-synthesized sample (Figure 4.3 a)), and upon calcination the structure collapses. The diffractogram in Figure 4.3b confirms berlinite ($AlPO_4$) structure. TEAOH seems therefore less suitable for the synthesis of CrAPO-5. It is, however, possible that different synthesis conditions (e.g. allowing longer time for crystallization, varying the pH with addition of water or acid etc.) could have a positive effect on the crystallization process. There is also the possiblity that TEAOH adapts a different conformation (as with the case of Zn and TEAOH described in Subsection 2.1.3) in the presence of Cr under the given conditions and thus acts as structure blocking rather than structure directing for CrAPO-5.

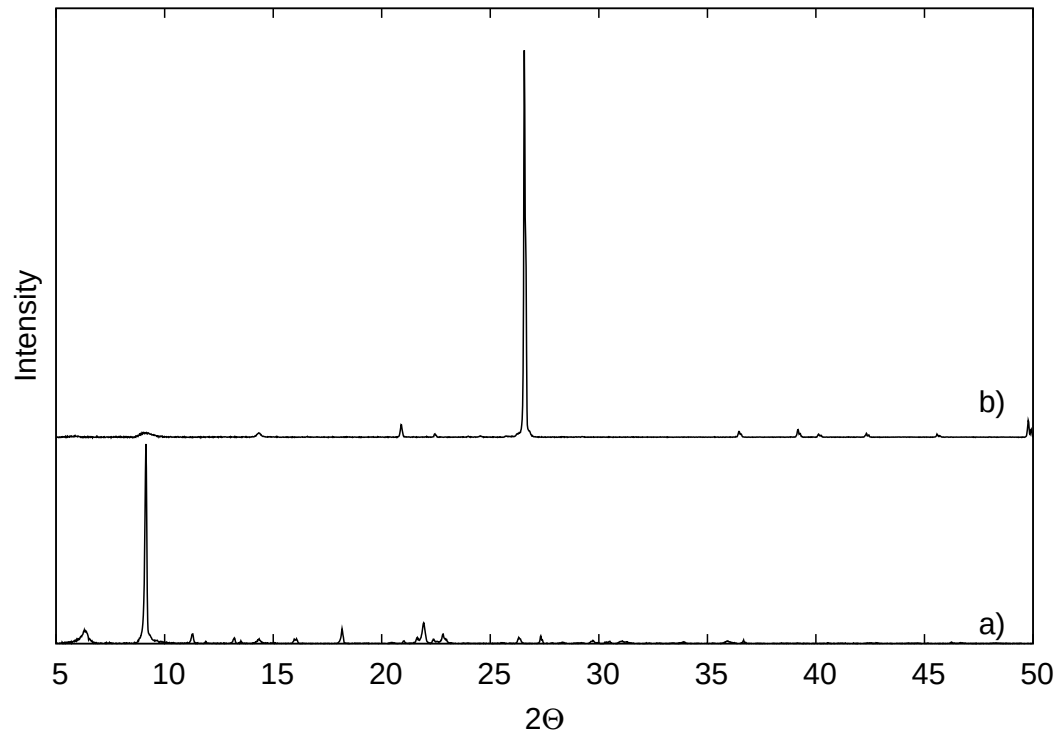

Figure 4.3: Normalized diffractograms of as-synthesized (a) and calcined (b) CrAPO-5/2 using TEAOH as template.

As the samples synthesized using methods 1 and 2 with TEA as template did not differ significanly from each other in color or crystallinity, only samples prepared by methods 1 (with chromium(III)nitrate) and 3 (with chromium(III)nitrate and co-template) were chosen to undergo further characterization. The CrAPO-5/2 was, however, studied under a scanning electron microscope to confirm similarities with CrAPO-5/1 with respect to crystal size and shape.

4.3 SEM

Scanning electron microscope images of typical CrAPO-5/1 (and CrAPO-5/2) crystals are shown in Figure 4.4. The crystals have a hexagonal rod-like shape with an *l:d* ratio much greater than 1. It is also very clear that the crystals are not very uniform or symmetric (is best seen in the image to the left). Some perfect crystals were found, however, these do not represent the average shape of the crystals in the sample.

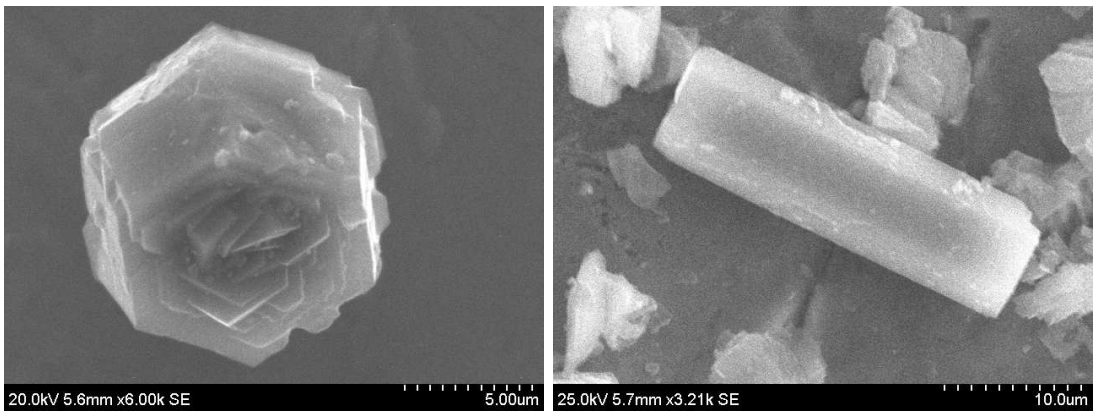

Figure 4.4: SEM images of crystals of typical shape for CrAPO-5/1.

The crystals of the CrAPO-5/3 samples (see Figure 4.5) are much more uniform and symmetric than those found in the CrAPO-5s. They also have *l:d* ratios less than one, which is in agreement with data found in litterature[38] for chromium substituted AlPO-5s. This property is also very favorable in optic materials.

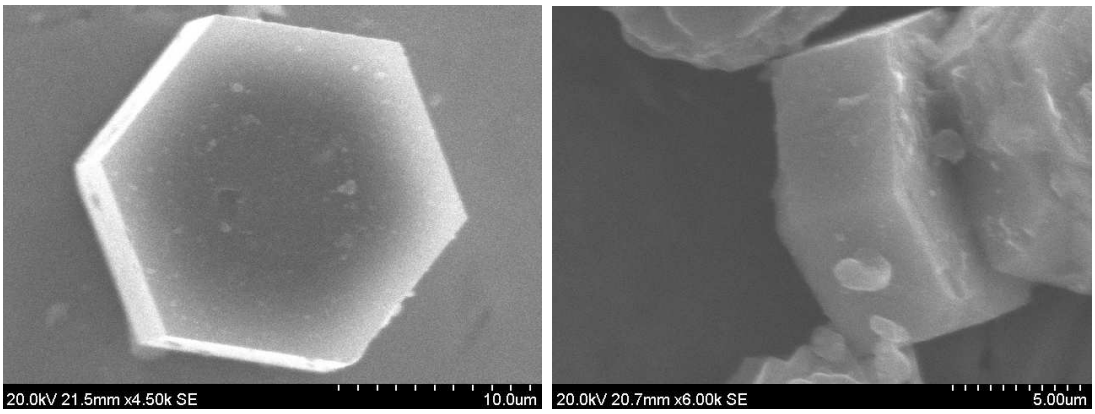

Figure 4.5: SEM images showing typical crystal shapes/sizes for CrAPO-5/3.

Crystals with an aspect ratio greater then one was also found in the CrAPO-5/3 material. This suggestes that the incorporated metal is not distributed evenly throughout the sample. The crystals are nevertheless clean-cut and symmetric, as apposed to those of CrAPO-5/1. See Figure 4.6 for a comparison of the two.

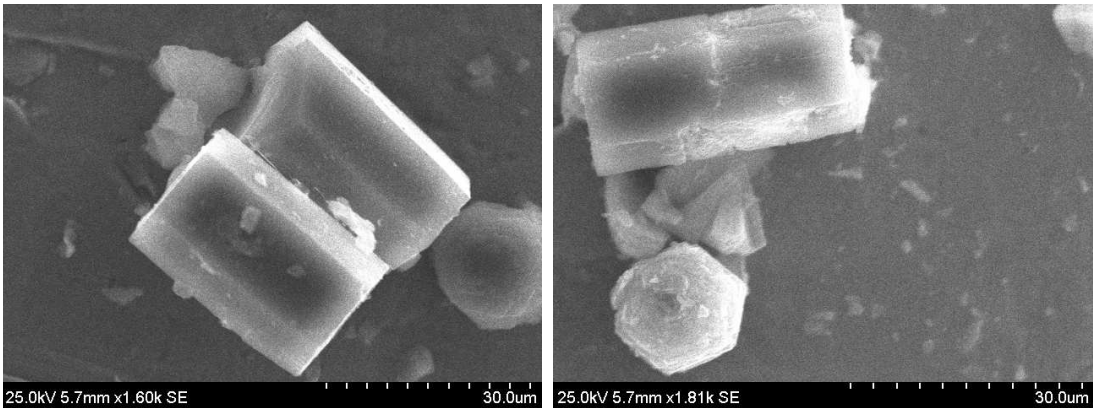

Figure 4.6: Crystal with an aspect ratio greater than one for CrAPO-5 (left) compared with that of a CrAPO-5/1 (right).

4.4 ICP-MS

Elemental composition analysis gives a good indication on whether or not chromium is substituted for aluminum in the framework by calculating the relative amounts of aluminum, phosphorus and chromium.

The results from ICP-MS analysis is listed in Table 4.2. All values are relative to the total amount of detected elements in the decomposed material (i.e. mmol per gram detected elements, not per gram AlPO-5). The ratios (Al:P and (Cr+Al):P), however, represents the actual molar ratio in the CrAPO-5. The standard deviations for Cr, Al, and P are 1.3, 1.2. and 0.4% respectively.

Table 4.2: Elemental composition of CrAPO-5.

Sample	Al (mmol/g)	P (mmol/g)	Cr (mmol/g)	Al:P	(Cr+Al):P	$Cr_xAl_yP_zO_4$
CrAPO-5/1	6.798	6.784	0.318	1.002	1.049	$Cr_{0.05}Al_{1.0}P_{1.0}O_4$
CrAPO-5/3	9.335	9.709	0.623	0.962	1.026	$Cr_{0.06}Al_{1.0}P_{1.0}O_4$
CrAPO-5/3b	8.856	9.582	0.691	0.924	0.996	$Cr_{0.07}Al_{0.93}P_{1.0}O_4$

Elemental composition analysis of CrAPO-5/1 revealed an Al:P ratio greater than 1. The (Cr+Al):P ratio is then ofcourse also greater than 1, suggesting that chromium has not taken the place of aluminum in the framework. It is therefore reasonable to

assume that chromium is present in relatively low amounts on the surface (or possibly within the pores) of the AlPO-5. These results are in concistency with the color observations made; the powder lost color when washed with water, hence confirming the presence of non-incorporated chromium.

More promising results were found for CrAPO-5/3, where the Al:P ratio is less than one, and the (Cr+Al):P ratio is closer to one than for the CrAPO-5/1. This ratio is, however, a little bit greater than one suggesting that not all the chromium has been substituted for aluminum. The CrAPO-5/3b revealed an even lower aluminum to phosphorus ratio, and a ratio closer to 1 when including chromium. This indicates that the synthesis was more successful with respect to incorporating the highest amount of chromium.

4.5 Raman

Combined in situ Raman spectroscopy and XAS was performed on calcined CrAPO-5/1 to possibly determine any acid sites present in the structure. The Raman spectrum recorded at room temperature shows a series of bands between 100 and 1240 cm^1 (see Figure 4.7). The most intense features are summarized in Table 4.3.

The intense bands between 100 and 300 cm^{-1} can be assigned to T-O-T (= Al and P) "ring breathing" and distortion modes. These bands are typical for AlPO-5s.[71;72;73] The region between 300 and 600 cm^{-1} belongs to the structure sensitive bands. The bands at approximately 400 and 500 cm^{-1} is present due to T-O-T bending. The band at 500 cm^{-1} is characteristic for zeolites and zeotypes containing exlusively even-numbered rings (4 MR, 6 MR, 8 MR or 12 MR). The presence of odd-numbered rings would have shifted this band down to between 350 and 460 cm^{-1}. This clearly indicates that the AlPO-5 consists of only even-numbered rings (which is in consistency with litterature presented in Section 2.1.

Asymmetric stretching vibrations of Al-O bonds is present between 600 and 800 cm^{-1}, and the two bonds at 1135 and 1240 cm^{-1} correspond to T-O stretching (more specifically P-O stretch at 1240 cm^{-1}).[71;73]

The band and shoulder marked with an asterisk (*) at approximately 889 and 940 is assigned to surface chromium species, most likely CrO_4 compounds.[74] These are

the most interesting features in the scan as they confirm that chromium is present as extraframework species.

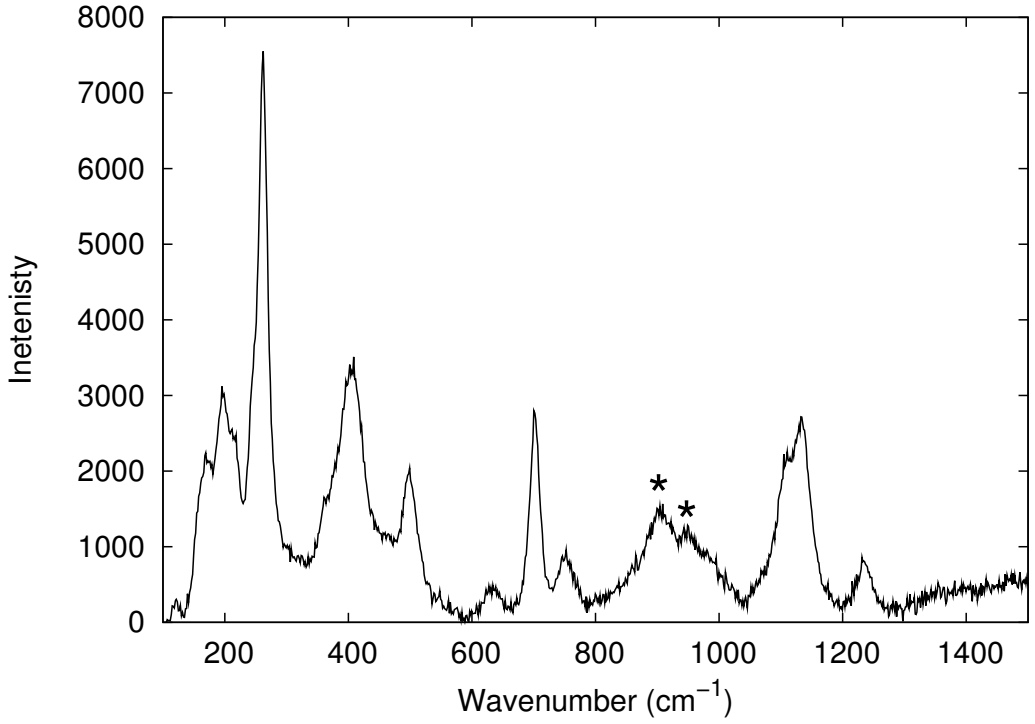

Figure 4.7: Raman spectra for CrAPO-5/1 at room temperature.

Table 4.3: Main peaks in the Raman spectrum obtained at room temperature for CrAPO-5/1.

Raman vibrations (cm^{-1})	Assignment
199	T-O-T ring breathing distortion modes
263	T-O-T ring breathing distortion modes
405	T-O-T bending
503	T-O-T bending
702	Al-O stretching
889	Cr-O stretching
1135	T-O stretching
1240	P-O stretching

The Raman spectra recorded during heating of the material in the presence of propylene/O_2 are given in Figure 4.8.

These scans have many common features with the scan recorded at room temperature, but as they were recorded over a longer range (100-4000) a peak appears at ca. 3600 cm^{-1} due to OH- vibrations which represent defects in the CrAPO-5 structure. These OH-vibrations represent terminal P-OH groups on the external surface of the CrAPO-5.[27] The surface P-OH group is expected based on the identification of extra framework Cr^{6+} which makes the material more acidic than if only incorporated Cr^{3+} was present.

The most noticable difference from room temperature is found between 850-950 cm^{-1} where the vibrations due to extra framework chromium appear. As the temperature increases (in propylene/O_2 gas flow) the features becomes smaller. This indicates that chromium is being reduced at the given conditions. This is also verified by in situ XAS measurements which is described in Section 4.8.

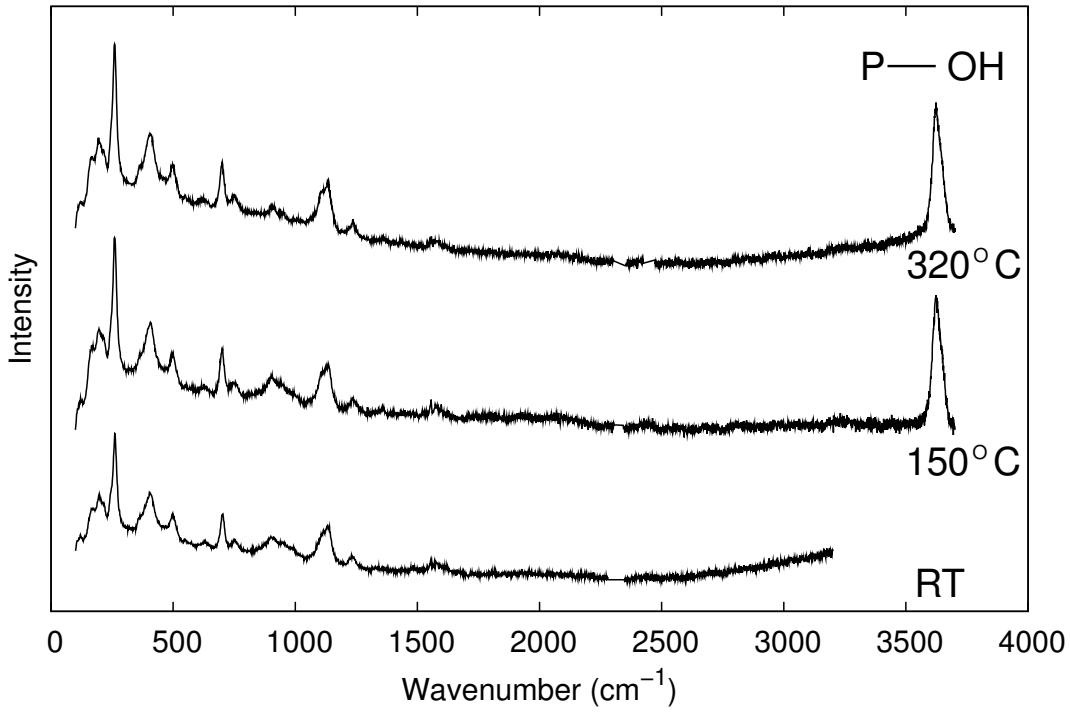

Figure 4.8: In situ Raman spectra for CrAPO-5/1.

4.6 FTIR

FTIR was performed on the as-prepared CrAPO-5/3 material with acetic acid as co-template to examine the template remomal process and identify possible acid sites at various temperatures. The results from the experiment are shown in Figure 4.9. The absorption spectra are classified into four regions, marked by I, II, III, and IV, respectively.

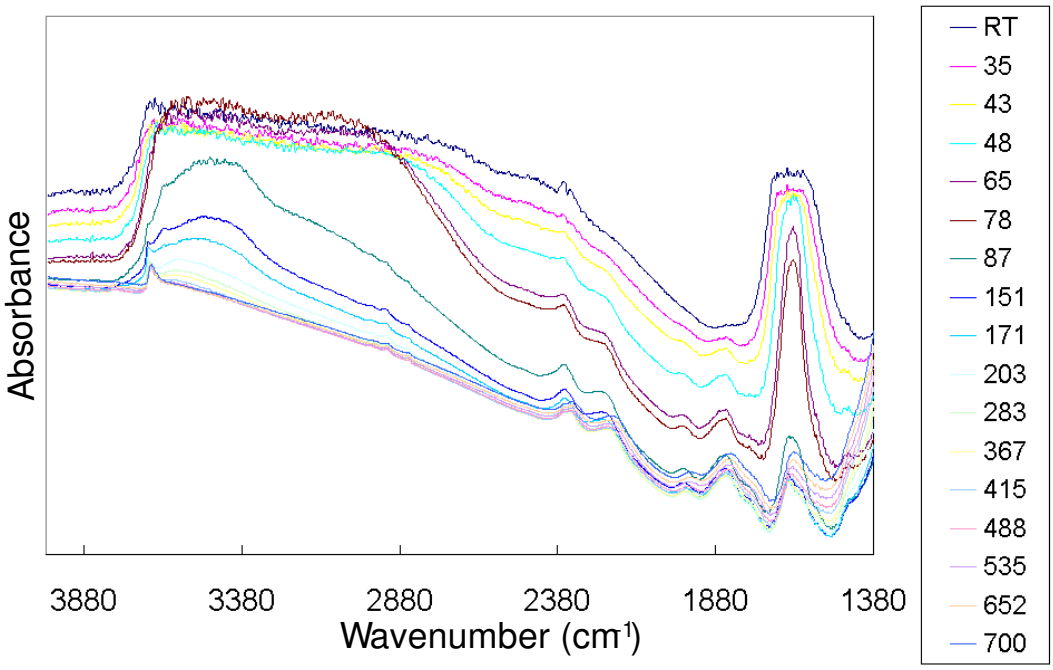

Figure 4.9: FTIR experiment on CrAPO-5/3.

The spectra at lower temperatures are dominated by bands due to absorbed water, making the identification of various species virtually impossible. As can be seen from the spectra, the material contained large amounts of water giving rise to the absorption bands between 3600 and 2800 cm^{-1} and in region IV at ca. 1630 cm^{-1}.[75]

The most surprising observation is the absence of template absorption bands. Triethylamine should give absorptions assigned to N-H and C-H stretching in region II (3400-2000 cm^{-1}).[27] Such absorptions are absent in the FTIR spectra, except for some weak absorptions that appear after dehydration between 3000 and 2800 cm^{-1}. These absorptions can possibly be assigned to C-H stretch of small amounts of residual template in the pores.

The reason for the absense of template in the CrAPO-5/3 material is still unclear, but there is a possibility that the template may have evaporated together with water when the material was dried at 80°C after the synthesis was complete. Another possible cause that was considered was template evaporation with water during the FTIR experiment. The water evaporates quite quickly due to the large pores of the material. If the template were to evaporate together with the water, this would be virtually impossible to detect as the absorptions due to the template would be overshaddowed

by the water absorptions.

In region I (4000-3400 cm^{-1} a distinct peak appears at higher temperatures (above ca. 150°C) at 3666 cm^{-1} which is assigned to stretching vibrations of P-OH present as framework defects on the external surface.[76] This indicates the presence of Cr^{6+}, which in turn means that not all the chromium in the material is incorporated in a stable manner. As Cr-O bonds cannot be detected in this experimental range, no further information can be extracted.

The features present in region III, visible above approximately 40°C is due to the overtones and their combinations of Al-O-P vibrations from the $AlPO_4$ framework. Some amorphous aluminum may be present as indicated by small absorption at ca. 3785 and 3760 cm^{-1} at higher temperatures. This indicates that the structure cannot handle temperatures above 600°C and starts to collapse.

4.7 TGA

The TGA-DSC results for CrAPO-5/1 and CrAPO-5/3 are shown in Figure 4.10 and 4.11 respectively, where the TGA curves represent percent weight loss and the DSC curves represent the enthalpy change in units of mW/g, both as a function of temperature. A positive slope in DSC curves means exothermic changes, while a negative slope means edothermic changes to the material.

Three step weight losses is observed in the 25-100, 100-400, and 400-550°C temperature ranges for CrAPO-5/1. There is a very strong desorption at temperatures below 100°C which corresponds to the release of water (m/z = 18). Another desorption can be observed in the 100-400°C range followed by another desorption at higher temperatures. The latter is probably due to combustion of the remaining TEA. The mass spectrometry results revealed that there are two water desorptions; one that occurs around 100°C and another that occurs simultaneously with the desorption of the the TEA (m/z = 86) template molecule at temperatures around 200°C. This suggests that the TEA desorption from the CrAPO-5 channels is accompanied by a simultaneous release of water. Water within the pores can possibly play a templating role, hence demanding higher temperatures in order to be released due to stronger bonding with the framework. This can be supported by the theory on cooperative structure direction presented in Subsection 2.1.3.

Two decomposition products [NH_3 (m/z = 16) and C_2H_4 (m/z = 28) were detected in different temperature regions. The release of NH_3 occurred last which is in consistency with the mechanism for template decomposition in Subsection 2.1.3.

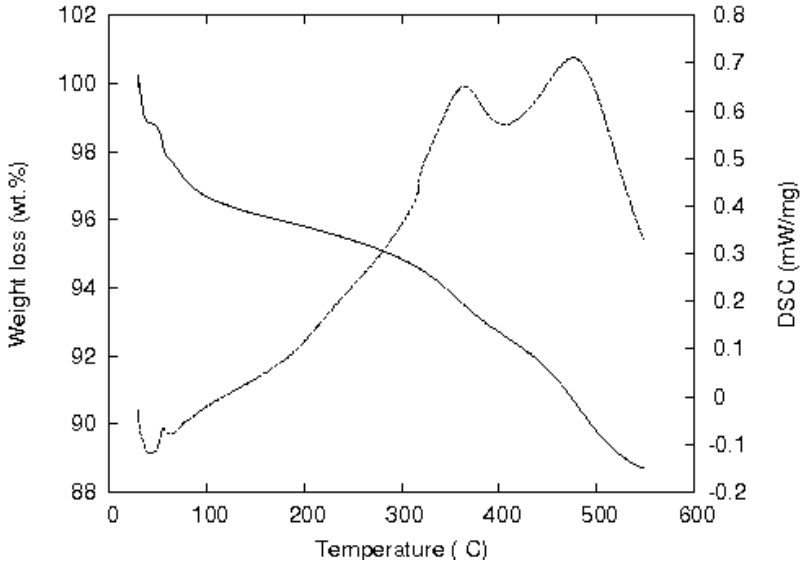

Figure 4.10: TGA-DSC curves for CrAPO-5/1

The small weight loss for CrAPO-5/3 (only about 6.5 wt.%) is unusual but yet not unexpected based on the findings from the FTIR study. None of the masses detected by the mass spectrometer corresponded to either TEA or acetic acid. There were traces of carbonaceous material detectet, however, not in significant amounts. This means that the templates have most likely evaporated together with some water during drying of the filtered product. Almost the entire weight loss observed is thus due to desorption of water. As a consequence of these findings, the CrAPO-5 using Method 3 was re-synthesized and dried at room temperature in order to get more information about the template removal process. The result of this TGA-DSC analysis is shown in Figure 4.12.

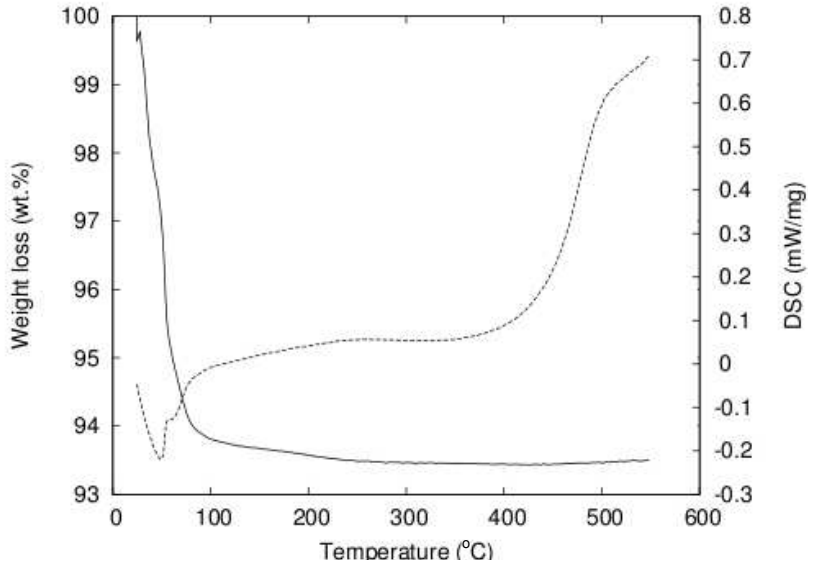

Figure 4.11: TGA-DSC curves for CrAPO-5/3

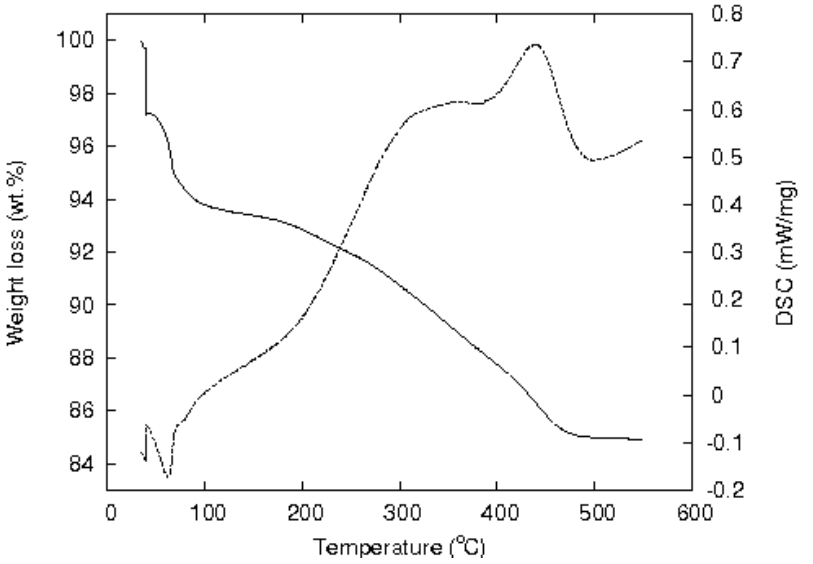

Figure 4.12: TGA-DSC curves for CrAPO-5/3b

The CrAPO-5/3 material dried in air show similar TGA-DSC curves similar to those for CrAPO-5/1. Weight loss occurs in three steps; the first assigned to the release of water, the second to template and water desorption, and the third only to template desorption. In addition to the components resulting from the decomposition of

TEA, small amounts of methane (CH_4) and carbon dioxide (CO_2) was detected at temperatures around 350°C. These decomposition products can possibly be assigned to the following reaction of acetic acid:

$$H_3CCOOH \longrightarrow CH_4 + CO_2 \tag{4.1}$$

This reaction can occur at lower temperatures[77] (starting at approximately 157°C), so it is reasonable to think that the acidic acid is bonded to the structure in such a way that it requires higher temperatures to break the bonds as apposed to acetic acid in free form.

Table 4.4: Weight loss for all materials divided into steps according to TGA-DSC graphs.

Sample	Weight loss (wt.%)			Template wt. loss	Total wt. loss
	1-Step	2-Step	3-Step	(wt.%)	(wt.%)
CrAPO-5/1	3.35	3.96	3.99	6.4	11.3
CrAPO-5/3	6.51	-	-	-	6.51
CrAPO-5/3b	6.00	2.00	7.07	9.07	15.07

4.8 XAS on CrAPO-5

4.8.1 Coordination of chromium in AlPO-5

As explained in section 2.1.4, chromium must adapt tetrahedral coordination in order to be stably incorporated into AlPO-5s. XAS is a very useful technique when investigating this local environment, and information can be extracted from both the XANES and the EXAFS region of the spectrum. Combining pre-edge analysis from XANES and the multiplicity and Fourier transform analysis from EXAFS gives a better picture on how chromium behaves when introduced in AlPO-5s.

XANES; pre-edge peak analysis

The intensity of the pre-edge peak is, as mentioned before, very sensitive to the coordination symmetry. This allows us to distinguish between octahedral and tetrahedral coordination. By investigating the pre-edges of the same compounds at various conditions and comparing them with known standards, one can be able to determine (at least semi-quantitative) the tetrahedral occupation fraction in the CrAPO-5s. In addition, the position of the pre-edge peak can, along with the position of the K-edge, tell us something about the oxidation state of chromium in the sample. Visualization of the difference in the pre-edge peaks of tetrahedral and octahedral coordinated chromium is given in Figure 4.14, where the standards $CrCl_3$ and CrO_3 represents octahedral and tetrahedral coordination respectively.

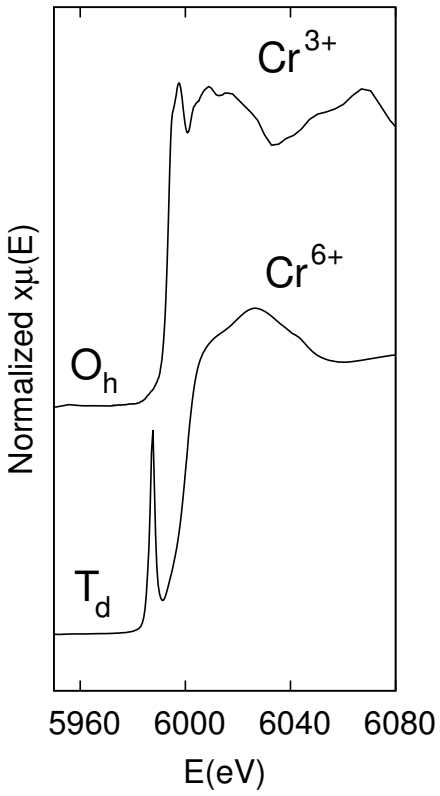

Figure 4.13: Pre-edge peak intensities of octahedral (top) and tetrahedral (bottom) coordinated chromium.

Based on the shapes of these pre-edge features it should be relatively simple to determine whether chromium in AlPO-5s tends towards tetrahedral or octahedral

coordination.

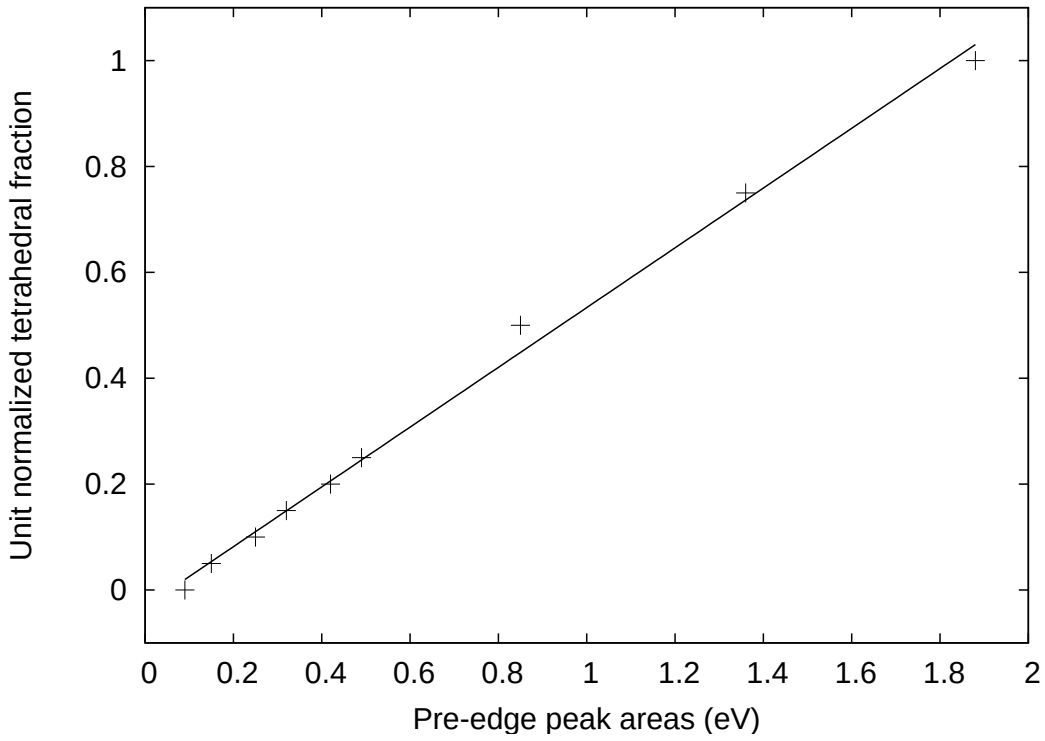

Figure 4.14: Pre-edge peak calibration curve

The area calibration curve in Figure 4.14 is based on the pre-edge peak areas obtained by XAS experiments by Huggins et al.[78] and will be used to estimate average coordination and relative Cr^{6+} content in the samples. Exact numerical values and the calibration curve parameters are given in Table 4.5. By comparing the results obtained from fitted pre-edge regions with the calibration curve, assumptions can be made with respect to the coordination number which in turn can be linked to the likelihood of chromium incorporation.

Table 4.5: Heights, widths and areas of pre-edges of known standard compounds compared with the fraction of tetrahedral coordination.

	Peak A			Peak B		
total T_d fraction	Height	Width	Area	Height	Width	Area
0	0.035	1.855	0.064	0.013	1.855	0.024
5	0.033	1.974	0.065	0.042	1.983	0.083
10	0.032	2.306	0.073	0.086	2.058	0.176
15	0.037	2.527	0.093	0.116	1.968	0.228
20	0.034	2.000	0.068	0.170	2.070	0.351
25	0.036	2.167	0.078	0.199	2.087	0.415
50	0.024	2.000	0.048	0.404	2.200	0.880
75	-	-	-	0.620	2.200	1.364
100	-	-	-	0.823	2.280	1.876

The area calibration curve in Figure 4.14 was obtained using linear regression analysis.
f(x) = m*x + c, where m = 0.57(1) and c = -0.03(1)

In order to determine more accurately in which oxidation state chromium in AlPO-5 molecular sieves exists at various conditions (e.g. changing temperature, gaseous environment etc.) a calibration curve (see Figure 4.15) was made from known chromium standards.

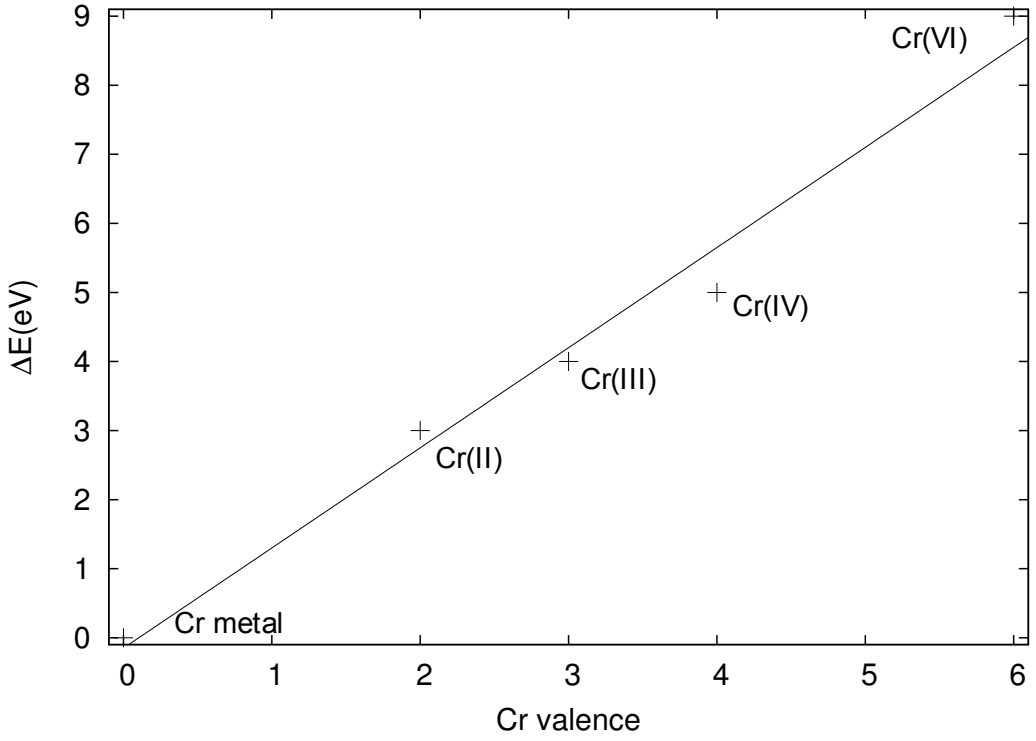

Figure 4.15: Energy positions of the Cr K-edge with respect to Cr metal plotted against various oxidation numbers.

Normalized XANES spectra of the selected samples CrAPO-5/1 and CrAPO-5/3 are shown in Figure 4.16. The derivatives of as-prepared and calcined samples are shown in Figure 4.17. Due to extremely noisy data (especially right before the pre-edge) on CrAPO-5/1, extensive deglitching was performed prior to any analyzes. As a result, some of the pre-edges look as if they have a tail towards lower energies, while it is clear from the unmodified data that they exhibit no such features. This is important to keep in mind as part of the analysis focuses on the shape of the pre-edge.

The most prominent changes occur in the pre-edge region between the as-prepared and calcined materials. Both as-prepared materials exhibit a small pre-edge feature which is a result of chromium existing mainly in its trivalent form in an octahedral field. For perfect centrosymmetric compounds, there will be no $p - d$ orbital mixing and hence no dipole transitions to add to the intensity of the pre-edge peak. The tiny features may have appeared as a result of quadrupole transitions or due to deviations (e.g. caused by vibrations) from perfect centrosymmetry. For calcined materials, the

pre-edge has grown sharp and intense, typical for Cr^{6+} in tetrahedral coordination, confirming a change in both oxidation state and geometry of the central atom.

Oxidation of chromium upon calcination is confirmed by the Cr K-edge shifts to higher energy relative to the Cr foil standard (E_0). The shift towards higher energies can more easily be seen from the first derivatives of the spectra (see Figure 4.17). The value of ΔE_{edge} ($E - E_0$) increases from as-prepared to calcined almost by a factor of 2 for CrAPO-5/1 and a factor of 1.4 for CrAPO-5/3 (see Table 4.6. These results obviously indicate that higher amounts of chromium is incorporated into the framework resisting oxidation in CrAPO-5/3.

Table 4.6: Calculated oxidation stated for chromium in various samples and conditions.

	ΔE_{edge} (eV)		Oxidation no.[a]	
Sample	As-prepared	Calcined	As prepared	Calcined
CrAPO-5/1	2.18	4.17	3.0	5.9
CrAPO-5/3	2.17	3.01	3.0	4.2

[a]Oxidation numbers are calculated using the linear regression curve in Figure 4.15 where f(x) = 1.45(2)x -0.15(5)

A closer look at the pre-edge regions of the respective materials reveals that even though the geometry changes for both materials, the pre-edge peak of CrAPO-5/3 is less intense than that of CrAPO-5/1 and has also a slightly different shape. It has a tail or shoulder towards lower energies suggesting that the symmetry around chromium is not entirely tetrahedral and also that chromium may not be fully oxidized. Further information on the valence state and coordination of chromium requires quantification of the peaks of the respective samples.

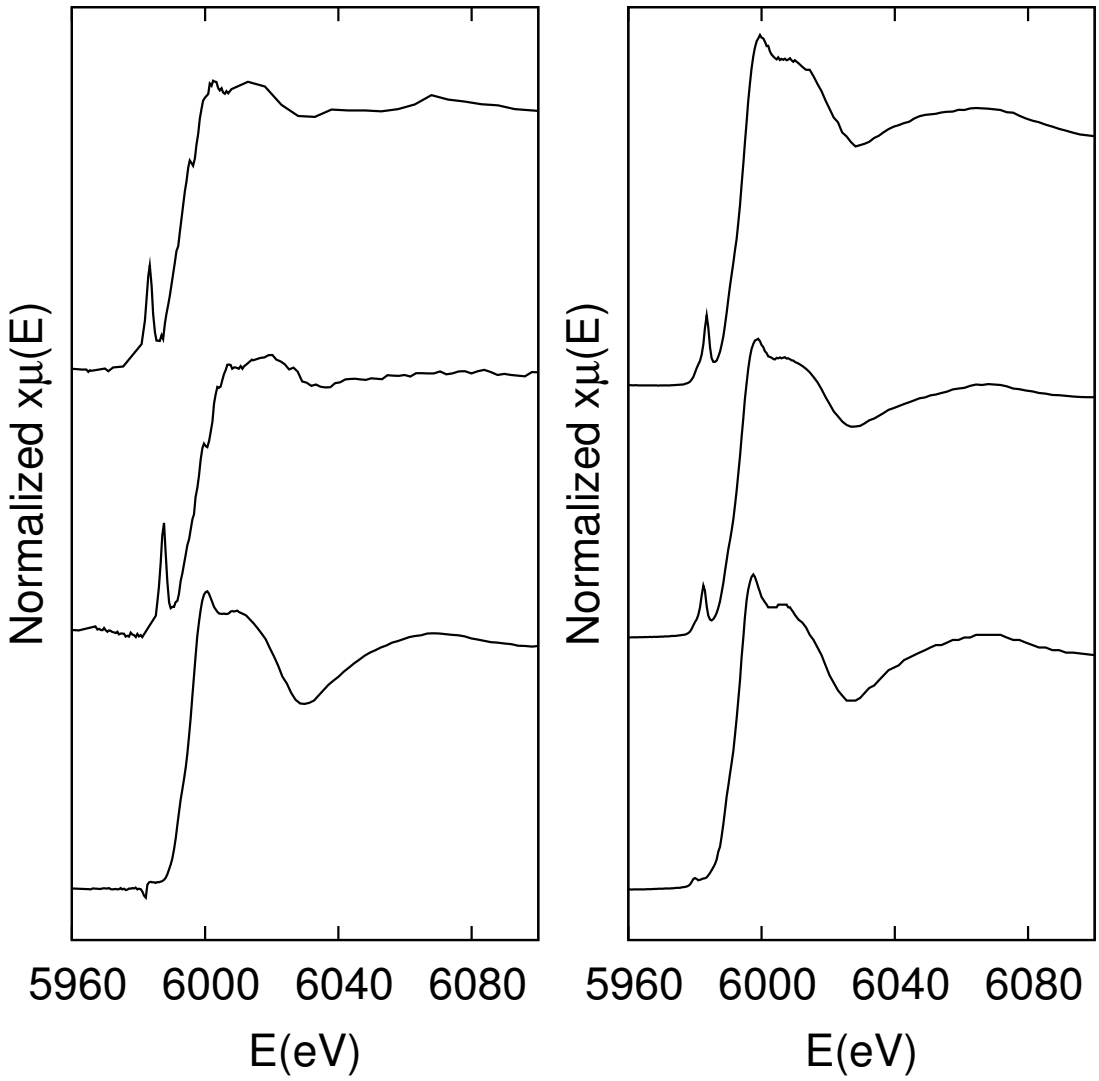

Figure 4.16: Normalized XANES on CrAPO-5/1 (left) and CrAPO-5/3 (right).

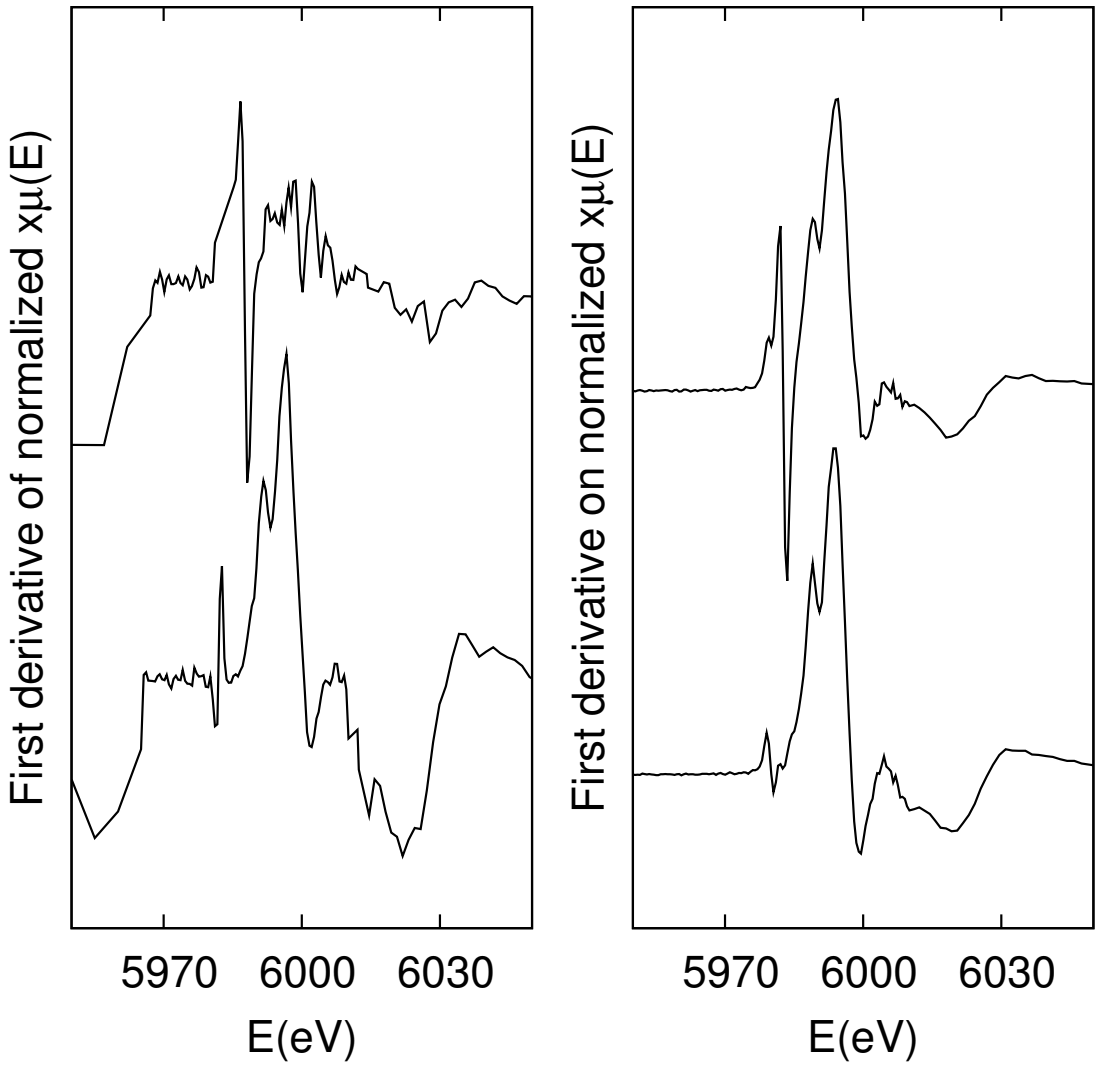

Figure 4.17: First derivative on $\mu(E)$: CrAPO-5/1 (left) and CrAPO-5/3 (right). The bottom and top graphs represent as-prepared and calcined samples respectively.

Peak fitting was performed on CrAPO-5/1 (calcined and dehydrated) and CrAPO-5/3 (as-prepared, calcined and dehydrated) as can be seen in Figures 4.18 and 4.19 respectively. Analysis of the pre-edge peak of as-prepared CrAPO-5/1 was omitted due to having an extreme glitch close to the small pre-edge.

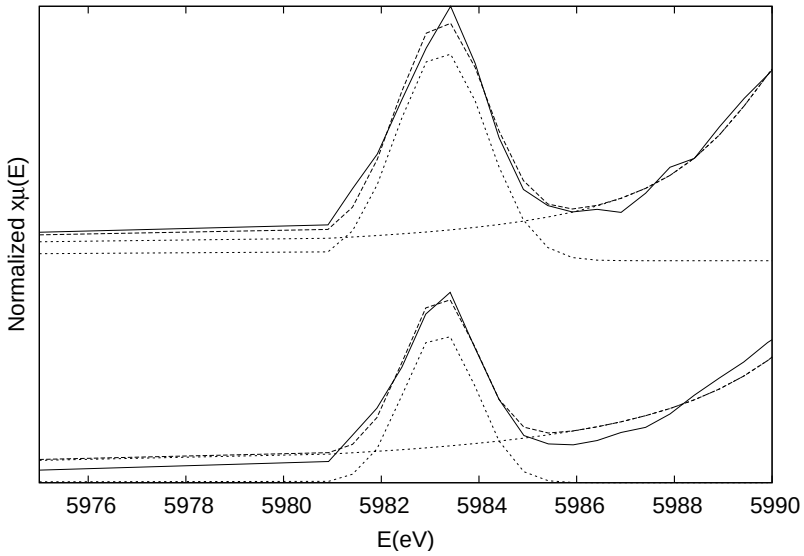

Figure 4.18: Pre-edge peak fits on calcined (bottom) and dehydrated (top) CrAPO-5/1.

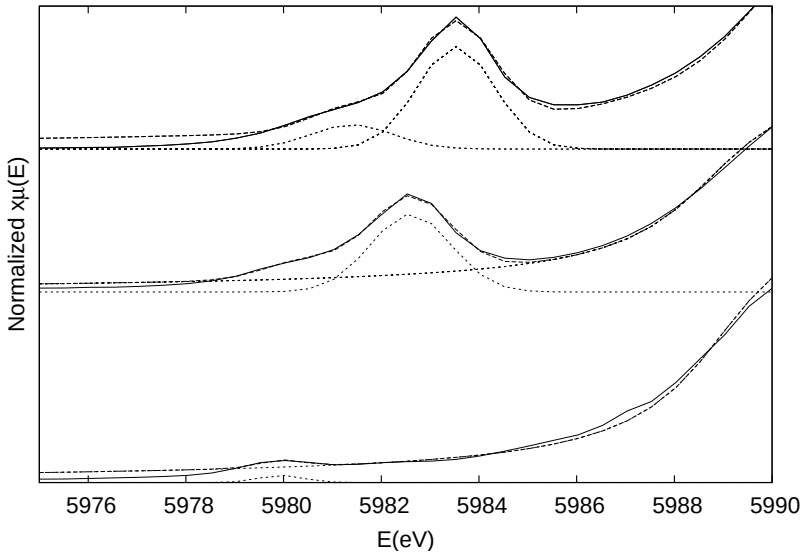

Figure 4.19: Pre-edge peak fits on as-prepared (bottom), calcined (middle) and dehydrated (top) CrAPO-5.

Upon magnification of the pre-edge areas the differences and similarities between the samples becomes even more obvious. The pre-edges are shifted to higher energies

accompanied with an increase in intensity for both samples. This supports the observations made when looking at the entrire range of XANES spectra; that Cr is oxidized and changes geometry upon calcination. A change in oxidation states means that not all (if any) of the chromium in both samples is incorporated into the framework. What is more interesting, however, is the pre-edge features of CrAPO-5/3. The presence of a pre-edge shoulder indicates that chromium is not strictly tetrahedrally coordinated. Furthermore, the integrated intensities (see Table 4.7) are smaller than those for the CrAPO-5/1 sample.

Pre-edge peak areas, heights, and widths for the as-prepared, calcined and dehydrated CrAPO-5s are given in table 4.7. All fits have correlation coefficients (R^2) above 99%. An illustration is given in Figure 4.20.

Table 4.7: Peak fit results with respect to coordination number.

		Peak A			Peak B		
Sample	T_d fraction[a]	Height[b]	Width[c]	Area	Height[b]	Width[c]	Area
CrAPO-5/3[d]	0	0.037	0.459	0.017	-	-	-
CrAPO-5/3[e]	0.19	0.033	1.939	0.064	0.168	1.786	0.300
CrAPO-5/3[f]	0.51	0.026	1.923	0.050	0.410	2.117	0.868
CrAPO-5/1[d]	0.03	0.040	1.725	0.069	-	-	-
CrAPO-5/1[e]	0.24	-	-	-	0.239	1.762	0.448
CrAPO-5/1[f]	0.70	-	-	-	0.603	2.103	1.268

[a] The sum of the peak areas were fitted on the linear regression model in Figure 4.14
[b] Peak heights are expressed as fractions of the edge step
[c] Peak widths are in eV
[d] As-prepared
[e] Calcined
[f] Dehydrated

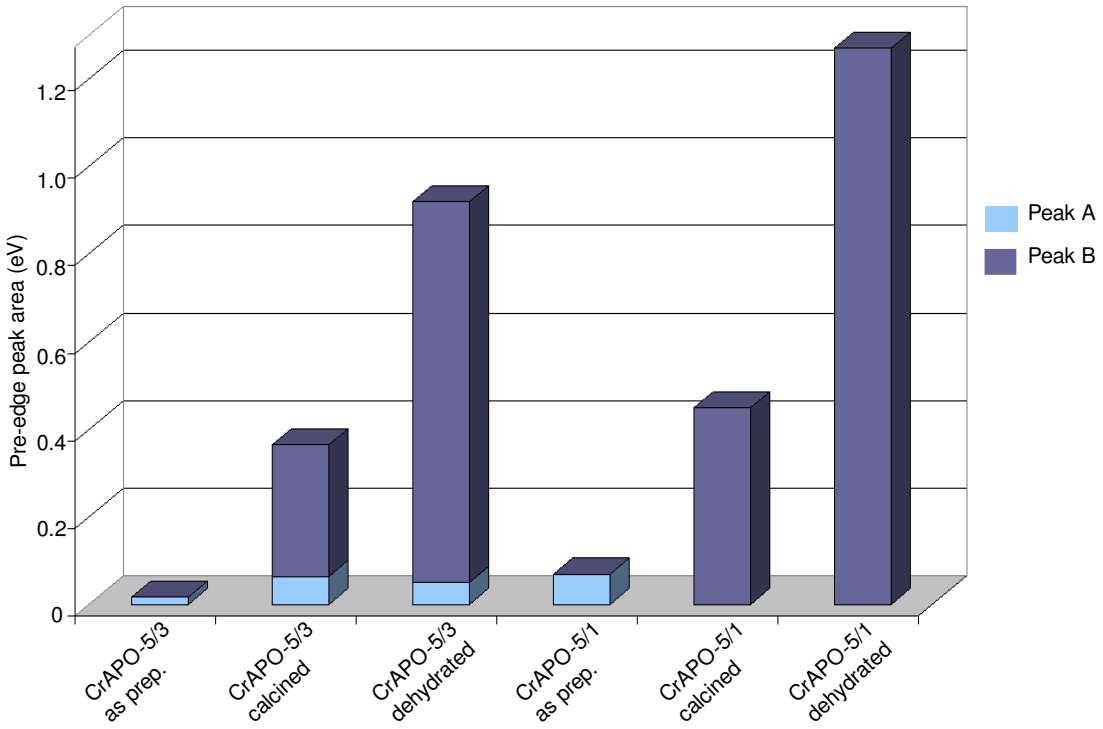

Figure 4.20: The pre-edge areas of CrAPO-5/3 and CrAPO-5/1. The contribution from the pre-edge peak shoulder is included for CrAPO-5/3.

Due to noisy data it was sometimes difficult to separate or even quantify some peaks. This was especially a problem with the as-prepared samples where the pre-edge peak is very small. For these samples, the sum of the areas of Peak A and B from Table 4.5 was used to determine the tetrahedral fraction. Note therefore that this analysis is only semiquantitative.

When comparing the pre-edge peak areas in Table 4.7 with those in Table 4.5, the difference between the samples prepared with only one template and the ones prepared with two becomes more distinct. Not only because of the presence of a second peak in CrAPO-5/3, but also because the sum of the areas of the two peaks is smaller than that of the single intense peak in the first sample. This difference indicates that higher amounts of chromium resists a change in geometry in CrAPO-5/3, which means that stably incorporated chromium is present in the sample. Further analysis of the EXAFS is necessary to find out more about the actual coordination of chromium in these samples.

Coordination from EXAFS analysis

The XAS data were first summed and background subtracted, and then the EXAFS part of the spectrum was extracted and converted to χ(k) using the EXAFS analysis software Athena[58]. The threshold energy, E_0, was determined from the first derivative spectra at the suitable inflection point. Fitting the χ^{exp}(k) to the theoretical χ^{th}(k) was carried out using the curved wave approximation using EXCURV98[59] which also calculated ab initio phase shifts for the various atoms.

Chromium(VI)oxide and Chromium(III)chloride were used as a reference compounds to confirm the ab initio phase shifts and to find the amplitude reduction factor AFAC to be transferred to the analysis of the CrAPO-5s. The results from the analysis of CrAPO/1, and CrAPO-5/3 are given in Table 4.8. Fourier Transforms and k^3 weighted EXAFS of CrAPO-5/1 and CrAPO-5/3 are shown in Figure 4.21 and 4.23 respectively.

Table 4.8: Parameters from the least squares EXAFS analysis for the model compounds used for analysis of the Cr K-edge data. Refined AFAC values were 0.8502 for CrO_3 and 0.8620 for $CrCl_3$.

Sample	Shell	N[a]	R(Å)	$2\sigma^2$(Å^2)	R(%)
CrAPO-5/1 (as-prep)	Cr-O	2.8(2)	1.71(6)	0.001[b]	41.48
	Cr-O	2.1(3)	1.92(8)	0.001[c]	
	Cr---P	0.9(4).	2.79(9)	0.001[c]	
CrAPO-5/1 (calc)	Cr-O	2.2(3)	1.61(5)	0.001[c]	32.8
	Cr-O	1.9(1)	1.89(9)	0.001[c]	
CrAPO-5/3 (as-prep)	Cr-O	4.6(2)	1.99(6)	0.009(3)	26.2
	Cr-O	0.7(4)	2.42(5)	0.004(2)	
	Cr---P	3.3(4)	3.21(7)	0.020(7)	
CrAPO-5/3 (dehyd)	Cr-O	3.2(3)	1.89(8)	0.015(3)	22.8
	Cr-O	1.1(2)	2.33(6)	0.010(2)	
	Cr---P	0.9(3)	3.15(4)	0.014(3)	

[a]The fixed multiplicities and crystallographic distances are taken from references. The standard deviation in the last significant digit as calculated by EXCURV98 is given in parentheses. These estimates, however, will in cases of high correlation between parameters lead to an overestimation of accuracy as the standard deviations for bonding distances are +/- 0.01 Åfor small r-values and +/- 0.04Åfor r-values exceeding 3Å. The deviation for $2\sigma^2$ is +/- 20%.

[b]Not refined. Fixed at 0.001.

Starting with the CrAPO-5/1, chromium starts out as six coordinated and ends up as four coordinated after being calcined. This observation is in agreement with the change in the pre-edge peak intensity seen in Figure 4.16, and that the chromium content is oxidized from mainly Cr^{3+} to mainly Cr^{5+}/Cr^{6+}. Two different Cr-O bond lengths indicate that chromium is coordinated to two water ligands and also three oxygen atoms which are part of the AlPO-5 framework.

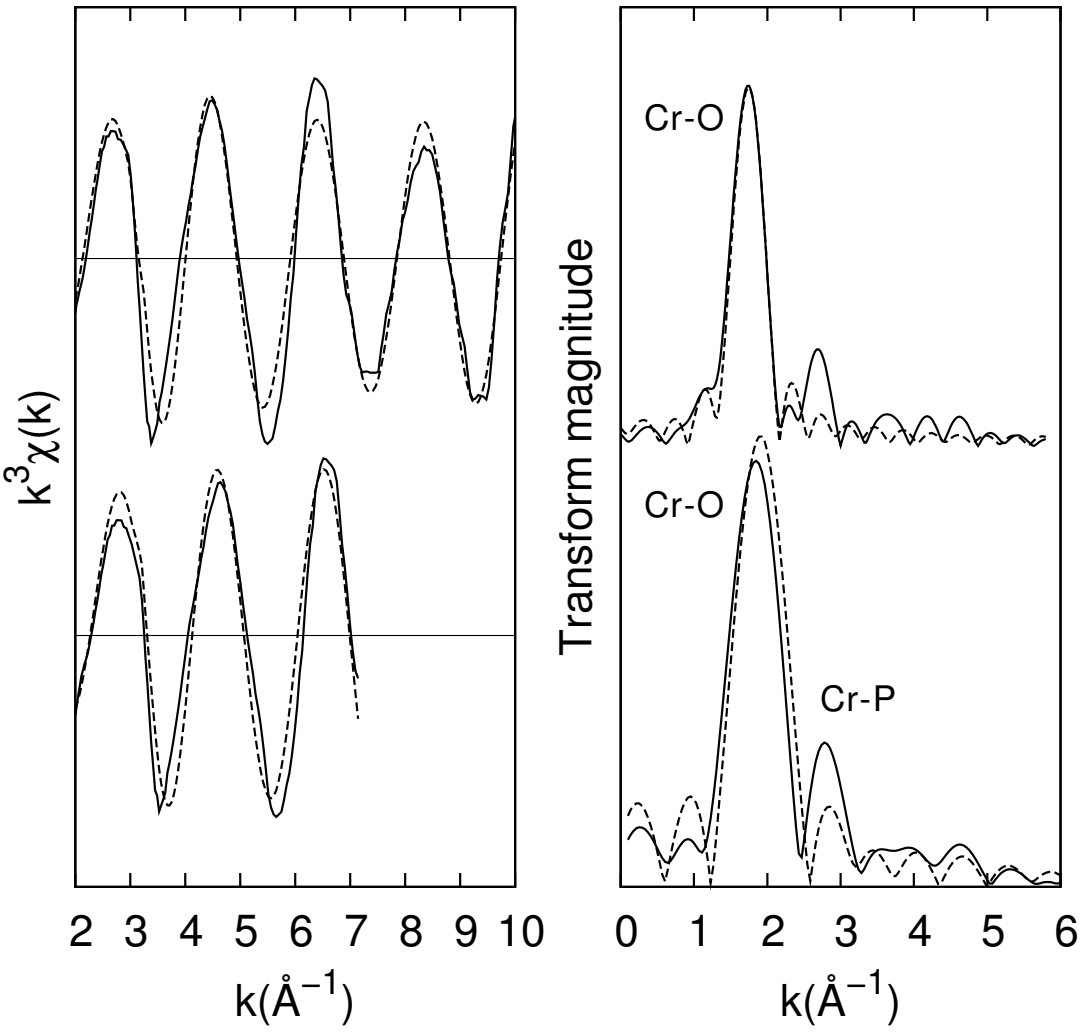

Figure 4.21: k^3 weighted EXAFS (left) and Fourier Transforms (right) of as-synthesized (bottom) and calcined (top) CrAPO-5/1.

In the calcined sample, there are also two different Cr-O bonding distances. Two of these bonds have decreased significantly compared with the bonds in the as-prepared sample, which indicate the formation of double bonds. It is therefore likely that chromium is not incorporated into the structure, but is attached to the surface as chromate species.[28] This is also supported by the fact that chromate species has an intense yellow color[79], not unlike the color the calcined sample. An illustration of what might be happening to the local geometry of Cr is shown in Figure 4.22. The suggested structure of the calcined sample is in agreement with the EXAFS analysis (see Table 4.8.

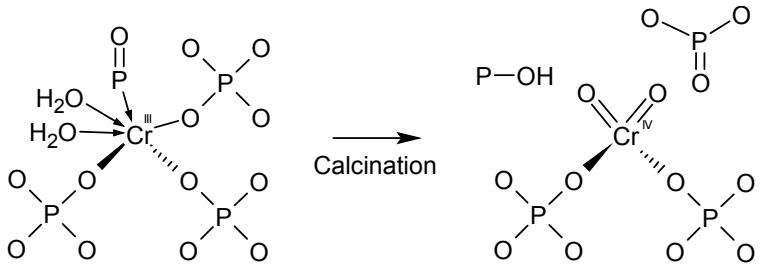

Figure 4.22: Possible local geometry of chromium in CrAPO-5/1 before (left) and after (right) calcination.

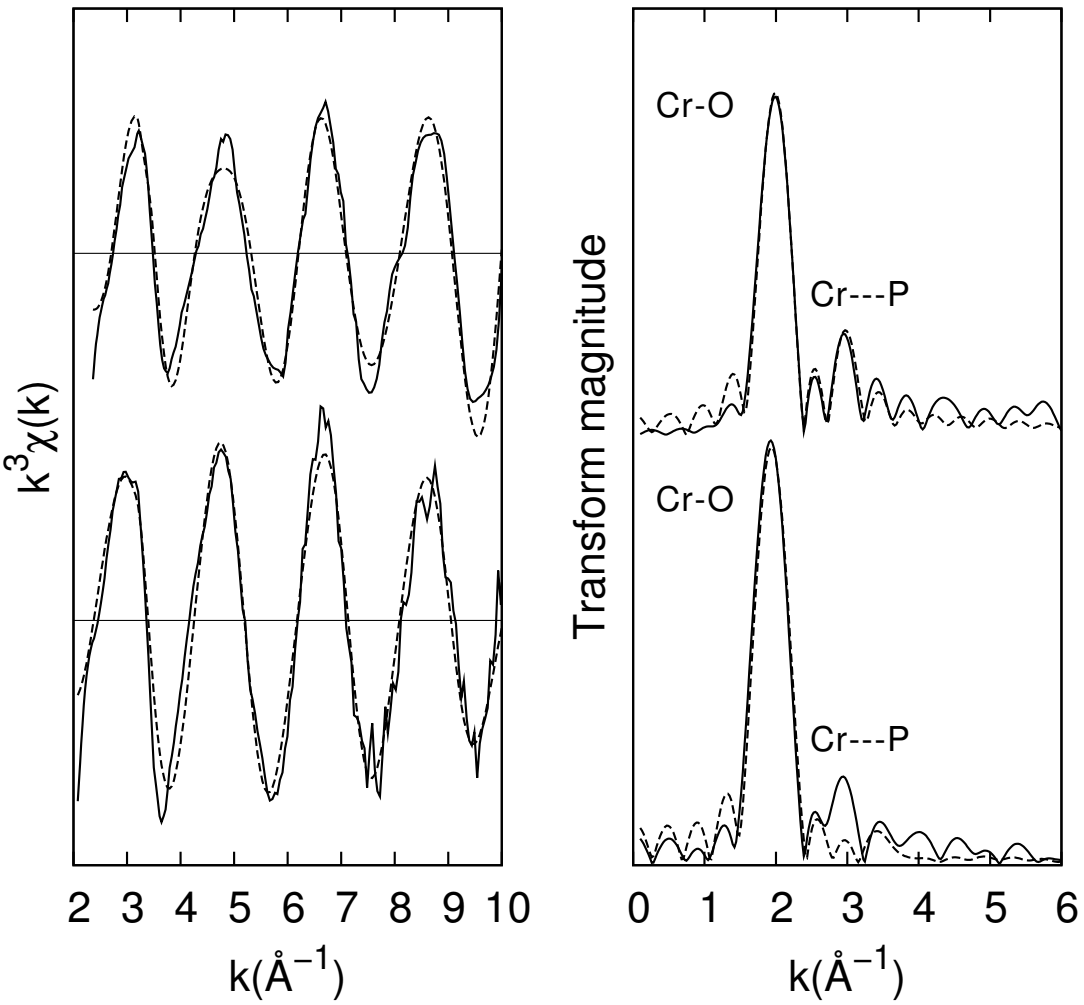

Figure 4.23: k^3 weighted EXAFS (left) and Fourier Transforms (right) of calcined (bottom) and dehydrated (top) CrAPO-5/3.

The analysis of the as-prepared and the dehydrated CrAPO-5/3 samples (Figure 4.23) reveals some rather unexpected changes that suggest that the local structure around Cr is slightly altered. As can be seen in Table 4.8, the first coordination shell of the calcined sample is occupied by five oxygen atoms at approximately 1.99 Å, and the second by one oxygen atom at 1.42 Å giving a total coordination number of six. The first main peak in the Fourier transform is composed of these two shells and upon dehydration, the peak experiences a large decrease in intensity. This effect can possibly be assigned to the decrease in the oxygen coordination number from six to four. The other effect is that the peak is shifted towards a shorter distance; i.e. the Cr-O bond is shortened. In general, a metal-oxygen bond distance for the same metal oxidation state will increase as a function of the coordination number.[80?] When trying to identify the atom in the third coordination shell, aluminum and phosphorus were the two most likely candidates. The fit was slightly better with phosphorus in the third shell, however, when including the standard deviations, the difference between phosphorus and aluminum becomes almost insignificantly small. Nevertheless, it is still more probable that chromium (provided that it adapts tetrahedral coordination) will be substituted for aluminum due to the smaller difference in ionic radii (the ionic radii of phosphorus, aluminum and chromium is given in Table 2.1 Section 2.1).

Similar results were obtained by Beale et. al.[?] who suggest that chromium has replaced a framework Al^{3+}, connected to four P atoms via four oxygen atoms, and that the contraction of the Cr-O distance is provoking a contraction of the Cr---P distances. Furthermore, they claim that the presence of one longer Cr-O bond in both calcined and dehydrated CrAPO-5 together with relatively high Debye-Waller factors implies that the octahedral and tetrahedral geometries of Cr^{3+} in the AlPO-5 are distorted. The longer bond suggests that the Cr atom slightly deviates from the normal Al position. The two oxygens removed by dehydration is believed to be connected to chromium in the form of two water molecules located in the channel of the porous material.[?] The bond lengths obtained in this work are, however, in general a bit shorter than the ones obtained by Beale et al. This indicates that there might be some bonds that have double bond character. There is most likely a mixture of incorporated and extraframework chromium present in the material, giving bonding distances somewhere in between Cr-O double bond and single bond.

4.8.2 In situ experiments on CrAPO-5

Calcined CrAPO-5/1 and CrAPO-5/3 were studied using in-situ XAS to monitor the behavior of chromium in reducing and oxidizing environments. The procedure is described in Subsection 3.8.2. Normalized and background subtracted XANES of CrAPO-5/1 and CrAPO-5/3 heated to 400°C in propene/O_2 gas flow are shown in Figure 4.24 left and right image respectively.

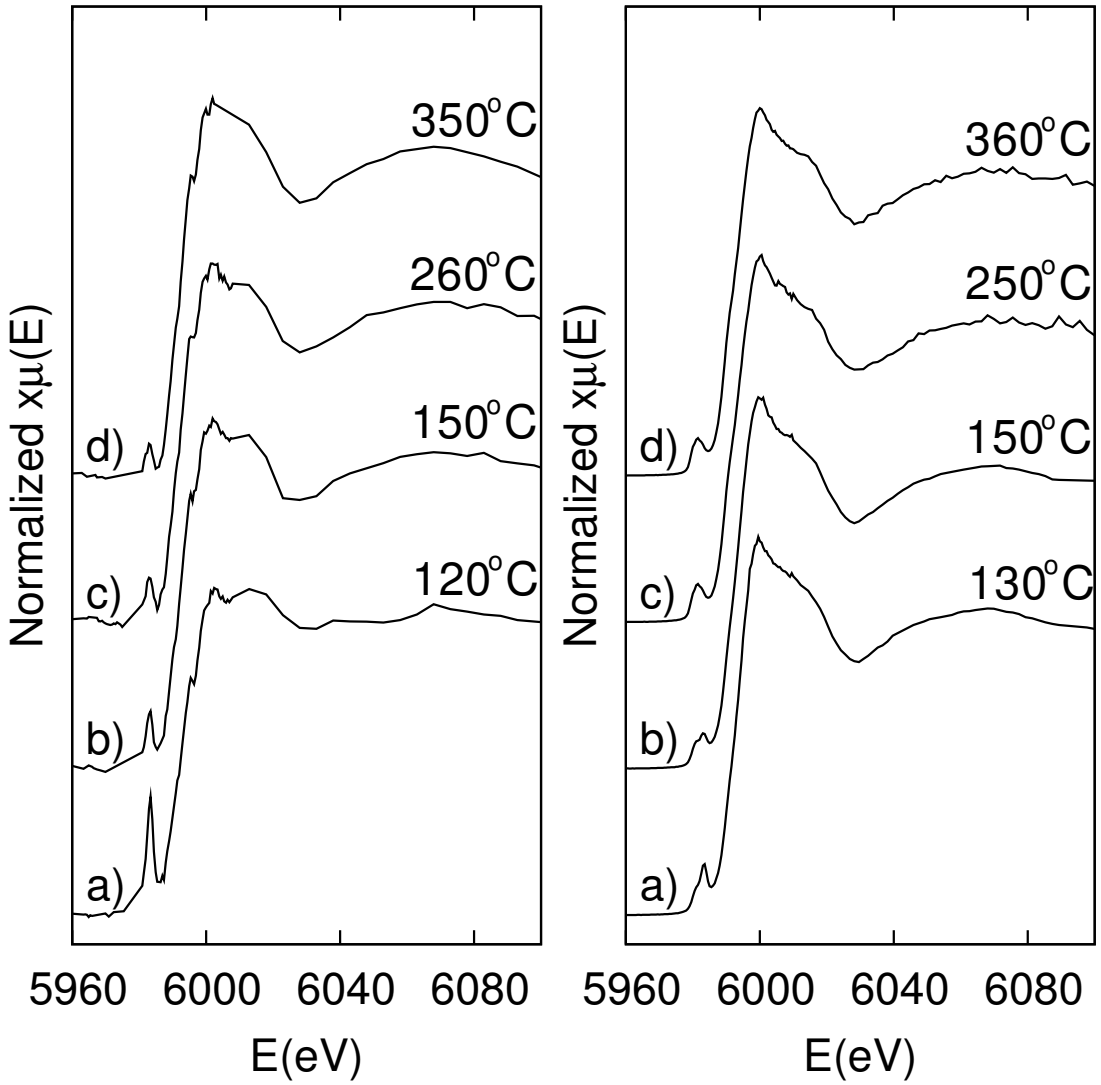

Figure 4.24: Heating CrAPO-5/1 (left) and CrAPO-5/3 (right) in propene/O_2 gas flow.

The K-edges in both samples are shifted towards lower energies (i.e. chromium is reduced) as the temperature increases in the propene/O_2 gas mixture. The reduction of chromium in CrAlPO-5 is also confirmed by Raman spectroscopy recorded simultaneously. Also, the pre-edge intensities decrease, but more so for the CrAPO-5/1 than the CrAPO-5/3. Once again, this indicates that some of the chromium is bonded in such a way that makes it harder to change the geometry. If most of the chromium present in CrAPO-5/1 is anchored to the surface, the geometry could easily be changed as it is not limited by the rigid framework. When cooled in NO/O_2 gas flow, the edges are shifted back to higher energies as can be seen in Figure 4.25. The re-oxidation is accompanied by an increase in the pre-edge peak intensities and areas. What is also worth noticing is the dependence not only of temperature, but the gases present in the in situ experiment. It has been shown that chromium is oxidized in air as the temperature increases in the calcination process. In these in situ experiments, however, chromium is reduced in propylene as the temperature increases and oxidized in NO as the temperature decreases.

The oxidation states of chromium at different temperatures and gaseous environments were calculated using the same calibration curve (from Figure 4.15) as in Table 4.6. The results are presented in Table 4.9.

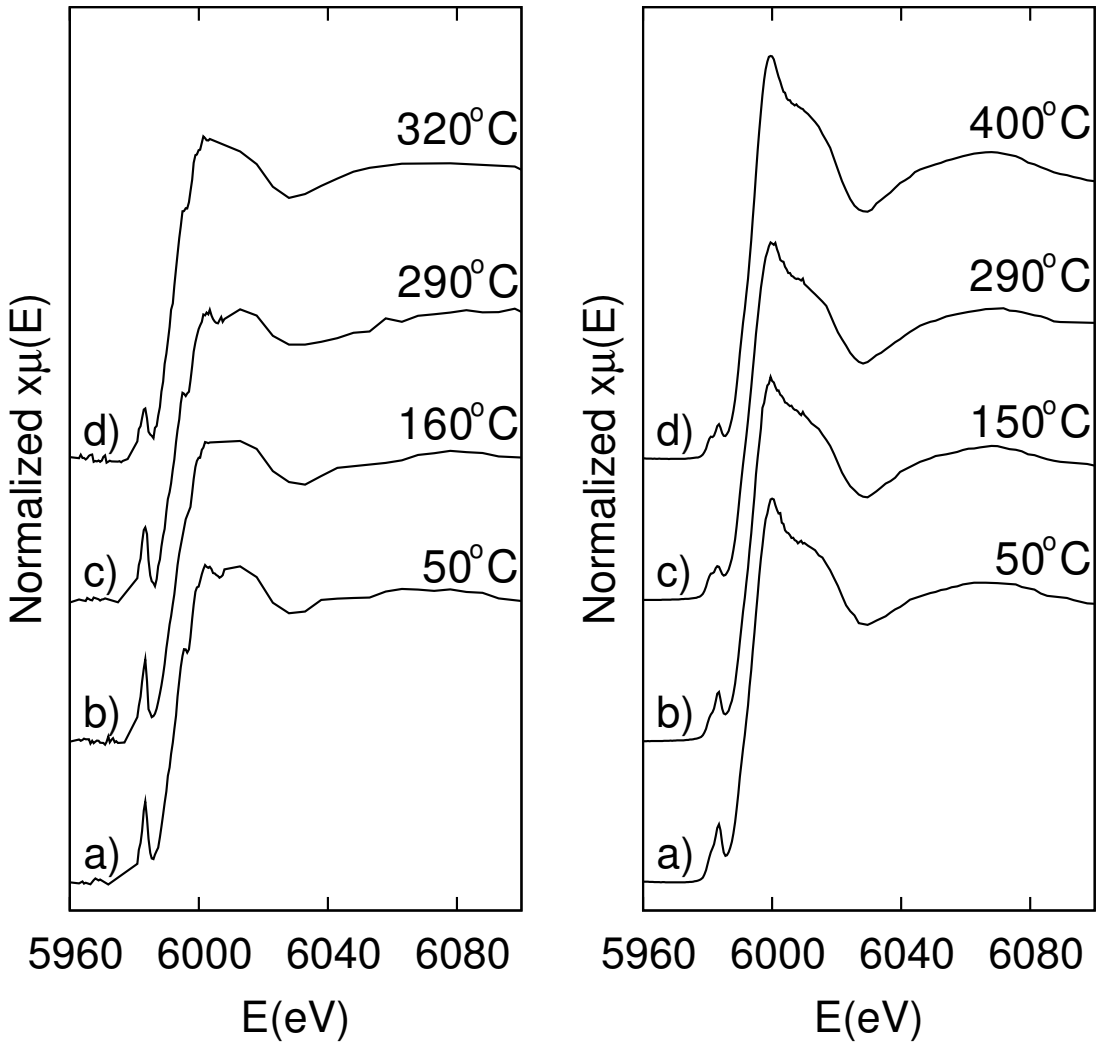

Figure 4.25: Cooling CrAPO-5/1 (left) and CrAPO-5/3 (right) in NO/O_2 gas flow.

Table 4.9: Calculated oxidation stated for chromium in various samples and conditions.

Sample	Label[a]	Heat in propene/O_2		Cool in NO/O_2	
		Edge value (eV)	Calc. oxidation no.[b]	Edge value (eV)	Calc. oxidation no.[b]
CrAPO-5/1	a	4.02	5.68	2.98	4.04
	b	3.51	4.94	2.95	4.13
	c	3.42	4.81	3.02	4.23
	d	2.91	4.07	3.98	5.62
CrAPO-5/3	a	2.93	4.10	2.74	3.82
	b	2.90	4.06	2.89	4.04
	c	2.88	4.03	3.01	4.21
	d	2.79	3.90	3.10	4.35

[a]The graph label denotes which of the graphs during the heating and cooling process (Figure 4.24 and 4.25 respectively) is being considered.

[b]Oxidation numbers are calculated using the linear regression curve in Figure 4.15 where f(x) = 1.45(2)x -0.15(5)

The trends in Table 4.9 clearly state that the oxidation state of chromium is temperature and gas-mixture dependent, and that chromium has reversible oxidation states. These results also confirm that chromium in CrAPO-5/3 is not oxidized/reduced as easily as in CrAPO-5/1. Peak fitting was performed on all pre-edge features in Figures 4.24 and 4.25. Fit results for CrAPO-5/1 and CrAPO-5/3 in situ are shown in Figure 4.27 and 4.28 respectively.

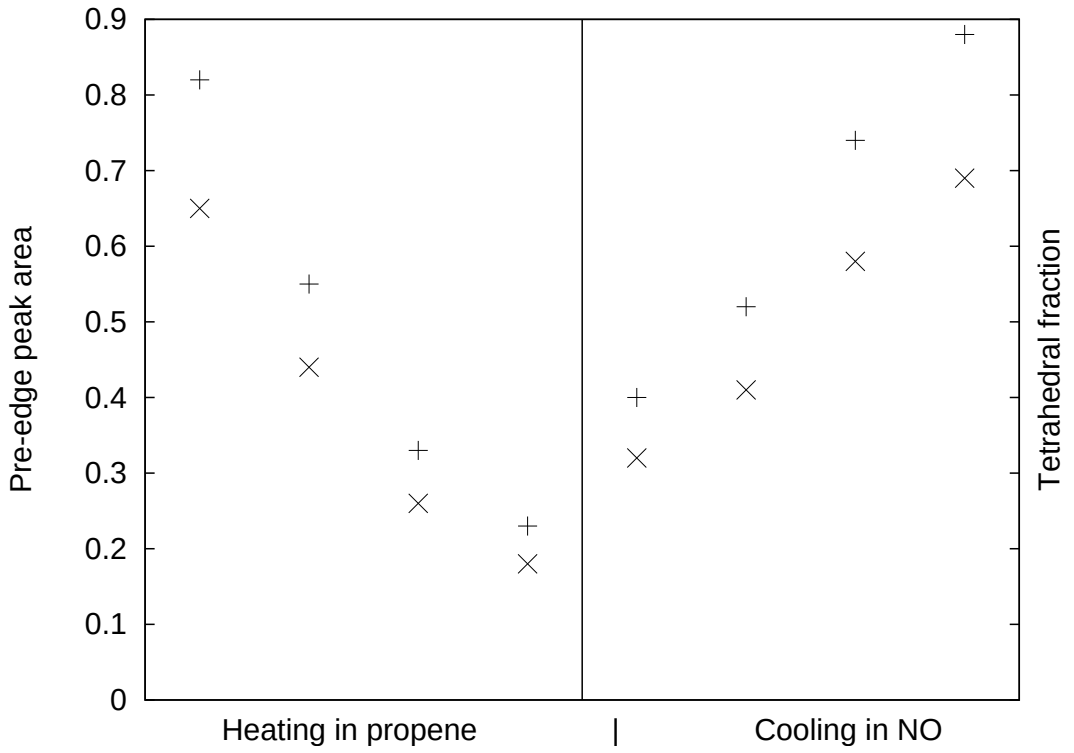

Figure 4.26: Pre-edge peak areas (x) and calculated tetrahedral fraction (+) versus CrAPO-5/1 environment.

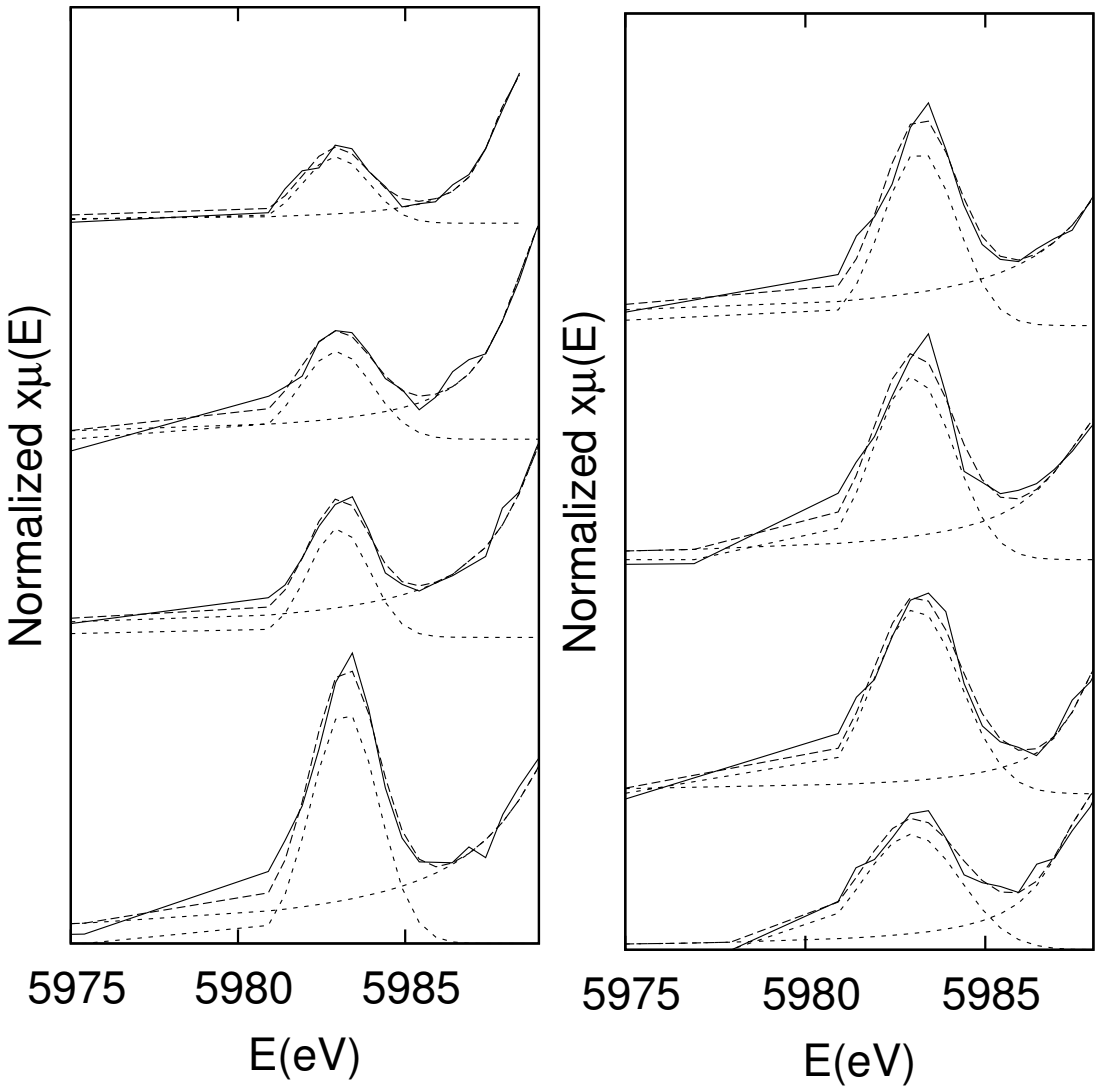

Figure 4.27: Peak fitting results for pre-edge features in CrAPO-5/1 during an in situ experiment. Heating in propene (left) and cooling in NO (right)

There is one sharp pre-edge peak in each of the CrAPO-5/1 spectra which decreases in size under treatment of propene at elevated temperatures. The centeroid of the peak is also shifted slightly towards lower energies as the chromium is reduced. It can also be seen that the peaks grow larger and are shifted towards higher energies again when the sample is cooled in NO. The pre-edge area varies almost linearly with increasing temperature in propene (linear decrease) and with decreasing temperature in NO (linear increase). The pre-edge area is clearly related to the oxidation states of

chromium in similar environments. A plot of pre-edge peak areas and Cr(VI) fraction versus in situ conditions can be seen in Figure 4.26. These results are consistent with the observations made of changes in the K-edge energy.

The pre-edge peak areas of CrAPO-5/3 show similar trends (see Figure 4.29) during the in situ study. The major difference here is that the areas are significantly smaller than those of CrAPO-5/1. The centeroids of the peaks also experience smaller shifts in energy.

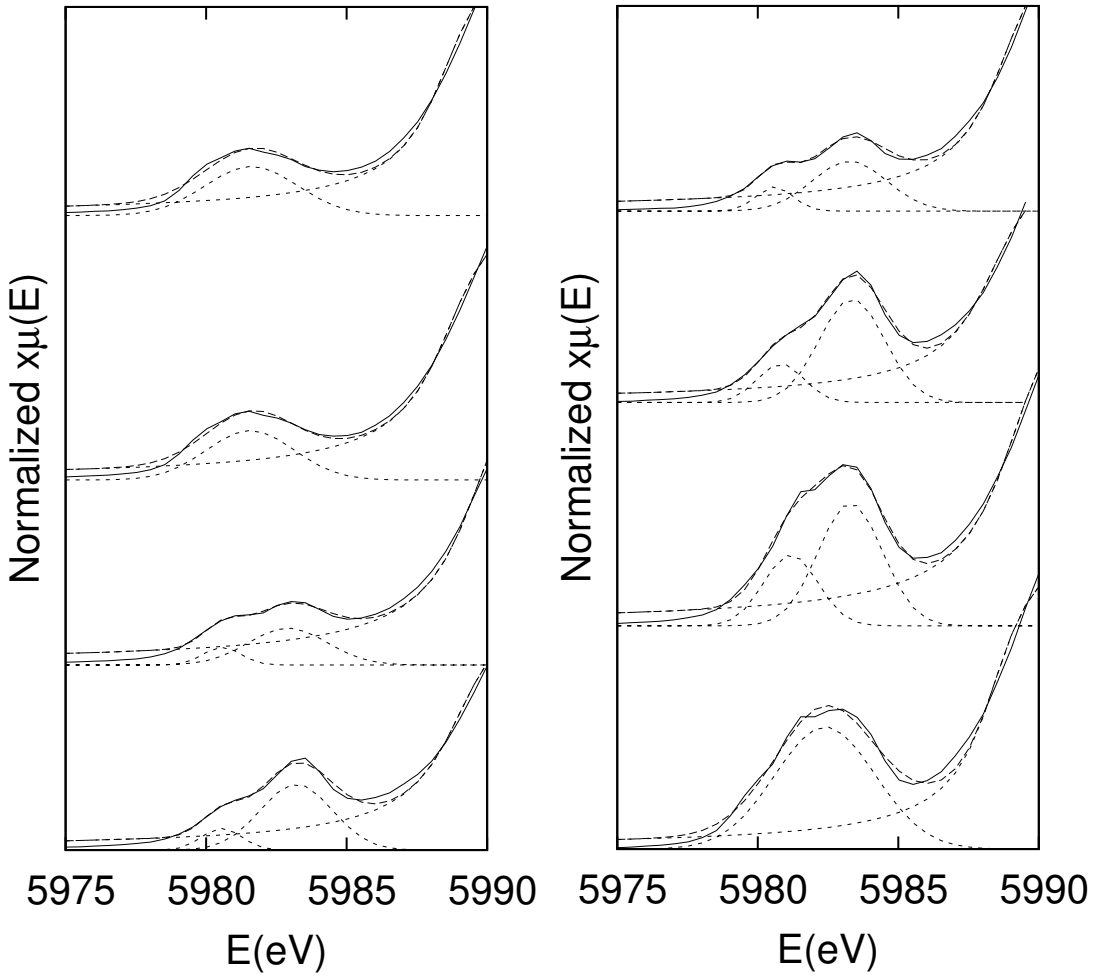

Figure 4.28: Peak fitting results for CrAPO-5/3 during heating in propene (left) and cooling in NO (right).

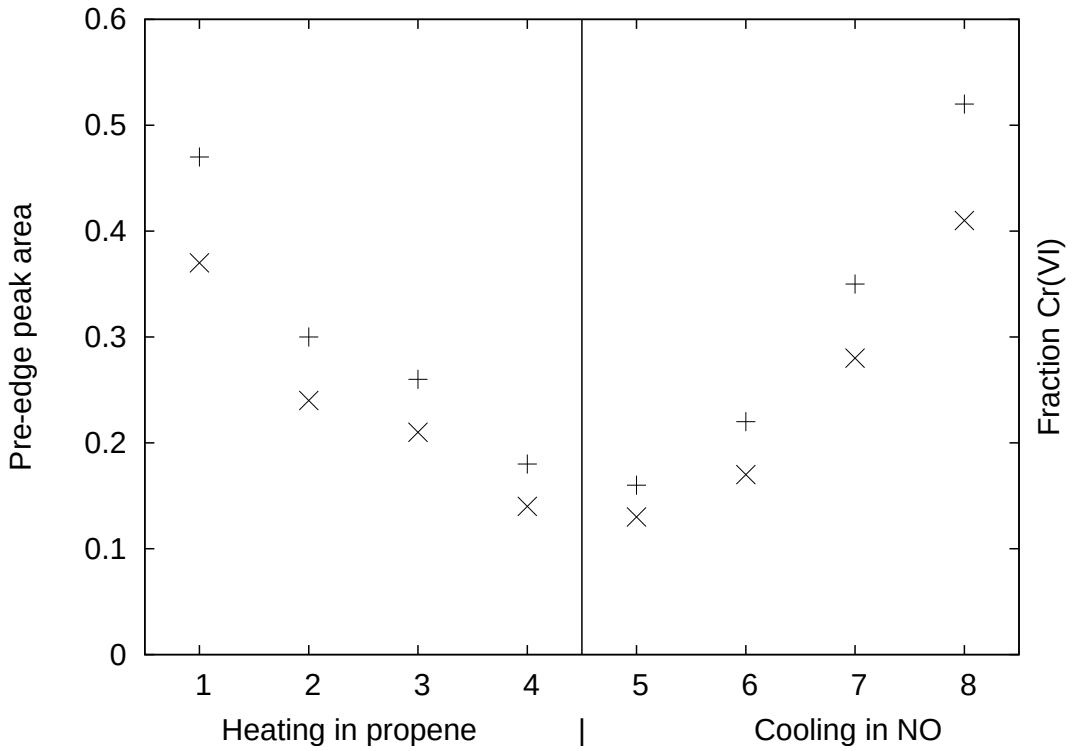

Figure 4.29: Pre-edge peak areas (x) and calculated tetrahedral fraction (+) versus CrAPO-5/3 environment.

As discussed briefly before, the most interesting features of these pre-edges are the two humps that appear only for this sample. Beale et al.[?] performed some pre-edge structure calculations for chromium with valences 2, 3, 4, and 6 in order to understand the structure and origin of such features in CrAPO-5s (ionic ground state and pure quadrupole transitions were assumed). The calculation for Cr^{3+} assumed a $1s^2 3d^3$ ground state and a $1s^1 3d^4$ final state, and Cr^{6+} was related to a $1s^2 3d^0$ ground state and a $1s^1 3d^1$ final state Figure 4.30 shows the calculations for chromium with valences 2, 3 and 4 in octahedral symmetry and 6 in tetrahedral symmetry (left), and Cr^{6+} and Cr^{3+} in tetrahedral symmetry (right).

They found that the $1s^1 3d^1$ final state for Cr^{6+} was split into E and T_2 (as predicted by the CFSE theory), where the T_2 was the only state showing quadrupole-dipole mixing. These results further indicated that the quadrupole transition has two peaks, while the dipole admixture transition has one single peak. The stick plots in the calculation for chromium with valence 3 in a tetrahedral field show the energy splitting and

intensities for the quadrupole transition. Each of those states mixes differently with the dipole transition producing the dipole spectrum.

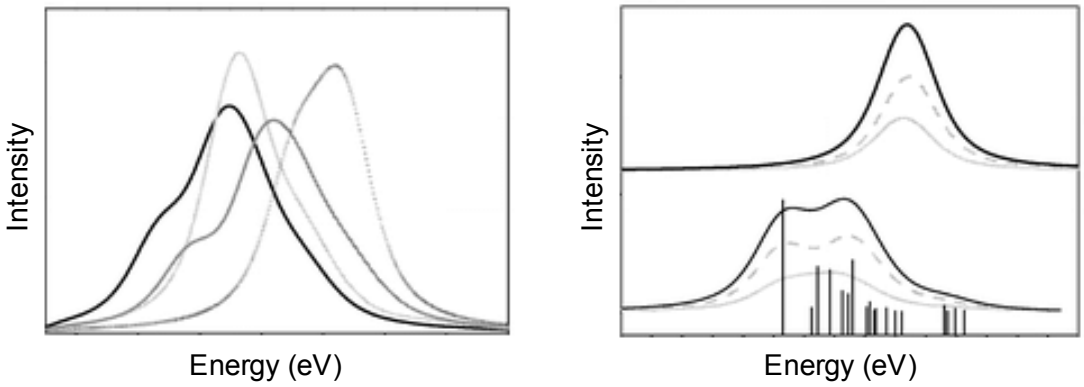

Figure 4.30: Left: The quadrupole calculation for Cr^{2+} (solid), Cr^{3+} (light gray), Cr^{4+} (dark gray), and Cr^{6+} (symbols). Right: The total pre-edge (solid) for Cr^{6+} (top) and Cr^{3+} (bottom). The pre-edge is divided into dipole (dashed) and quadrupole (solid) calculations. Stick spectrum for Cr^{3+} is added. Illustration adapted from Beale et al[3].

The graphic result for the calculation for Cr^{3+} in a tetrahedral field is more similar with the pre-edge features observed for CrAPO-5/3 in this study. It is therefore reasonable to assume that a fair amount of chromium in the sample is substituted for Al^{3+}. Structural models for hydrated and dehydrated CrAPO-5 have been proposed by Beale et al., as can be seen in Figure 4.31.

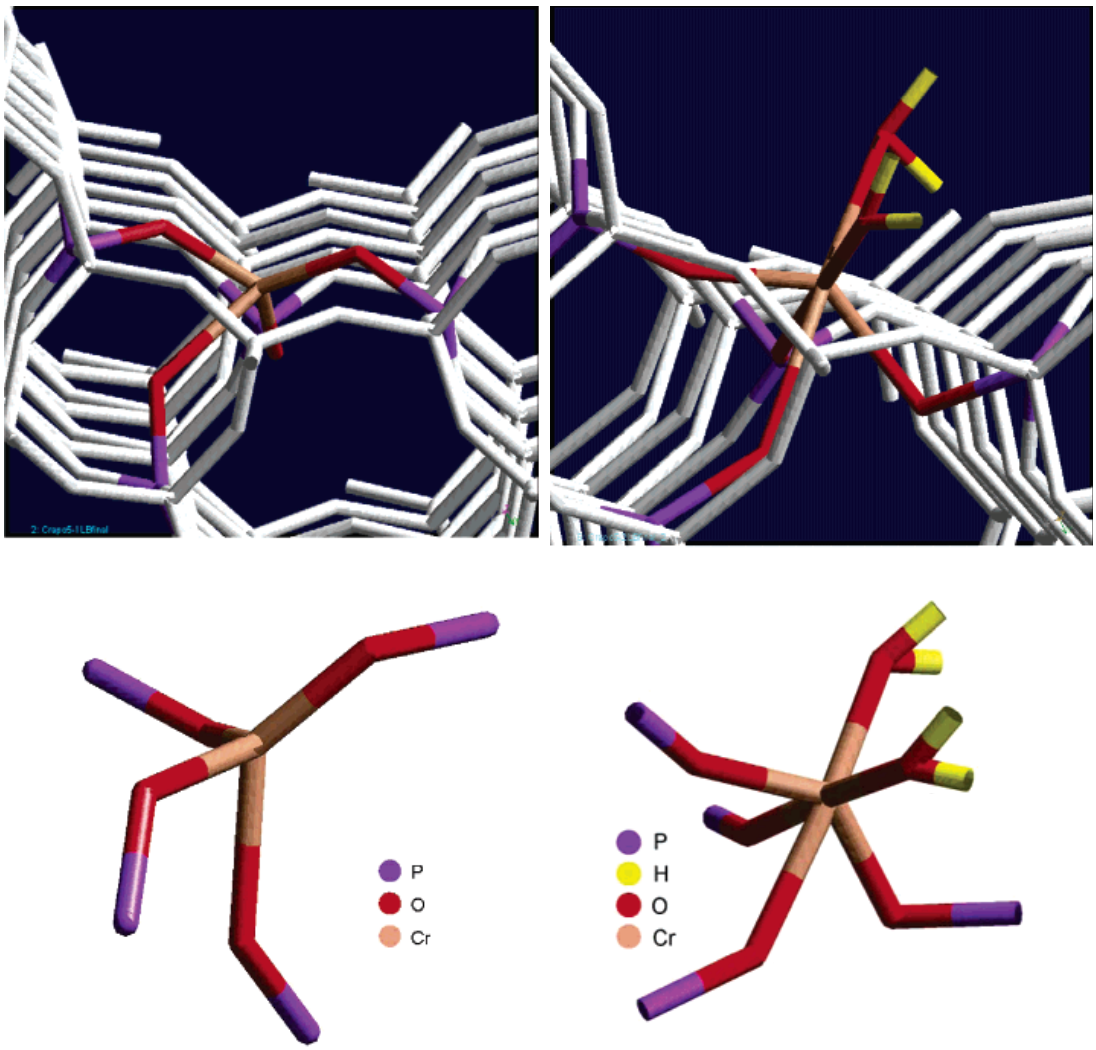

Figure 4.31: Proposed structural models for hydrated (left) and dehydrated (right) CrAPO-5 synthesized with a co-template[3].

In summary, significant differences have been obeserved between CrAPO-5s with and without a co-template. These differences become obvious when comparing the calcined samples, and also during in situ studies. For starters, the shape of the pre-edge for calcined CrAPO-5/3 is atypical for octahedral coordination. This alone is a good indicator of a distorted coordination. In addition, the chromium in this sample is not as easily oxidized as it is in CrAPO-5/1 material synthesized without a co-template. Nevertheless, the fact that it is oxidized, even if it is to a smaller extent, proves that some of the chromium is not substituted for aluminum in the AlPO-5

framework. The conclusion is thus that chromium exists in mixed states; one part being incorporated, the other not. This is also supported by FTIR spectroscopy, due to the absorption band assigned to the terminal P-OH group.

It is, however, reasonable to also conclude that the addition of a co-template (in this case acetic acid) leads to the formation of a metal-cotemplate complex that is more favorable for the framework incorporation of chromium relative to the hydrated chromium ions. Acetic acid may possibly be bonded to chromium in such a way that makes the metal deviate a little from octahedral coordination and hence eases the process of substituting chromium for aluminum.

Chapter 5

Conclusions

- In consistency with previous reports[28;33] this study has shown that Cr^{3+} cannot occupy tetrahedral sites in an AlPO-5 and is therefore not incorporated into the framework by conventional synthesis methods. Chromium is anchored at the surface of the framework as chromate species and may cause pore blockage of the material.
- In situ XAS studies on conventional CrAPO-5 material show that chromium is almost completely reduced to Cr^{3+} by propylene with incrasing temperatures. When cooled in NO, chromium is reoxidized to Cr^{6+}. As the tested material is redox active, it may be used as a catalyst in redox reactions. Due to potential pore blockage by the chromate species and hazards associated with chromium leakages, however, alternative redox catalysts should be considered. It can not be classified as a heterogenerous catalyst for liquid ohase reactions as the catalytic active species is likely to leach out and catalyze the reaction homogenically.
- The coordination geometry of chromium(III) is more flexible than what is suggested by CFSE theory. By introducing a co-template (such as acetic acid) in appropriate amounts chromium may be forced into a pseudo octahedral coordination due to favorable co-template-chromium interactions which makes substitution for Al^{3+} more probable.
- In situ XAS studies on CrAPO-5 show that a larger fraction of Cr^{3+} resists oxidation (and is therefore considered to occupy tetrahedral sites) when synthesized

with a co-template.

- Scanning electron microscopy revealed that the co-templated CrAPO-5 crystals exhibits increased symmetry, lower aspect ratios as well as more clean-cut crystals than samples prepared by conventional methods. Such properties are favorable in various optical and catalytic applications.
- The synthesis of CrAPO-5 did not favor the use of one type of chromium source over another. Regardless of the color of the synthesis gel, pale green powder was obtained after the crystallized samples were washed and dried. All materials turned yellow or greenish-yellow upon calcination except for the CrAPO-5 that was synthesized with a co-template and dried at room temperature.
- The temperature at which the co-templated material was dried had an effect on both color and elemental composition. All the other samples had various shades of yellow after being calcined. This sample showed no tendency to change color from green to yellow. The material dried at room temperature showed a (Cr+Al):P ratio closer to one than any of the other synthesized materials. This indicates that drying the sample at elevated temperatures may weaken the bonds between chromium and the surrounding oxygen tetrahedra, hence allowing chromium to adapt its preferred coordination.
- EXAFS confirms a distorted tetrahedral coordination of co-templated chromium in AlPO-5. Even though contributions from extraframework species were significant, the distortion was obvious enough. Chromium in calcined CrAPO-5 adapts a distorted octahedral coordination due to the presence of two extraframework water molecules bonded to chromium. When these are removed (by dehydration at elevated temperatures in helium), chromium remains in framework position adapting a pseudo-tetrahedral coordination.

Chapter 6

Future work

The main focus of this work has been to find a synthesis method that gives the highest amount of stably chromium incorporated into the AlPO-5 framework and examining the degree of incorporation by testing the material for redox activity. As using a co-template leads to incorporation in higher amounts, it is of interest to investigate the possibility of an "ideal" fraction of chromium substituted for aluminum and to tailor the composition of the synthesis gel so that the optimum chromium content may be incorporated. Determining sorption properties (sorption of e.g. benzene, nitrogen and water) would give a good indication towards the favorable amount of chromium in CrAPO-5s.

Considering that there is very little evidence pointing to the mechanism by which chromium is substituted for aluminum, more extensive work needs to be done on the actual role of the co-template. This can possibly be accomplished by monitoring the crystallization process by characterization techniques such as NMR, IR, and Raman spectroscopy.

Catalytic testing is ofcourse of major importance in order to determine the value of the materials as catalysts. Test reactions can be employed to test the behavior of the synthesized CrAPO-5 and to obtain information about the nature of the catalytic centers. For example, the conversion of 2-methyl-3-butyn-2-ol (MBOH) over CrAPO-5 can be used to determine the acid-base properties/character of the examined material. Conversion of isopropanol can be used to confirm the catalytic sites in CrAPO-5.[39] The importance of the stability of chromium in molecular sieves can in

this context cannot be overemphasized. Therefore, the state and stability of chromium in the crystals should be investigated. Electron paramagnetic resonance (EPR) may be used for this purpose.

Bibliography

[1] L. Gómez-Hortigüela, J. Pérez-Pariente, and F. Corà. Insight into structure direction of microporous aluminophosphates: Competition between organic molecules and water. *Chemistry - a European Journal*, 15, 2009.

[2] ESRF. ATHENA user's guide. XAS Analysis Software Using IFEFFIT, `http://www.esrf.eu/UsersAndScience/Experiments/TBS/SciSoft/Links/xafs`, July 2008.

[3] A. M. Beale, D. Grandjean, J. Kornatowski, P. Glatzel, F. M. F. de Groot, and B. M. Weckhuysen. Unusual coordination behaviour of cr3+ in microporous aluminophosphates. *J. Phys. Chem.*, 110, 2006.

[4] L. Zhou, J. Xu, C. Chen, F. Wang, and X. Li. Synthesis of Fe, Co, and Mn substituted AlPO-5 molecular sieves and their catalytic activities in the selective oxidation of cyclohexane. *Journal of porous material*, 15, 2008.

[5] W. L. Shea, R. B. Borade, and A. Clearfield. Synthesis and properties of MgAPO-5. *Journal of Chemical Society*, 89, 1993.

[6] S. K. Saha, H. Maekawa, S. B. Waghmode, S. A. R. Mulla, K. Komura, Y. Sygi, and S. J. Cho. Zincoaluminophosphate molecular sieves with AFI and ATS topologies: Synthesis by dry-gel conversion methods and their catalytic properties in the isopropylation of biphenyl. *Materials Transactions*, 46, 2005.

[7] J. D. Chen and R. A. Sheldon. Selective oxidation of hydrocarbons with O2 over chromium aluminophosphate-5 molecular sieve. *Journal of Catalysis*, 153, 1995.

[8] G. Zadrozna, E. Souvage, and J. Kornatowski. Characterization of crapo-

5 materials in test reactions of conversion of 2-methyl-3-butyn-2-ol and isopropanol. *Journal of Catalysis*, 208, 2002.

[9] J. Kornatowski, G. Zadrozna, M. Rozwadowski, B. Zibrowius, F. Marlow, and J. A. Lercher. New strategy for chromium substitution and crystal morphology control - synthesis and characteristics of CrAPO-5. *Chemistry of Materials*, 13, 2001.

[10] K. Byrappa and M. Yoshimura. *Handbook of Hydrothermal Technology - Technology for Crystal Growth and Materials Processing*. William Andrew Publishing/Noyes, 2001.

[11] E.-P. Ng and S. Mintova. Nanoporous materials with enhanced hydrophilicity and high water sorption capacity. *Microporous and Mesoporous Materials*, 12, 2008.

[12] L. E. Smart and E. A. Moore. *Solid State Chemistry - An Introduction*. Taylor & Francis Group, LLC, 2005.

[13] P. Somasundaran. *Encyclopedia of Surface and Colloid Science*. CRC Press, 2006.

[14] S. Ozaydin, G. Kocer, and A. Hepbasli. Natural zeolites in energy applications. *Energy Sources*, 28, 2006.

[15] C. N. R. Rao, A. Müller, and A. K. Cheetham. *The Chemistry of Nanomaterials - Synthesis, Properties and Applications*. WILEY-VCH Verlag GmbH & Co., 2004.

[16] S. T. Wilson, B. M. Lok, C. A. Messina, and E. M. Flanigen T. R. Cannan. Aluminophosphate molecular sieves: a new class of microporous crystalline inorganic solids. *Journal of the American Chemical Society*, 104:1146–1147, 1982.

[17] R. A. Sheldon, I. Arends, and U. Hanefeld. *Green Chemistry and Catalysis*. Wiley/VCH, 2003.

[18] S. T. Wilson. Phosphate-based molecular sieves: novel synthetic approaches to new structures and compositions. *Studies in Surface Science and Catalysis*, 37:229–260, 2001.

[19] W. Löwenstein and M. Löwenstein. The distribution of aluminum in the tetrahedra of silicates and aluminates. *Americal Mineralogist*, 39, 1954.

[20] L. Zhou, J. Xu, and C. Chen. Synthesis of Fe, Co, and Mn substituted AlPO-

5 molecular sieves and their catalytic activities in the selective oxidation of cyclohexane. *Journal of porous materials*, 15:7–12, 2008.

[21] R. Raja, J.M. Thomas, and M. Greenhill-Hooper. A high-performance selective oxidation system for the facile production of fine chemicals. *Chemical Communications*, 19:1924–1926, 2007.

[22] N. R. Shiju, S. Fiddy, and O. Sonntag. Selective oxidation of benzene to phenol over FeAlPO catalysts using nitrous oxide as oxidant. *Chemical Communications*, 47:4955–4957, 2006.

[23] P. Concepcion, T. Blasco, and J.M.L. Nieto. Preparation, characterization and reactivity of V- and/or Co-containing AlPO-18 materials (VCoAPO-18) in the oxidative dehydrogenation of ethane. *Microporous and Mesoporous Materials*, 67:215–227, 2004.

[24] Y. Peidong. *The Chemistry of Nanostructured Materials*. World Scientific, 2006.

[25] C. S. Cundya and P. A. Cox. The hydrothermal synthesis of zeolites: Precursors, intermediates and reaction mechanism. *Microporous and Mesoporous Materials*, 82, 2005.

[26] M. E. Davis and R. F. Lobo. Zeolite and molecular sieve synthesis. *Chemistry of Materials*, 4, 1992.

[27] K. H. Schnabel, G. Finger, J. Kornatowski, E. Löffler, C. Peuker, and W. Pilz. Decomposition of template in SAPO4 and AlPO-5 molecular sieves studied by IR and Raman spectroscopy. *Microporous Materials*, 11, 1997.

[28] B. M. Weckhuysen and R. A. Schoonheydt. Synthesis and chemistry of chromium in CrAPO-5 molecular sieves. *Centrum voor Oppervlaktechemie en Katalyse*, 14, 1994.

[29] P Atkins, T. Overton, L. Rourke, M. Weller, and F. Armstrong. *Inorganic Chemistry*. W. H. Freeman and Co., 2006.

[30] M. Hartmann and L Kevan. Substitution of transition metal ions into aluminophosphates and silicoaluminophosphates: characterization and relation to catalysis. *Research on Chemical Intermediates*, 28, 2002.

[31] G. Q. Lu and X. S. Zhao. *Nanoporous Materials - Science and Engineering*. Imperial College Press, 2004.

[32] E. M. Flanigen, R. L. Patton, and S . T. Wilson. Structural, synthetic and physicochemical concepts in aluminophosphate-based molecular sieves. *Innovation of Zeolite Materials Science, Studies in Surface Science and Catalysis*, 37, 1998.

[33] B. M. Weckhuysen and R. A. Schoonheydt. Chemistry and spectroscopy of chromium in zeolites. *Studies in Surface Science and Catalysis*, 84, 1994.

[34] J. G. Speight. *Lange's Handbook of Chemistry*. McGraw-Hill, 2005.

[35] M. Miyake, H. Uehara, H. Suzuki, Z. Yao, M. Matsuda, and M. Sato. Preparation and characterization of molecular sieves based on aluminum phosphate. *Polyhedron*, 8, 1988.

[36] S. C. Laha, G. Kamalakar, and R. Gläser. Microwave-assisted synthesis of [CrAPO-5]. *Microporous and Mesoporous Materials*, 90, 2006.

[37] J. Kornatowski, G. Zadrozna, J. Lercher, K. Erdmann, R. Golembiewski, and M. Rozwadowski. Co-template impact on structure of AFI type crystals: An adsorption study. *Proceedings: 14th International Zeolite Conference*, 78, 2004.

[38] J. Kornatowski and Gabriel Zadrozna. *Large and Perfect, Optically Transperent Crystals of an Unusual Habitus*. Wiley/VCH, 2007.

[39] J. Kornatowski, G. Zadrozna, J. Wlich, and M. Rozwadowski. Compositional heterogeneity of CrAPO-5 with neutral framework: Effect on sorption properties in comparison to other MeAPO-5 with charged frameworks and analytical evaluation of adsorption potentials. *Langmuir*, 15, 1999.

[40] S. Thiele, K. Hoffmann, R. Vetter, F. Marlow, and S. Radaev. Cr3+ in AlPO4-5: Single crystal u.v.-vis spectroscopy of as-synthesized and modified crystals. *Zeolites*, 19:190–196, 1997.

[41] eZ Publish. Chapter 6. Hexavalent chromium. Toxics Use Reduction Institute, University of Massachusetts Lowell `http://www.turi.org/library/turi_publications/five_chemicals_study/final_report/chapter_6_hexavalent_chromium`, April 2009.

[42] S. Gangolli. *Dictionary of Substanced and Their Effects*. Royal Society of Chemistry, 2005.

[43] C. R. Brundle, C. A. Evans, and S. Wilson. *Encyclopedia of Materials Characterization - Surfaces, Interfaces, Thin Films*. Elsevier, 1992.

[44] B.E. Warren. *X-ray Diffraction*. Courier Dover Publications, 1990.

[45] M. J. Fay, A. Proctor, D. P. Hothnann, and D. M. Hercules. Unraveling EXAFS spectroscopy. *Analytical Chemistry*, 60, 1988.

[46] B. K. Teo. *EXAFS: Basic Principles and Data Analysis*. Springer-Verlag, Berlin, 1986.

[47] B. K. Teo. Chemical applications of extended X-ray absorption fine structure (EXAFS) spectroscopy. *Accounts of Chemical Research*, 13, 1980.

[48] T. Yamamoto. Assignment of pre-edge peaks in K-edge X-ray absorption spectra of 3d transition metal compounds: electric dipole or quadrupole? *X-ray Spectrometry*, 37, 2008.

[49] B. P. Dailey. The chemical significance of quadrupole spectra. *Journal of Physical Chemistry*, 57, 1953.

[50] D. E. Sayers, E. A. Stern, and F. W. Lytle. New technique for investigating nanocrystalline structures: Fourier analysis of the extended X-ray Absorption Fine Structure. *Physical Review Letters*, 27, 1971.

[51] D.C. Koningsberger, B.L. Mojet, G.E. van Dorssen, and D.E. Ramaker. XAFS spectroscopy; fundamental principles and data analysis. *Topics in Catalysis*, 10, 2000.

[52] D. E. Ramaker, B. L. Mojet, D. C. Koningsberger, and W. E. O'Grady. Understanding atomic X-ray absorption fine structure in X-ray absorption spectra. *Journal of Physics: Condensed Matter*, 10, 1998.

[53] ESRF. ESRF - a light for sience. ESRF - A Light for Sience, `http://www.esrf.eu/`, October 2005.

[54] U. Johansson, S. Werin, and A. Nyberg. MAX-lab. MAX-lab, `http://www.maxlab.lu.se/`, April 2009.

[55] P. A. Lee, P. H. Citrin, P. Eisenberger, and B. M. Kincaid. Extended X-ray

absorption fine structure - its strengths and limitations as a structural tool. *Reviews of Modern Physics*, 53, 1981.

[56] T. Murata. Synchrotron radiation for structure analysis - EXAFS and XANES. *Microchimica Acta*, 104, 1991.

[57] B. Ravel. XAFS software catalog. ESRF A Light for Science, http://cars9.uchicago.edu/~ravel/software/doc/Athena/html/athena.pdf, Februar 2009.

[58] B. Ravel and M. Newville. ATHENA,ARTEMIS, HEPHAESTUS: data analysis for x-ray absorption spectroscopy using ifeffit. *Journal of Synchrotron Radiation*, 12:537–541, 2005.

[59] N. Binsted. EXCURV98 - the manual. Synchrotron Radiation Source, Daresbury Laboratory, http://srs.dl.ac.uk/xrs/computing/Programs/excurv97/excurv98guide.htm, July 2002.

[60] M. Newville, P. Livins, Y. Yacoby, J. J. Rehr, and E. A. Stern. Near-edge X-ray-absorption fine structure of Pb: A comparison of theory and experiment. *Physical Review Letters*, 47, 1993.

[61] Marcin Wojdyr. fityk - free peak fitting software. Institute of High Pressure Physics of the Polish Academy of Sciences, http://www.unipress.waw.pl/fityk, January 2008.

[62] P. J. Ellis and H. C. Freeman. XFIT - an interactive EXAFS analysis program. *Journal of Synchrotron Radiation*, 2, 1995.

[63] Kaiser Optical Systems Inc. Raman technical resources, June 2006.

[64] A. J. Holmes, S. J. Kirkby, G. A. Ozin, and D. Young. Raman spectra of the unidimensional aluminophosphate molecular sieves AlPO4-11, AlPO4-5, AlPO4-8, and VPI-5. *Journal of Physical Chemistry*, 98, 1994.

[65] B. Stuart. *Infrared Spectroscopy : Fundamentals and Applications*. John Wiley and Sons, Incorporated, 2004.

[66] P. J. Haines. *Thermal Method of Analysis - Principles, Applications and Problems*. Chapman and Hall, 1995.

[67] Evans Analytical Group. Inductively coupled plasma spectroscopy (ICP-

OES/MS). The Global Leader in Surface Analysis and Materials Characterization - Evans Analytical Group (EAG), http://www.eaglabs.com/, April 2009.

[68] Inc. Elemental Scientific. Sample introduction technology for ICPMS and ICpAES. ESI - Elemental Scientific), http://www.icpms.com/, April 2009.

[69] D. A. Skoog, D. M. West, F. J. Holler, and S. R. Crouch. *Fundamentals of Analytical Chemistry*. Brooks/Cole, 2004.

[70] J. W. Croft. *Under the Microscope : A Brief History of Microscopy*. World Scientific, 2006.

[71] P. P. Knops-Gerrits, D. E. De Vos, E. J. P. Feijen, and P. A. Jacobs. Raman spectroscopy on zeolites. *Microporous Material*, 8, 1997.

[72] A. J. Holmes, S. J. Kirkby, G. A. Ozin, and D. Young. Raman spectra of the unidimensional aluminophosphate molecular sieves AlPO4-11, AlPO4-5, AlPO4-8, and VPI-5. *Journal of Physical Chemistry*, 98, 1994.

[73] K. J. Chao, C. N. Wu, H. Chang, L. J. Lee, and Shu fen Hu. Incorporation of vanadium in mesoporous MCM-41 and microporous AFI zeolites. *Journal of Physical Chemistry*, 101, 1997.

[74] M. A. Vuurman and I. E. Wachs. In situ raman spectroscopy of alumina-supported metal oxide catalysts. *Journal of Physical Chemistry*, 96, 1992.

[75] S. C. Popescu, S. Thomson, and R. F. Howe. Microspectroscopic studies of template interactions in AlPO4-5 and SAPO-5 crystals. *Physical Chemistry Chemical Physics*, 3, 2000.

[76] Z. M. Li, J. P. Zhai, H. J. Liu, I. L. Li, C. T. Chan, P. Sheng, and Z. K. Tangb). Synthesis of 4 åsingle-walled carbon nanotubes in catalytic Si-substituted AlPO4-5 molecular sieves. *Applied Physics Letters*, 85, 2004.

[77] J. C. Mackie and K. R. Dodlan. High-temperature kinetics of thermal decomposition of acetic acid and its products. *International Journal of Chemical Kinetics*, 16, 1983.

[78] F. E. Huggins, M. Najih, and G. P. Huffman. Direct specitation of chromium in coal combustion by-products by X-ray Absorption Fine-structure Spectroscopy. *Fuel*, 1999.

[79] Quality Assurance Department. Msds - material safety data sheet, chromate. Mallinckrodt Baker Inc., http://www.jtbaker.com/europe/msds/pdf07/GB/MSDS_0210_GB.pdf, September 2007.

[80] F. M. F. deGroot. X-ray absorption and dichroism of transition metals and their compounds. *Journal of Electron Spectroscopy and Related Phenomena*, 67, 1994.